



SOLID-STATE STUDIES OF INCLUSION
COMPOUNDS AND OTHER ORGANIC MATERIALS

A thesis submitted for the degree of Doctor of Philosophy by

ANABEL MORTE RÓDENAS

Supervisor: K. D. M. Harris

School of Chemistry

Cardiff University

February 2011

UMI Number: U585419

All rights reserved

INFORMATION TO ALL USERS

The quality of this reproduction is dependent upon the quality of the copy submitted.

In the unlikely event that the author did not send a complete manuscript and there are missing pages, these will be noted. Also, if material had to be removed, a note will indicate the deletion.



UMI U585419

Published by ProQuest LLC 2013. Copyright in the Dissertation held by the Author.
Microform Edition © ProQuest LLC.


All rights reserved. This work is protected against
unauthorized copying under Title 17, United States Code.



ProQuest LLC
789 East Eisenhower Parkway
P.O. Box 1346
Ann Arbor, MI 48106-1346


DECLARATION

This work has not previously been accepted in substance for any degree and is not concurrently submitted in candidature for any degree.

Signed  (candidate) Date 04/02/11


STATEMENT 1

This thesis is being submitted in partial fulfillment of the requirements for the degree of PhD

Signed  (candidate) Date 04/02/11


STATEMENT 2

This thesis is the result of my own independent work/investigation, except where otherwise stated. Other sources are acknowledged by explicit references.

Signed  (candidate) Date 04/02/11

STATEMENT 3

I hereby give consent for my thesis, if accepted, to be available for photocopying and for inter-library loan, and for the title and summary to be made available to outside organisations.

Signed  (candidate) Date 04/02/11

A mis padres...

Acknowledgements

First of all I would like to thank my supervisor Prof. Kenneth D. M. Harris for all his support, assistance and guidance, and for welcoming me into the group. It has been a really fulfilling experience.

I would also like to thank everybody in our research group (past and present) with special mention to Dr Colan Hughes for all his unconditional help and patience and Dr Eugene Cheung for his encouragement in the first steps of this journey.

I am especially grateful to Dr Benson Kariuki for motivating me and for extremely helpful scientific discussions and Prof. Steven Collins for passionate insights on physics and for invaluable experimental assistance at Diamond Light Source.

I would like to thank all the technical staff and stores in the School of Chemistry for making everyday research life easier. Thank you Mr Alun Davies for all the support and teaching (and for the good press)! A special thanks to the

administrative staff in the School of Chemistry, in particular Terrie and Alison for their serious work and the enjoyable moments!

M'agradaria donar les gràcies d'una manera molt i molt especial a l'Eugènia Estop i al José Luís Briansó per fer-me estimar la cristal·lografia i per donar-me aquesta gran oportunitat i creure en mi, sense vosaltres, tot això no hagués estat possible.

Y a vosotros, los que me entendéis: ¡¡Muchas gracias por todo!! Todo ha sido mucho más fácil con vosotros cerca. Muchas gracias Carlos, Paulilla, Isabel, Vero, Niek, Yaiza, Pili, Toni, Kathrin, Giorgia, Vanesa, Manuel, Caterina, Deborah, Eli, Txell, Xavi, Carmen, Rob, Juan, Ginger, Raimon, Lydia, Inés, Paola, Alicia (espero no haberme olvidado a nadie). And for the non-Spanish speakers, Lino, Grazia, Maurizio, Yuehua, Non, Adrian, Massimo, Dirk, Soraya, Vincenzo, Gabrielle, Judith, Ioanna, Jon, Geraint, Matt, Dan, Theo, Alex, thank you for making my life in Cardiff really enjoyable and pleasant. I have learned a lot from every person that I have met on the way!

Y por supuesto y sobre todo dar las gracias a mis padres preferidos y al nenito, a mis abuelas y a mis tíos y primos. ¡¡Gracias por aguantarme!! ¡¡Os quiero mucho a todos!!

Abstract

This thesis comprises the results of research on various aspects of solid inclusion compounds and other organic materials.

Chapter 1 is an introduction to solid-state inclusion compounds, in particular describing the main characteristics of urea inclusion compounds and thiourea inclusion compounds.

The experimental techniques utilized during the research are described in Chapter 2. These techniques include X-ray diffraction techniques (single crystal X-ray diffraction, powder X-ray diffraction and the characteristics of synchrotron radiation) and thermal analysis techniques (differential scanning calorimetry and thermogravimetric analysis).

In Chapter 3, the main focus concerns studies of the solid-state properties of a special type of non-conventional urea inclusion compound formed with α,ω -diaminoalkane guest molecules, and also incorporating methanol molecules

within the structure. The present work is focused primarily on the stability of these materials, and the evolution of structural phases formed upon decomposition as function of time.

Novel X-ray birefringence and X-ray dichroism investigations carried out at the Diamond Light Source (UK) on different thiourea inclusion compounds (1-bromoadamantane/thiourea inclusion compound, 2-bromoadamantane/thiourea inclusion compound and bromocyclohexane/thiourea inclusion compound, which has an order-disorder phase transition at low temperature) are reported in Chapter 4, where pioneering X-ray dichroism and X-ray birefringence measurements in organic compounds have proved to serve as a sensitive probe of changes in molecular orientation at order-disorder phase transitions.

Chapter 5 is aimed at broadening the understanding of polymorphism and chemical reactivity of oxalyl dihydrazide at high temperatures using time-resolved powder X-ray diffraction data recorded at the Daresbury SRS (UK).

Chapter 6 reports a powder X-ray diffraction study of the solid-state dehydration process of *t*-butylammonium acetate monohydrate, and the structural consequences of the dehydration process.

Table of Contents

Chapter 1 – Introduction

| | |
|--|---|
| 1.1 – Solid Inclusion Compounds | 1 |
| 1.1.1 – Urea Inclusion Compounds | 2 |
| 1.1.2 – Thiourea Inclusion Compounds | 5 |
| 1.1.3 – Applications | 7 |
| 1.2 – Solid-State Structural Transformations | 8 |
| 1.3 – References | 9 |

Chapter 2 – Experimental Techniques

| | |
|---|----|
| 2.1 – Introduction | 13 |
| 2.2 – X-ray Diffraction | 13 |
| 2.2.1 – Background on X-ray Diffraction | 15 |
| 2.2.2 – Sources of X-rays | 18 |
| 2.2.3 – Single Crystal X-ray Diffraction | 20 |
| 2.2.4 – Powder X-ray Diffraction | 21 |
| 2.3 – Thermal Analysis | 25 |
| 2.3.1 – Differential Scanning Calorimetry | 25 |
| 2.3.2 – Thermogravimetric Analysis | 27 |
| 2.4 – References | 28 |

Chapter 3 – Structural Properties and Solid-State Decomposition Behaviour of α,ω -Diaminoalkane/ Urea Inclusion Compounds

| | |
|---|----|
| 3.1 – Introduction | 30 |
| 3.2 – Experimental | 37 |
| 3.3 – 1,6-Diaminohexane/Methanol/Urea | 38 |
| 3.4 – Decomposition Behaviour | 43 |
| 3.4.1 – Introduction | 43 |
| 3.4.2 – 1,7-Diaminoheptane/Methanol/Urea Inclusion Compound | 44 |
| 3.4.3 – 1,8-Diaminooctane/Methanol/Urea Inclusion Compound | 47 |
| 3.4.4 – 1,9-Diaminononane/Methanol/Urea Inclusion Compound | 49 |
| 3.4.5 – 1,10-Diaminodecane/Methanol/Urea Inclusion Compound | 51 |
| 3.4.6 – 1,12-Diaminododecane/Methanol/Urea Inclusion Compound | 53 |
| 3.5 – Conclusions and Future Work | 56 |
| 3.6 – References | 59 |

Chapter 4 – X-ray Dichroism and X-ray Birefringence in Thiourea Inclusion Compounds

| | |
|---|----|
| 4.1 – Introduction | 60 |
| 4.2 – Experimental | 66 |
| 4.3 – 1-Bromoadamantane / Thiourea Inclusion Compound | 70 |
| 4.4 – 2-Bromoadamante / Thiourea Inclusion Compound | 73 |
| 4.5 – Bromocyclohexane / Thiourea Inclusion Compound | 79 |
| 4.6 – Conclusions and Future Work | 90 |
| 4.7 – References | 92 |

Chapter 5 – Solid State Reaction and Polymorphism of Oxalyl Dihydrazide at High Temperature

| | |
|---|-----|
| 5.1 – Introduction | 93 |
| 5.2 – Experimental | 100 |
| 5.3 – Results | 103 |
| 5.4 – Conclusions and Future Work | 111 |
| 5.5 – References | 113 |

Chapter 6 – Solid-State Dehydration of *t*-Butylammonium Acetate Monohydrate

| | |
|------------------------------------|-----|
| 6.1 – Introduction | 114 |
| 6.2 – Experimental | 116 |
| 6.3 – Structure Determination..... | 119 |
| 6.4 – Results and Discussion | 126 |
| 6.5 – References | 133 |

Appendix A – Crystal data for 1,6-DAHx/MeOH/Urea.....

Appendix B – Crystal data for 2-BA/TIC

Appendix C – Crystal data for BCHx/TIC

Appendix D – Solid-State Reaction and Polymorphism of ODH

Appendix E – Crystal data for TBAMH

Chapter 1

Introduction

1.1 – Solid Inclusion Compounds

Solid inclusion compounds comprise two constituents: the host and the guest.

The host operates as a framework with empty spaces where the guest molecules are included. The host structures in solid inclusion compounds comprise two different kinds [1, 2]: hard hosts and soft hosts, depending on their response when the guest is removed. Hard hosts are stable regardless of whether the guest is included within them or not. Zeolites are an example of hard hosts, where the framework is built from corner-sharing SiO_4 and AlO_4 tetrahedra, with the cavities in these materials ranging from cages and tunnels to 2-D and 3-D networks. Their main applications are in catalysis and separation technologies. In contrast, soft hosts are not stable when the guest molecules are removed, and collapse, in most cases irreversibly.

Chapters 3 and 4 are focused on one-dimensional, soft-host solid inclusion compounds, specifically urea inclusion compounds and thiourea inclusion compounds [3-6] (*Figure 1.1*).

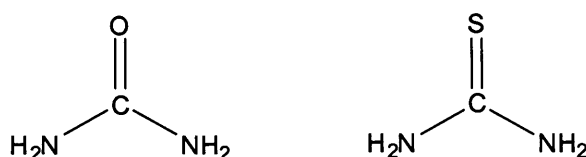


Figure 1.1 Urea (left) and thiourea (right) molecules.

1.1.1 – Urea Inclusion Compounds

Urea inclusion compounds (UICs) were discovered by Bengen in 1940 [7]. These compounds are host-guest systems in which the host is formed by a hydrogen-bonded arrangement of urea molecules, within which there are infinite, uni-directional, parallel, hexagonal tunnels, and the guest molecules are densely packed inside these urea tunnels (in the absence of the guest, urea recrystallizes in a tetragonal crystal structure $P\bar{4}2_1m$, $a = 5.6 \text{ \AA}$ and $c = 4.7 \text{ \AA}$ [8]). In the urea tunnel structure, the oxygen atom of each urea molecule is hydrogen bonded to four nitrogen atoms (from four different urea molecules) and each nitrogen atom is hydrogen bonded to two oxygen atoms (from two different urea molecules) [9]. The diameter of the urea tunnels varies from 5.5 \AA to 5.8 \AA [10]. The comparatively

narrow tunnel diameter limits the type of guest molecules that can be included (typically long n-alkane chains with a small degree of substitution).

All “conventional” UICs (the majority of the UICs are classed as conventional) have the same hexagonal host structure at room temperature, with either space group $P6_122$ (right handed) or $P6_522$ (left handed) and lattice parameters: $a = b \approx 8.22 \text{ \AA}$, $c \approx 11.01 \text{ \AA}$, $\alpha = \beta = 90^\circ$ and $\gamma = 120^\circ$ [11, 12] (Figure 1.1).

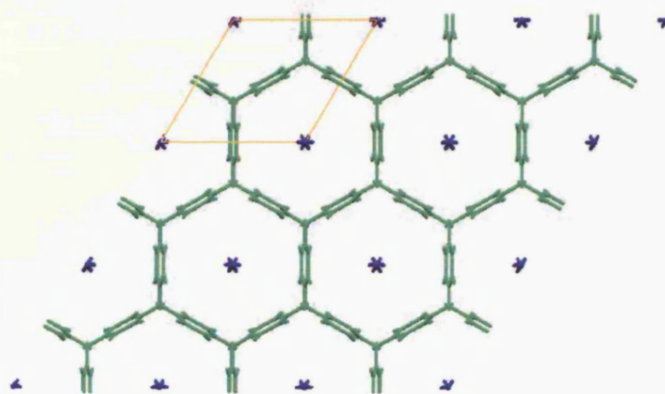


Figure 1.1 View along the c -axis of the hexagonal host structure of UICs (in green urea molecules and in blue the guest molecules).

Conventional UICs have an incommensurate relationship (Figure 1.2) between the periodicities of the host C_h and guest C_g substructures along the tunnel [13, 14], which means there are no small integers p and q that satisfy the equation: $pC_g = qC_h$, i.e., the ratio C_g/C_h is not a rational number with a sufficiently small denominator. Thus, the position of the guest molecules in relation to the unit cell of the host

substructure varies along the tunnel. For a small number of UICs, on the other hand, the equation above is satisfied (and thus each guest molecule has a fixed position with respect to the unit cell of the host substructure), and these materials have a commensurate relationship.

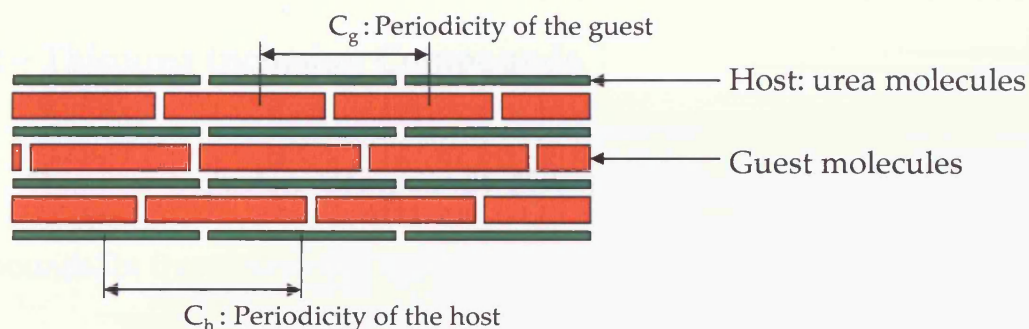


Figure 1.2 Schematic representation of the periodicities of the urea substructure (in green) and the guest molecules (in orange).

Conventional UICs at room temperature usually exhibit substantial dynamic disorder of the guest molecule around the tunnel axis. However, on lowering the temperature, UICs generally undergo a phase transition to a lower symmetry than hexagonal and experience an increase in the ordering of the guest molecules.

UICs have been a subject of interest for their physico-chemical properties, including incommensurate structural properties [13-17], dynamic properties [18-23], host-guest chiral recognition [24, 25], order disorder phase transitions [26-31], ferroelastic properties [32, 33] and properties related to one-dimensional confinement [34-36].

In the present work, we concentrate on a particular type of non-conventional UIC, a layered UIC formed with α,ω -diaminoalkane as the guest molecules and methanol. A more detailed description of these compounds and their properties, focusing on their stability at room temperature, is given in Chapter 3.

1.1.2 – Thiourea Inclusion Compounds

Thiourea Inclusion Compounds (TICs) [3, 37] are also soft-host inclusion compounds. In these materials, the thiourea molecules are hydrogen bonded to each other to form the walls of the tunnels (*Figure 1.3*). The tunnel diameter varies from 5.8 Å to 7.1 Å, creating an internal surface that has significant variation in tunnel diameter on moving along the tunnel, as seen in *Figure 1.4*. For that reason, TICs are often considered as cage-like inclusion compounds.

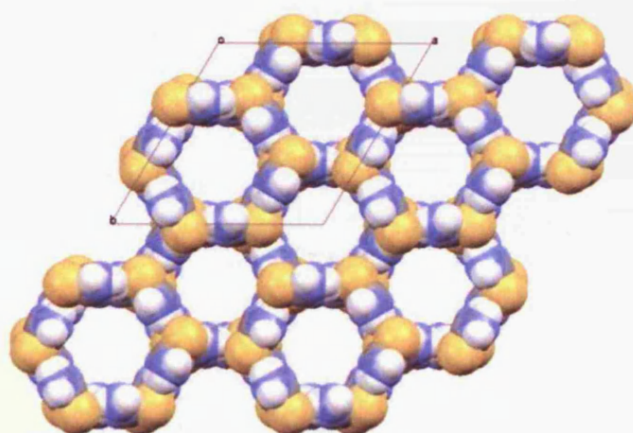


Figure 1.3 Projection of the thiourea host structure viewed along the tunnel axis.

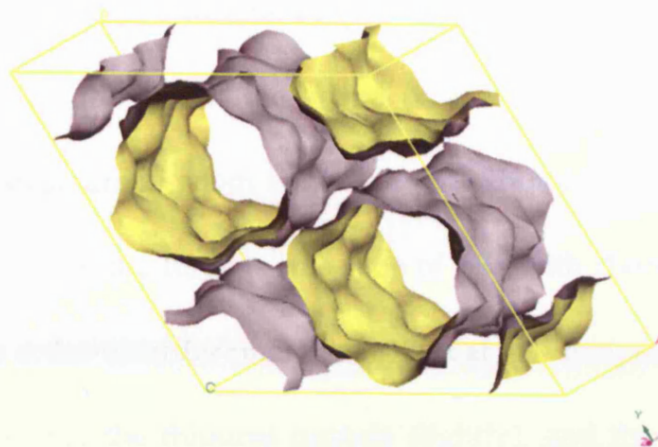


Figure 1.4 Detail of the internal surface of the thiourea tunnel structure.

These constrictions within the tunnels are important for locking the guest molecules into certain positions along the tunnel, and thus TICs are usually commensurate structures. As the TIC tunnel is wider than the UIC tunnel, these inclusion compounds can accommodate guest molecules of different shape and size such as cyclohexane and derivatives, ferrocene and compounds containing aromatic rings (Figure 1.5).

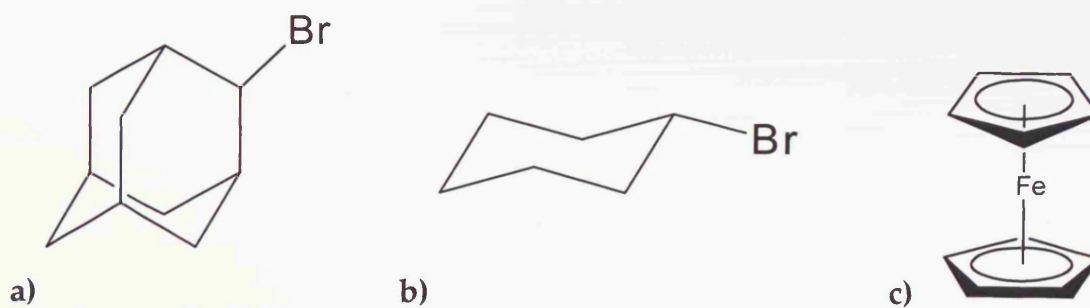


Figure 1.5 Some guest molecules in thiourea inclusion compounds. (a) 1-bromoadamantane, (b) bromocyclohexane and (c) ferrocene.

Generally, there are two different types of thiourea host structure, depending on the included guest [4]. When the shape of the guest molecule is essentially isotropic, the host structure at room temperature is rhombohedral and the guest is usually disordered inside the tunnel. This type of TIC with rhombohedral structure often undergoes an order-disorder phase transition at low temperature (lowering the symmetry and distorting the thiourea tunnels slightly), and the guest molecules in the low temperature phase become ordered. In Chapter 4, this issue is discussed in detail, as we focus on the bromocyclohexane/thiourea inclusion compound phase transition at low temperature. The other type of thiourea host structure, formed with planar molecules, is monoclinic and the guest is typically ordered.

1.1.3 – Applications

Some of the applications of UICs and TICs involve the control of crystal morphology [38, 39]. Although conventional UICs normally grow as long needles, the crystal growth can be controlled by using an inhibitor to obtain flat hexagonal plates instead. Guest exchange processes have also been explored for UICs [35, 40-44], with *in situ* and *ex situ* studies demonstrating that there is guest transport along the tunnel driven by thermodynamic considerations. Another important application is to utilize UICs and TICs as X-ray dichroic filter materials [45-47], which is discussed thoroughly in Chapter 4.

1.2 – Solid-State Structural Transformations

Crystalline organic materials may experience different types of structural transformations [48-52], including polymorphic transformations, solid-state reactions, processes involving solvent exchange, formation of new materials by solid-state grinding (mechanochemical synthesis) and solvation or desolvation among solvate and non-solvate forms.

Polymorphism of oxalyl dihydrazide (for which five polymorphs α , β , γ , δ and ϵ have been reported [53]) is examined in detail in Chapter 5, including discussion of the relative stability of the polymorphs and investigations of a solid-state reaction that takes place at high temperature in these materials.

A solid-state dehydration process involving solid *t*-butylammonium acetate monohydrate is described comprehensively in Chapter 6 [54]. This process involves the transformation of a single crystal of *t*-butylammonium acetate monohydrate to a microcrystalline powder of an anhydrous product phase, involving substantial rearrangement of the hydrogen bonding scheme.

1.3 – References

- [1] K. D. M. Harris, *Monographs on Chemistry for the 21st Century: Interfacial Chemistry*, 21-55, I.U.P.A.C. Blackwell Science, (1997)
- [2] K. D. M. Harris, *J. Chin. Chem. Soc.*, **46**, 5-22 (1999)
- [3] M. D. Hollingsworth and K. D. M. Harris, *Comprehensive Supramolecular Chemistry*, Vol. 6, 177-238, Pergamon Press: Oxford, (1996)
- [4] K. D. M. Harris, *Supramol. Chem.*, **19**, 47-53 (2007)
- [5] K. D. M. Harris, *Chem. Soc. Rev.*, **26**, 279-289 (1997)
- [6] K. D. M. Harris, *J. Mol. Struct.*, **374**, 241-250 (1996)
- [7] M. F. Bengen, *Ger. Pat. Appl.*, OZ 123438 (1940)
- [8] K. D. M. Harris, *J. Phys. Chem. Solids*, **53**, 529-537 (1992)
- [9] V. W. Bhatnagar, *J. Struct. Chem.*, **8**, 513-529 (1967)
- [10] A. R. George and K. D. M. Harris, *J. Mol. Graph.*, **13**, 138-141 (1995)
- [11] A. E. Smith, *Acta Cryst.*, **5**, 224 (1952)
- [12] K. D. M. Harris and J. M. Thomas, *J. Chem. Soc. Faraday Trans.*, **86**, 2985-2996 (1990)
- [13] A. J. O. Rennie and K. D. M. Harris, *Proc. R. Soc. London Ser. A Math. Phys. Eng. Sci.*, **430**, 615-640 (1990)
- [14] A. J. O. Rennie and K. D. M. Harris, *Chem. Phys. Lett.*, **188**, 1-4 (1992)
- [15] K. D. M. Harris and M. D. Hollingsworth, *Proc. R. Soc. London Ser. A Math. Phys. Eng. Sci.*, **431**, 245-269 (1990)
- [16] R. Lefort, J. Etrillard, B. Toudic, F. Guillaume, T. Brezowski and P. Bourges, *Phys. Rev. Lett.*, **77**, 4027 (1996)
- [17] T. Weber, H. Boysen, F. Frey and R. B. Neder, *Acta Cryst. B*, **53**, 544-552 (1997)
- [18] H. L. Casal, D. G. Cameron and E. C. Kelusky, *J. Chem. Phys.*, **80**, 1407 (1984)

- [19] K. D. M. Harris and P. Jonsen, *Chem. Phys. Lett.*, **154**, 593-598 (1989)
- [20] A. El Baghdadi, E. J. Dufourc and F. Guillaume, *J. Phys. Chem.*, **100**, 1746-1752 (1996)
- [21] F. Guillaume, C. Sourisseau and A.-J. Dianoux, *J. Chim. Phys. (Paris)*, **88**, 1721 (1991)
- [22] F. Guillaume, S. P. Smart, K. D. M. Harris and A. J. Dianoux, *J. Phys.: Condens. Matter*, **6**, 2169-2184 (1994)
- [23] P. Girard, A. E. Aliev, F. Guillaume, K. D. M. Harris, M. D. Hollingsworth, A. J. Dianoux and P. Jonsen, *J. Chem. Phys.*, **109**, 4078-4089 (1998)
- [24] R. Arad-Yellin, B. S. Green, M. Knossow and G. Tsoucaris, *Inclusion compounds*, Vol. 3, 263, Academic Press: New York, (1984)
- [25] L. Yeo and K. D. M. Harris, *J. Chem. Soc. Faraday Trans.*, **94**, 1633-1639 (1998)
- [26] L. Yeo, B. M. Kariuki, H. SerranoGonzalez and K. D. M. Harris, *J. Phys. Chem. B*, **101**, 9926-9931 (1997)
- [27] N. G. Parsonage and R. C. Pemberton, *Trans. Faraday Soc.*, **63**, 311-328 (1967)
- [28] Y. Chatani, Y. Taki and H. Tadokoro, *Acta Cryst. B*, **33**, 309-311 (1977)
- [29] K. Fukao, *J. Chem. Phys.*, **92**, 6867 (1990)
- [30] R. M. Lynden-Bell, *Mol. Phys.*, **79**, 313 (1993)
- [31] H. Le Lann, C. Odin, B. Toudic, J. C. Ameline, J. Gallier, F. Guillaume and T. Brezczewski, *Phys. Rev. B*, **62**, 5442 (2000)
- [32] M. E. Brown and M. D. Hollingsworth, *Nature*, **376**, 323-327 (1995)
- [33] M. D. Hollingsworth, M. L. Peterson, J. R. Rush, M. E. Brown, M. J. Abel, A. A. Black, M. Dudley, B. Raghothamachar, U. Werner-Zwanziger, E. J. Still and J. A. Vanecko, *Cryst. Growth Des.*, **5**, 2100-2116 (2005)
- [34] M. D. Hollingsworth and N. Cyr, *Mol. Cryst. Liq. Cryst.*, **187**, 135 - 144 (1990)
- [35] A. A. Khan, S. T. Bramwell, K. D. M. Harris, B. M. Kariuki and M. R. Truter, *Chem. Phys. Lett.*, **307**, 320-326 (1999)

- [36] M. H. Chao, K. D. M. Harris, B. M. Kariuki, C. L. Bauer and B. M. Foxman, *J. Phys. Chem. B*, **106**, 4032-4035 (2002)
- [37] K. Takemoto and N. Sonoda, *Inclusion Compounds*, Vol. 2, 47, Academic Press: New York, (1984)
- [38] S. O. Lee and K. D. M. Harris, *Chem. Phys. Lett.*, **307**, 327-332 (1999)
- [39] N. E. Kelly, S. O. Lee and K. D. M. Harris, *J. Am. Chem. Soc.*, **123**, 12682-12683 (2001)
- [40] J. Marti-Rujas, K. D. M. Harris, A. Desmedt and F. Guillaume, *J. Phys. Chem. B*, **110**, 10708-10713 (2006)
- [41] J. Marti-Rujas, K. D. M. Harris and A. Desmedt, *Mol. Cryst. Liq. Cryst.*, **456**, 139-147 (2006)
- [42] J. Marti-Rujas, A. Desmedt, K. D. M. Harris and F. Guillaume, *J. Phys. Chem. C*, **113**, 736-743 (2008)
- [43] J. Marti-Rujas, A. Desmedt, K. D. M. Harris and F. Guillaume, *J. Phys. Chem. B*, **111**, 12339-12344 (2007)
- [44] J. Marti-Rujas, A. Desmedt, K. D. M. Harris and F. Guillaume, *J. Am. Chem. Soc.*, **126**, 11124-11125 (2004)
- [45] S. P. Collins, D. Laundy, K. D. M. Harris, B. M. Kariuki, C. L. Bauer, S. D. Brown and P. Thompson, *J. Phys.: Condens. Matter*, **14**, 123-134 (2002)
- [46] M. H. Chao, B. M. Kariuki, K. D. M. Harris, S. P. Collins and D. Laundy, *Angew. Chem. Int. Ed.*, **42**, 2982-2985 (2003)
- [47] N. P. Bannister, K. D. M. Harris, S. P. Collins, A. Martindale, P. S. Monks, G. Solan and G. W. Fraser, *Exp. Astron.*, **21**, 1-12 (2006)
- [48] J. M. Thomas, *Phil. Trans. Roy. Soc. A*, **277**, 251 (1974)
- [49] J. D. Dunitz, *Acta Cryst. B*, **51**, 619 (1995)
- [50] J. Bernstein, *Polymorphism in Molecular Crystals*, Oxford University Press, Oxford, (2002)
- [51] D. Braga and F. Grepioni, *Chem. Commun.*, 3635 (2005)

- [52] F. H. Herbstein, *Acta Cryst. B*, **62**, 341 (2006)
- [53] S. Y. Ahn, F. Guo, B. M. Kariuki and K. D. M. Harris, *J. Am. Chem. Soc.*, **128**, 8441-8452 (2006)
- [54] J. Marti-Rujas, A. Morte-Ródenas, F. Guo, N. Thomas, K. Fujii, B. M. Kariuki and K. D. M. Harris, *Cryst. Growth Des.*, **10**, 3176-3181 (2010)

Chapter 2

Experimental techniques

2.1 – Introduction

This chapter provides the theoretical background for the techniques used during this research project, namely single crystal X-ray diffraction, powder X-ray diffraction, and thermal analysis [differential scanning calorimetry (DSC) and thermogravimetric analysis (TGA)].

2.2 – X-ray Diffraction

X-ray diffraction is a powerful technique used to determine crystal structures (spatial atomic distribution) of crystalline solids, which involves determination of the unit cell parameters [the unit cell axis lengths a , b and c and the unit cell angles α , β

and γ (Figure 2.1)] and the atomic content of the unit cell [described by the atomic coordinates $(x_1, y_1, z_1), (x_2, y_2, z_2), \dots, (x_n, y_n, z_n)$]. Identifying the unit cell and its contents gives us knowledge of the complete crystal structure since the unit cell (which contains the full symmetry of the crystal structure) is repeated in all dimensions of the crystal due to the crystal periodicity. Crystalline solids belong to one of the 7 crystallographic systems (triclinic, monoclinic, orthorhombic, tetragonal, trigonal, hexagonal and cubic) and are arranged in the space in a symmetry defined by one of the 230 space groups.

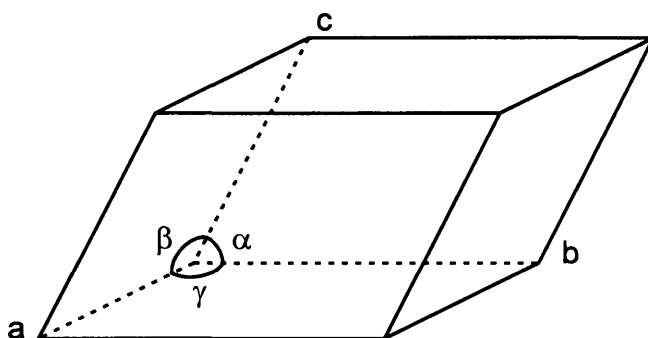


Figure 2.1 Representation of a unit cell.

From the diffraction pattern, the crystal lattice can be identified. The angles of the reflections allow the unit cell parameters (dimensions and angles) to be determined, while the relative intensities of the reflections provide information about the atomic content of the unit cell.

2.2.1 – Background on X-ray Diffraction

X-ray diffraction was discovered by von Laue in 1912, for which he was awarded the Nobel Prize in Physics in 1914. Bragg's law [1] describes the geometric conditions (*Figure 2.2*) that must be satisfied to observe a diffracted X-ray beam. To observe a diffraction maximum (i.e. a peak in a diffraction pattern), a constructive interference of the diffracted beams is necessary. Therefore, the diffracted beams must be in phase (Equations 2.1-2.4). To have the diffracted beams in phase, the path difference between beams (Equation 2.2) must be an integer (n) multiple of the wavelength λ . The angle θ is known as the Bragg angle and d_{hkl} is the inter-planar spacing.

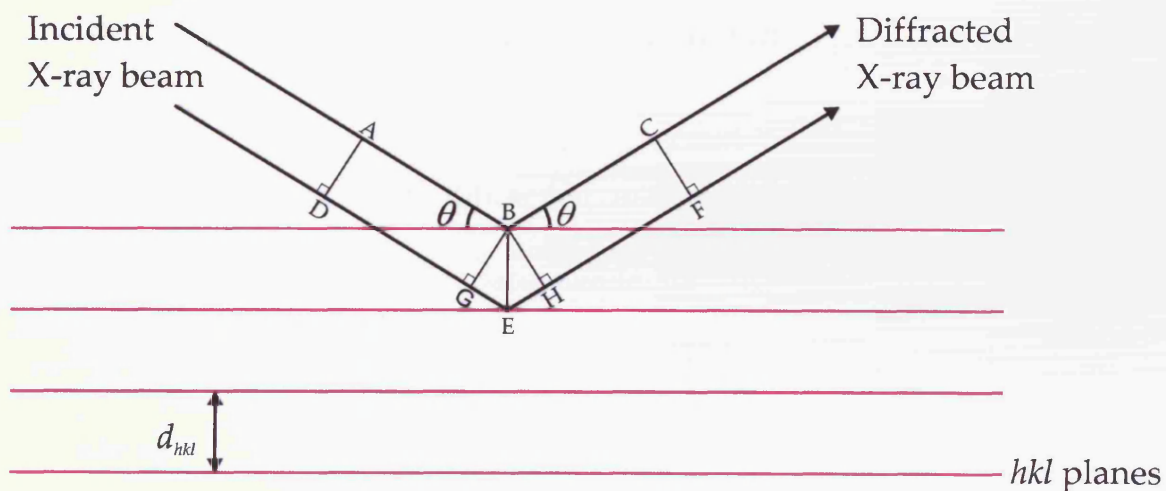


Figure 2.2 Diffraction of X-rays from lattice planes illustrating the Bragg's law.

$$\sin \theta = \frac{GE}{d_{hkl}} \quad ; \quad \sin \theta = \frac{EH}{d_{hkl}} \quad (2.1)$$

$$\text{Path difference} = GE + EH = d_{hkl} \sin \theta + d_{hkl} \sin \theta \quad (2.2)$$

$$\text{For constructive interference: } GE + EH = n\lambda \quad (2.3)$$

$$n\lambda = 2d_{hkl} \sin \theta \quad (2.4)$$

The crystal structure (specifically, the electron density, $\rho(\mathbf{r})$, as described by the atom positions and displacements parameters) is related to its X-ray diffraction pattern by the structure factor $F(\mathbf{H})$ (Equation 2.5).

$$\begin{aligned} F(\mathbf{H}) &= |F(\mathbf{H})| \exp[i\alpha(\mathbf{H})] \\ &= \int \rho(\mathbf{r}) \exp[2\pi i \mathbf{H} \cdot \mathbf{r}] d\mathbf{r} \end{aligned} \quad (2.5)$$

In this equation, each diffraction maximum corresponds to a value of $\mathbf{H} = h\mathbf{a}^* + k\mathbf{b}^* + l\mathbf{c}^*$ in reciprocal space, while for each atom there is a value of $\mathbf{r} = x\mathbf{a} + y\mathbf{b} + z\mathbf{c}$ in direct space. $|F(\mathbf{H})|$ is the amplitude and $\alpha(\mathbf{H})$ is the phase. The amplitude can be obtained from the X-ray diffraction pattern and is related to the intensities, $I(\mathbf{H})$, by $I(\mathbf{H}) \propto |F(\mathbf{H})|^2$. From the crystal structure, the diffraction pattern can be calculated using a forward Fourier Transform. However, the phases of the diffraction maxima $\alpha(\mathbf{H})$ cannot be extracted from the experimental data, which is

known as the “phase problem”. As a consequence, the inverse Fourier transform (Equation 2.6) cannot be performed, as it requires information about the phases (Figure 2.3).

$$\rho(\mathbf{r}) = \frac{1}{V} \sum_{\mathbf{H}} |F(\mathbf{H})| \exp[i\alpha(\mathbf{H}) - 2\pi i \mathbf{H} \cdot \mathbf{r}] \quad (2.6)$$

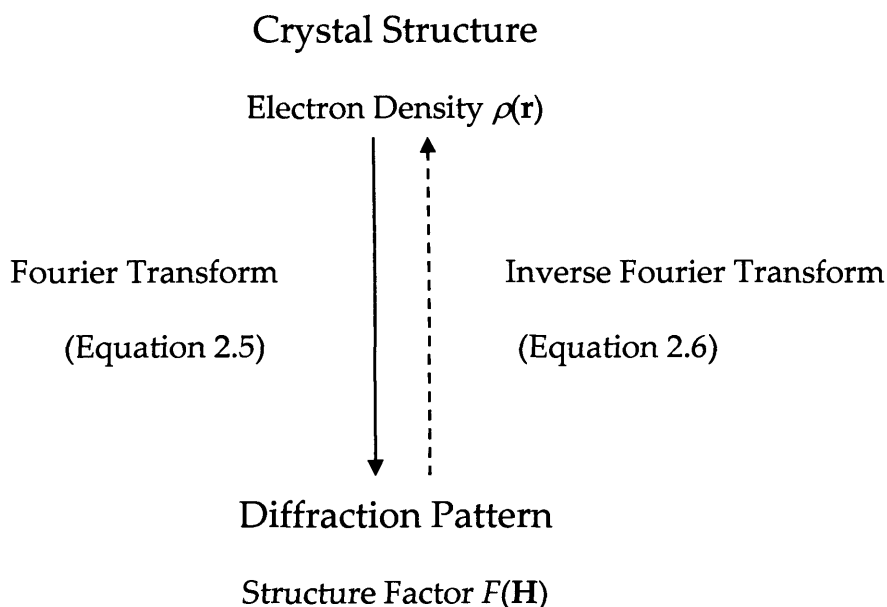


Figure 2.3 Diagram illustrating the phase problem.

There are basically two main, traditional approaches to overcome this problem in structure solution for small-molecule single-crystal X-ray crystallography: the Patterson Synthesis and Direct Methods. In Patterson Synthesis, the amplitudes $|F(\mathbf{H})|$ in Equation 2.5 are replaced by their squares $|F(\mathbf{H})|^2$ and the unknown phases are omitted. The peaks in a Patterson map correspond to vectors between pairs of atoms in the structure. It is mostly used for structures containing a few heavy

atoms (atoms with a high number of electrons) among many light atoms. Direct Methods, preferred at present, attempt to derive the structure factor phases, electron density or atomic coordinates by mathematical means from a single set of X-ray intensities. With Direct Methods, the approximate phases can be estimated from relationships between the structure factors with no previous knowledge about the crystal structure itself. On the other hand, for powder X-ray structure determination direct-space [2] approach methods are mostly used as the reliability of the extracted intensities is limited by peak overlapping in the powder X-ray diffraction patterns (See section 2.2.4).

2.2.2 –Sources of X-rays

X-rays were discovered by W.C. Röntgen in 1895. The X-ray wavelengths (λ) range from 0.1 to 100 Å, and lie in the electromagnetic spectrum between γ -rays and UV radiation. Longer wavelength X-rays have medical applications, whereas shorter wavelength X-rays (0.25 - 2.5 Å) are used for X-ray diffraction. Such wavelengths are of a similar order of magnitude to the periodic repeat distances in crystalline solids, and thus a crystal behaves as a diffraction grating for such X-rays.

X-rays in laboratories are produced in a vacuum tube in which a voltage is applied between the anode (usually a metal such as copper or molybdenum) and the

cathode. Electrons from the cathode collide with the anode, removing electrons from the anode's internal K shell. The vacancies left are subsequently filled with electrons from external shells (L or M) with a resulting emission of energy as X-rays. The wavelength of the X-rays produced depends on the composition of the anode and on the transition that has taken place: $L \rightarrow K$ ($K\alpha$) and $M \rightarrow K$ ($K\beta$). $K\alpha$, which is not monochromatic (as it comprises two components: $K\alpha_1$ and $K\alpha_2$ due to the energy differences in spin states), is more intense, and thus is the one used for X-ray production in laboratories. To produce monochromatic $K\alpha_1$ radiation, the X-rays are passed through a monochromator. The copper anode, with longer wavelength ($K\alpha_1$, $\lambda = 1.54056 \text{ \AA}$), is usually used in powder X-ray diffraction as it resolves the peaks better and the molybdenum anode, with shorter wavelength ($K\alpha$, $\lambda = 0.7107 \text{ \AA}$), is mostly used in single crystal X-ray diffraction.

Another X-ray source is the synchrotron. Much of the work reported here has employed synchrotron X-ray radiation, based on exploiting a number of special properties of synchrotron X-rays. Electrons, generated initially in an electron gun, are accelerated to very high speeds (nearly the speed of light) by particle accelerators and steered around a storage ring by bending magnets. When the magnets bend the path of the electron beam, very intense X-ray, UV and Infra-Red light are emitted. The very high intensity of the X-rays from a synchrotron radiation source makes possible the study of systems in which rapid transformations occur and short data

collection times are needed. In addition, synchrotron radiation produces diffraction data of higher resolution and improved signal-to-noise. The wavelength is tunable depending on the station/beamline, and the angular divergence is very low (thus giving very high resolution diffraction data). Synchrotron radiation is polarized horizontally (electric vector component vibrating in the horizontal plane), an indispensable property necessary to perform the X-ray dichroism and birefringence experiments discussed in Chapter 4. Two different synchrotron facilities were used during this research, Daresbury SRS and Diamond Light Source. As the experimental set up in the synchrotron varies a lot depending on the specific type of experiment and on the particular station/beamline used, the specific experimental set up details used for our experiments are described in the experimental sections of the relevant chapters.

2.2.3 – Single Crystal X-ray Diffraction

Single crystal diffraction data in this thesis were collected on a Nonius Kappa CCD diffractometer using monochromated MoK α radiation ($\lambda = 0.71073 \text{ \AA}$) in the School of Chemistry of Cardiff University. Crystals were mounted on a glass fibre with the aid of perfluoroether oil. Data collection was carried out using COLLECT [3], crystal structure solution was carried out with direct methods using SHELXS [4] and crystal structure refinement using SHELXL [4] via the software interface

WinGX [5]. The figure-of-merit used to evaluate the refinement quality and therefore the accuracy of the crystal structure obtained is the R -factor (R) (Equation 2.7) and the weighted R -factor (R_w) (Equation 2.8):

$$R = 100 \times \frac{\sum ||F_o| - |F_c||}{\sum |F_o|} \quad (2.7)$$

$$R_w = 100 \times \frac{\sum w||F_o| - |F_c||}{\sum w|F_o|} \quad (2.8)$$

where $|F_o|$ is the observed structure factor amplitude, $|F_c|$ is the calculated structure factor amplitude and w is a weighting factor.

2.2.4 – Powder X-ray Diffraction

Powder X-ray diffraction (PXRD) is a powerful technique for structure determination of crystalline solids that are available as polycrystalline powders. In this technique, the powder sample is irradiated by monochromatic X-ray radiation. When the powder is crystalline, each individual crystallite diffracts X-rays, which are measured by a detector to give a diffraction pattern. The diffraction pattern is plotted as a graph with the x -axis representing the 2θ angle of the diffracted X-rays and the y -axis representing the intensities of these X-rays (*Figure 2.4*). Thus, the powder X-ray

diffraction data is only a one-dimensional representation of the diffraction pattern. As a consequence, structure determination from powder diffraction data is significantly more challenging than from single-crystal diffraction data (which provides a three-dimensional representation of the crystal structure).

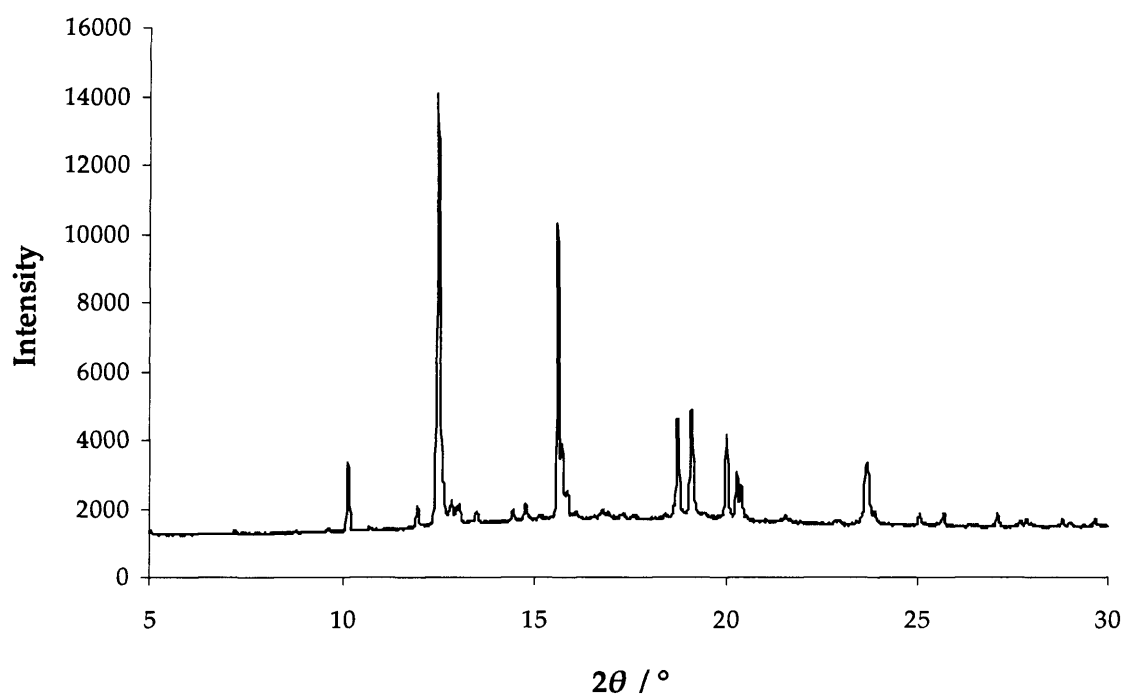


Figure 2.4 Example of a powder X-ray diffraction pattern.

In any given diffraction pattern, the peak positions (2θ) depend on the unit cell parameters and the intensity of each peak depends on the atomic content and its distribution in the unit cell. From this diffraction pattern, the crystal structure can be determined. There are different stages involved the crystal structure determination

from powder X-ray diffraction data: indexing and space group assignment, structure solution and structure refinement.[6-12]

The first step for crystal structure determination is the unit cell determination and space group assignment (indexing), determined from the peak positions and the systematic absences. The indexing of the X-ray powder pattern is assisted by particular software: TREOR [13], ITO [14], DICVOL [15] and CRYSFIRE [16]. Unit cell refinement following the Le Bail [17] technique is carried out using the GSAS [18] software and its graphical user interface editor EXPGUI [19].

The following stage in the crystal structure determination is the structure solution, carried out using the program EAGER [20], based on the Genetic Algorithm, a direct-space [2] approach for structure solution from powder X-ray diffraction data, based on the principles of evolution involving well-known evolutionary operations such as natural selection, mating and mutation. In this strategy, trial structures are generated in direct space, independently of the experimental powder diffraction data, and the suitability of each trial structure is evaluated by direct comparison between the powder diffraction pattern calculated for the trial structure and the experimental powder diffraction pattern. This comparison is quantified using a figure-of-merit, the weighted powder profile R-factor R_{wp} (Equation 2.7), where w_i is a weighting factor for the i^{th} point in the powder pattern, y_i is the intensity of the i^{th} point in the experimental powder

diffraction pattern and y_{ci} is the intensity of the i^{th} point in the calculated powder diffraction pattern. The final stage for structure determination is the structure refinement following the Rietveld Method [21, 22], intended to obtain an accurate crystal structure, using GSAS [18] and EXPGUI [19].

$$R_{wp} = 100 \times \sqrt{\frac{\sum_i w_i (y_i - y_{ci})^2}{\sum_i w_i y_i^2}} \quad (2.9)$$

Powder X-ray Diffraction has some advantages over single crystal X-ray diffraction. Single crystals are not required (polycrystalline powders are analysed with this technique); it also overcomes the problem of crystal twinning (crystal twins contribute to the diffraction as different crystallites, which is not a problem for powder X-ray diffraction data) making it easier to study phase transitions at low temperature which often involve twinning of the crystals. However, there is the difficulty of peak overlapping and preferred orientation, when a peak shows higher intensity than predicted, due to the sample mounting or the anisotropy of crystal orientations in the powder (long needles or flat plate crystals suffer more preferred orientation than more isometric crystals).

Powder X-ray diffraction data included in this work were collected using a Bruker D8 Advance diffractometer operating in transmission mode with Ge-monochromated Cu $K\alpha_1$ radiation ($\lambda = 1.54056 \text{ \AA}$) and a linear position-sensitive

detector covering 12° in 2θ and a step size of 0.0167° . In these transmission measurements, the sample was fixed between two pieces of adhesive tape in a foil-type sample holder. It is important to note that the X-ray scattering from the tape contributes to the measured powder X-ray Diffraction pattern, giving rise to a significant background contribution that resembles the typical scattering from an amorphous component. Synchrotron X-ray powder diffraction data were recorded on Station 6.2 and 9.1 at Daresbury SRS.

2.3 – Thermal Analysis

Two thermal analysis techniques were used during this research project, namely DSC (Differential Scanning Calorimetry) and TGA (Thermogravimetric Analysis).

2.3.1 – Differential Scanning Calorimetry

DSC is a technique that measures the heat flows of a sample and a reference. The instrument used here was a heat flux Q100 DSC from TA Instruments. Important information can be obtained from these experiments such as determining the temperatures associated with phase transitions, decomposition processes, melting and boiling points, crystallisations, etc. The differential calorimeter measures the heat

into or out of a sample, as well as the heat of a sample relative to a reference. When the process is endothermic, the heat flows into the sample, whereas if the process is exothermic, the heat flows out of the sample. The absolute heat flow indicates the heat capacity, and a shift in the heat flow may be a sign of a glass transition (*Figure 2.5*). When there is an exothermic peak, this may be a sign of crystallization, while melting gives an endothermic peak. Higher sample weights and higher rates of cooling/heating increase the sensitivity, whereas lower sample weights and lower cooling/heating rates increase the resolution.

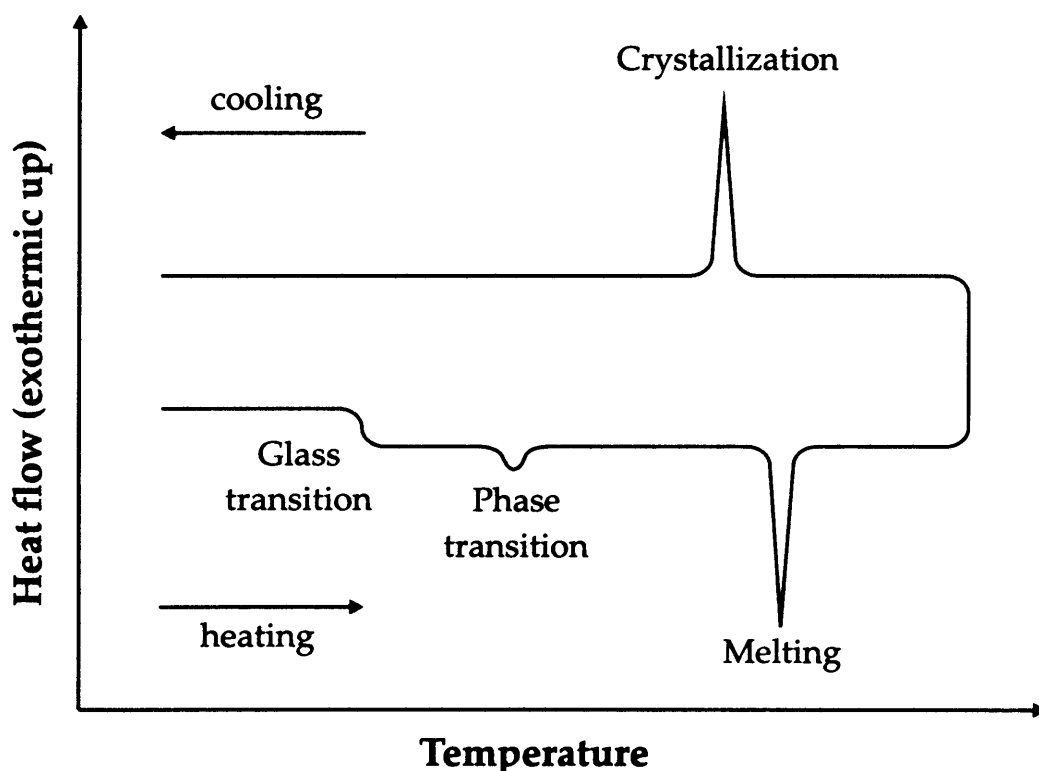


Figure 2.5 Schematic representation of a differential scanning calorimetry graph with different types of transformations indicated.

2.3.2 – Thermogravimetric Analysis

Thermogravimetric Analysis (TGA) is a technique which measures the mass loss of a sample as a function of time or temperature in a controlled environment (Figure 2.6). Useful information can be obtained from this technique about processes such as decomposition, dehydration and sublimation. TGA experiments in this thesis were carried out on a TA Instruments Q600 Simultaneous TGA/DSC instrument.

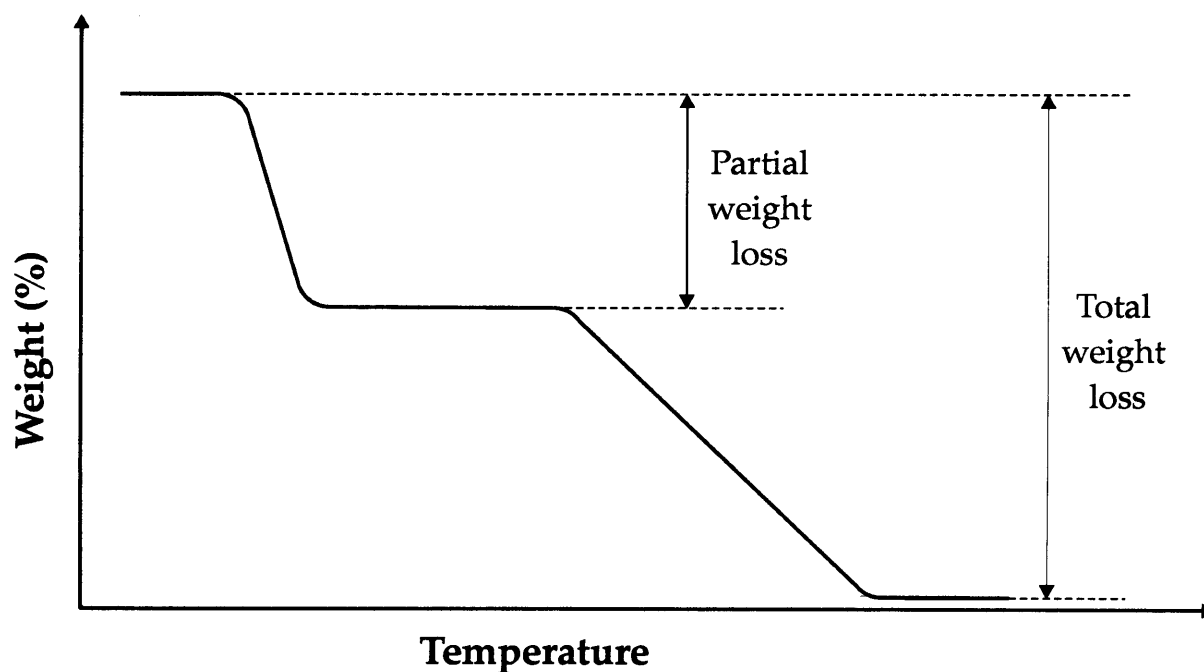


Figure 2.6 Schematic representation of a thermogravimetric analysis graph.

2.4 – References

- [1] W. L. Bragg, *Proc. Camb. Phil. Soc.*, **17**, 43-57 (1913)
- [2] K. D. M. Harris, M. Tremayne, P. Lightfoot and P. G. Bruce, *J. Am. Chem. Soc.*, **116**, 3543-3547 (1994)
- [3] COLLECT, *Enraf-Nonius*, Nonius, B. V., Delft, the Netherlands (1997-2000)
- [4] G. M. Sheldrick, *Acta Cryst. A*, **64**, 112-122 (2008)
- [5] L. J. Farrugia, *J. Appl. Cryst.*, **32**, 837-838 (1999)
- [6] K. D. M. Harris, R. L. Johnston, G. W. Turner, E. Tedesco, E. Y. Cheung and B. M. Kariuki, *15th International Conference on the Chemistry of the Organic Solid State*, 123-129 (2001)
- [7] K. D. M. Harris, M. Tremayne and B. M. Kariuki, *Angew. Chem. Int. Ed.*, **40**, 1626-1651 (2001)
- [8] K. D. M. Harris and E. Y. Cheung, *Organic Process Research & Development*, **7**, 970-976 (2003)
- [9] S. Habershon, E. Y. Cheung, K. D. M. Harris and R. L. Johnston, *J. Phys. Chem. A*, **108**, 711-716 (2004)
- [10] K. D. M. Harris and E. Y. Cheung, *Chem. Soc. Rev.*, **33**, 526-538 (2004)
- [11] K. D. M. Harris, S. Habershon, E. Y. Cheung and R. L. Johnston, *Z. Kristallogr.*, **219**, 838-846 (2004)
- [12] K. D. M. Harris, R. L. Johnston and S. Habershon, *Applications of Evolutionary Computation in Chemistry*, Vol. 110, 55-94, Springer-Verlag Berlin, (2004)
- [13] P. E. Werner, L. Eriksson and M. Westdhal, *J. Appl. Cryst.*, **18**, 367-370 (1985)
- [14] J. W. Visser, *J. Appl. Cryst.*, **2**, 89-95 (1969)
- [15] A. Boulton and D. Louër, *J. Appl. Cryst.*, **24**, 987-993 (1991)
- [16] R. A. Shirley, *CRYSFIRE*, Suite of Programs for Indexing Powder Diffraction Patterns, University of Surrey (2002)

- [17] A. Le Bail, H. Duroy and J. L. Fourquet, *Mat. Res. Bull.*, **23**, 447-452 (1988)
- [18] A. C. Larson and R. B. Von Dreele, *General Structure Analysis System (GSAS)*, Los Alamos National Laboratory, Report LAUR 86-748 (2000)
- [19] B. H. Toby, *J. Appl. Cryst.*, *EXPGUI, a graphical user interface for GSAS*, **34**, 210-213 (2001)
- [20] S. Haberson, G. W. Turner, B. M. Kariuki, E. Y. Cheung, A. Hanson, E. Tedesco, D. Albesa-Jové, M. H. Chao, O. J. Lanning, R. L. Johnston and K. D. M. Harris, *EAGER, Computer Program for Structure Solution from Powder Diffraction Data*, (Cardiff University and University of Birmingham.)
- [21] H. M. Rietveld, *J. Appl. Cryst.*, **2**, 65-71 (1969)
- [22] R. A. Young, "The Rietveld Method", International Union of Crystallography, (1993)

Chapter 3

Structural Properties and Solid-State Decomposition

Behaviour of α,ω -Diaminoalkane/ Urea Inclusion Compounds

3.1 – Introduction

In the attempt to crystallize urea inclusion compounds (UICs) using α,ω -diaminoalkanes as the guest molecules, a special and new type of inclusion compound structure was discovered [1]. As described in Chapter 1, conventional UICs generally have the same characteristics of the host structure regardless of the guest molecule included. However, when the guest molecule is an α,ω -diamino-

alkane, the inclusion compound formed with urea is not a conventional one but a different kind based on a layered structure (Figure 3.1), with methanol molecules (the solvent used for crystal growth) incorporated into this structure.

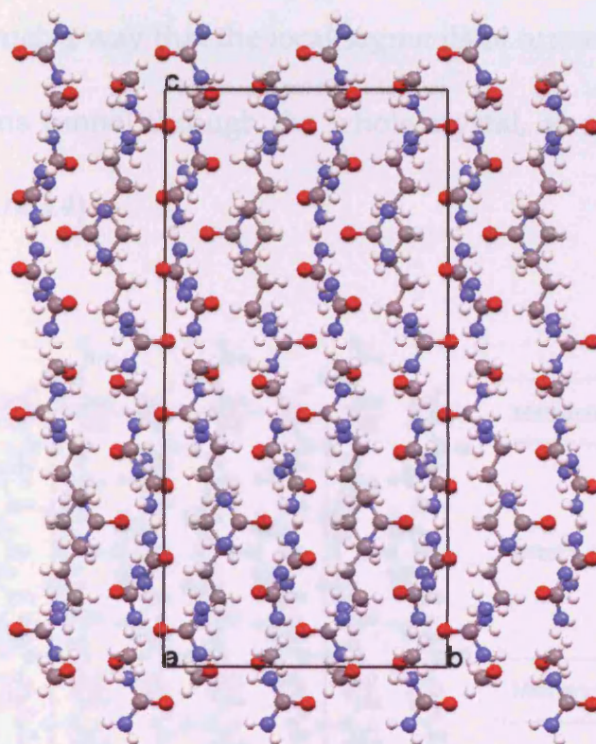


Figure 3.1 View along the *a*-axis of the 1,7-diaminoheptane/methanol/urea inclusion compound.

These materials are constructed by two types of layers: host-guest layers and methanol layers. The former consist of local segments of urea tunnel structure, with hydrogen bonding similar to the conventional UICs, and with a layer thickness that

is approximately the length of one guest molecule. The latter are the methanol layers which consist solely of methanol molecules.

There is an alternation of host-guest layers and methanol layers throughout the crystal (Figure 3.2). The methanol layers interrupt the urea tunnels in between the host-guest layers in such a way that the local segments of tunnel in adjacent layers do not form a continuous tunnel through the whole crystal, as occurs in conventional UICs (Figure 3.3, Figure 3.4).

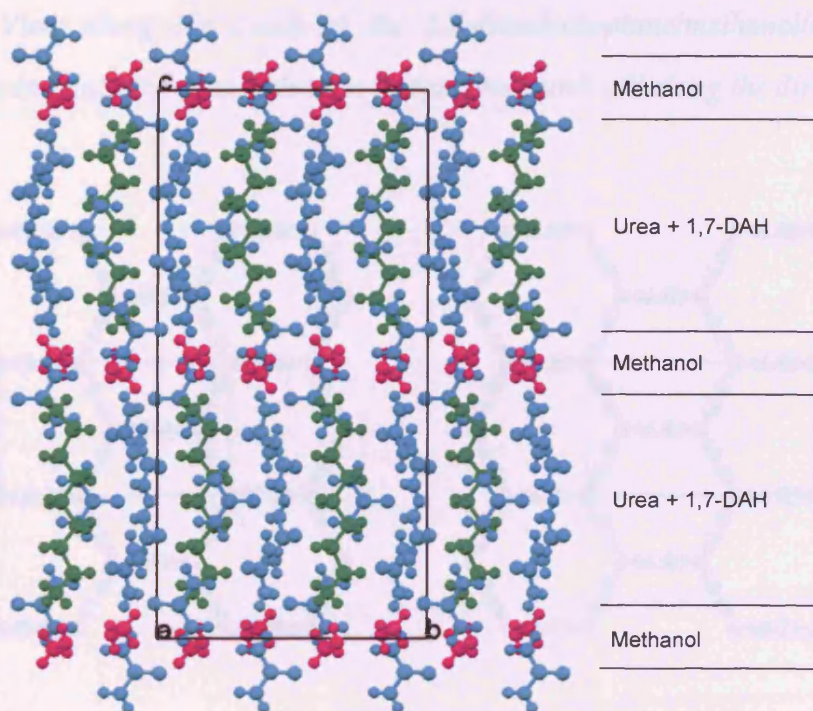


Figure 3.2 View along the *a*-axis of the 1,7-diaminoheptane/methanol/urea inclusion compound unit cell. Urea in cyan, 1,7-diaminoheptane (1,7-DAH) in green and methanol in magenta.

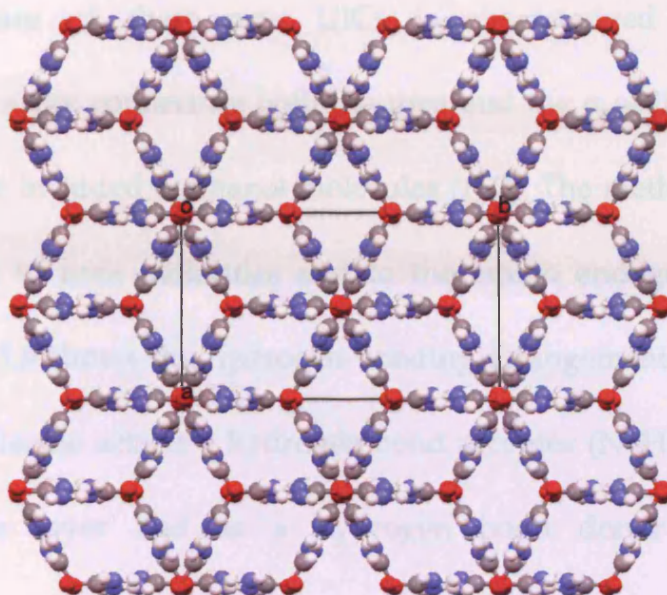


Figure 3.3 View along the c -axis of the 1,7-diaminoheptane/methanol/urea inclusion compound showing only the urea molecules in one whole unit cell along the direction of view.

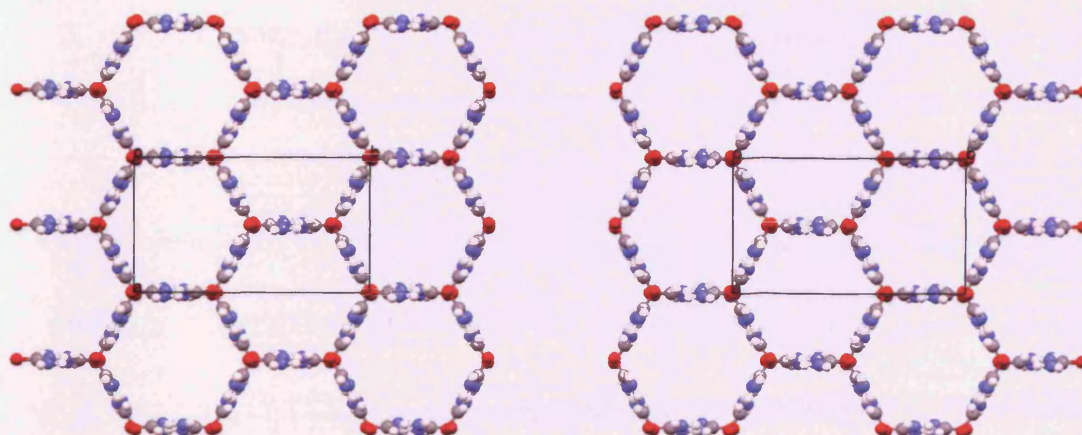


Figure 3.4 View along the c -axis of the 1,7-diaminoheptane/methanol/urea inclusion compound showing the local segments of urea molecules, with the z -coordinate along the c -axis between 0 and 0.5 on the left and between 0.5 and 1 on the right.

The structure of these new UICs is characterized by an extended hydrogen-bonded array connecting both the urea and the α,ω -diaminoalkane guest molecules with the included methanol molecules [1, 2]. The methanol molecules are hydrogen bonded to urea molecules and to the amino end groups of the guest molecules. *Figure 3.5* shows the hydrogen bonding arrangement in these materials; each methanol molecule acts as a hydrogen bond acceptor ($\text{N-H}\cdots\text{O}$) from two urea molecules in one layer and as a hydrogen bond donor ($\text{O-H}\cdots\text{N}$) to an α,ω -diaminoalkane molecule (in this case 1,7-diaminoheptane) in the other layer. In contrast, for conventional UICs, there is no hydrogen bonding between the guest molecules and the urea molecules in the host structure.

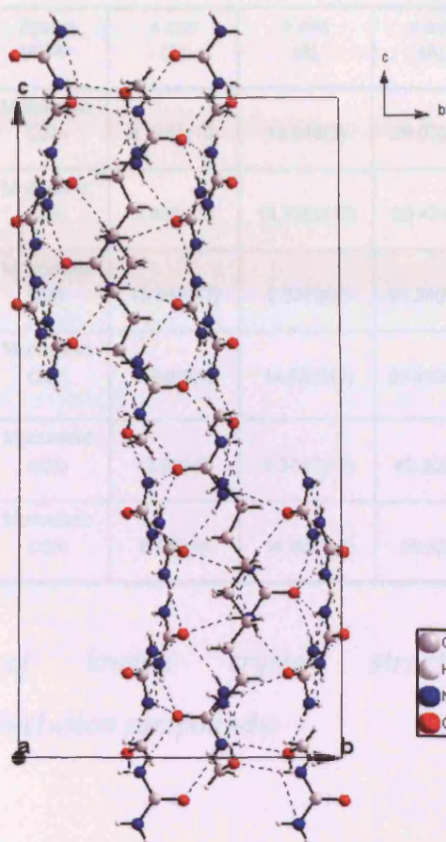


Figure 3.5 View along the *a*-axis of the 1,7-diaminoheptane/methanol/urea inclusion compound showing the hydrogen bonding arrangement.

In the past, several crystal structures have been solved for this new class of urea inclusion compounds containing the following guest molecules: 1,7-diaminoheptane (1,7-DAH), 1,8-diaminooctane (1,8-DAO), 1,9-diaminononane (1,9-DAN), 1,10-diaminodecane (1,10-DAD), 1,12-diaminododecane (1,12-DADD) and 1-amino-octane. For the case of 1-amino-octane/urea/methanol, the crystal structure is somewhat different, as the tunnel segments contain two guest molecules instead of one, as in the other structures [2, 3].

Chapter 3 – Structural Properties and Solid-State Decomposition Behaviour of α,ω - Diaminoalkane/Urea Inclusion Compounds



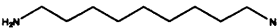


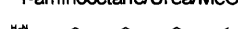
| | Space group | <i>a</i> axis (Å) | <i>b</i> axis (Å) | <i>c</i> axis (Å) | β (°) | Ratio urea/guest/methanol |
|---|-----------------|-------------------|-------------------|-------------------|-------------|---------------------------|
| 1,7-diaminoheptane/Urea/MeOH  | Monoclinic C2/c | 8.3161(10) | 13.948(2) | 29.033(3) | 95.030(5) | 7:1:2 |
| 1,8-diaminooctane/Urea/MeOH  | Monoclinic C2/c | 8.4631(9) | 13.9385(18) | 29.421(3) | 95.258(6) | 7:1:2 |
| 1,9-diaminononane/Urea/MeOH  | Monoclinic C2/c | 13.9678(7) | 8.3379(4) | 33.2409(2) | 93.681(8) | 8:1:2 |
| 1,10-diaminodecane /Urea/MeOH  | Monoclinic C2/c | 7.9408(2) | 14.6915(3) | 35.9999(6) | 90.7870(10) | 9:1:2 |
| 1,12-diaminododecane/Urea/MeOH  | Monoclinic C2/c | 13.989(3) | 8.3767(19) | 40.300(9) | 96.234(13) | 10:1:2 |
| 1-aminooctane/Urea/MeOH  | Monoclinic C2/c | 8.079(5) | 14.620(10) | 59.62(3) | 90.612(9) | 15:2:2 |

Table 3.1 Summary of known crystal structures of the different aminoalkane/methanol/urea inclusion compounds.

As seen in Table 3.1, the crystal structures for the α,ω -diaminoalkane/methanol/ urea inclusion compounds share some similarities. They are all monoclinic and belong to the same space group C2/c. The unit cell parameters also have analogies; the *a* and *b* axes have comparable values around 8.3 Å and 13.9 Å and the *c*-axis varies with the length of the guest molecule, increasing as the guest molecule becomes longer. The urea/guest/methanol ratio also changes depending on the guest molecule, so for longer guests there is a longer tunnel section and therefore more urea molecules are required to form that tunnel segment. Urea inclusion compounds containing a 1:1 mixture of α,ω -diaminoalkane and α,ω -dihydroxyalkane guest molecule have been found [4] to contain disrupted urea tunnels, similar to

α,ω -diaminoalkane/ methanol/urea, where the methanol is replaced by a short α,ω -dihydroxyalkane.

This chapter is intended to investigate the stability of the different α,ω -diaminoalkane/MeOH/urea inclusion compounds at room temperature and the possible structural transformations.

3.2 – Experimental

The materials studied here were prepared from a homogeneous solution of urea, the guest molecules (1,6-diaminohexane, 1,7-diaminoheptane, 1,8-diaminooctane, 1,9-diaminononane, 1,10-diaminodecane or 1,12-diaminododecane) and the solvent methanol [in some cases, *t*-amyl alcohol (2-methyl-2-butanol) was also added drop wise (1-2 ml) in order to obtain a homogeneous solution]. The solutions were prepared following the standard method for conventional urea inclusion compounds, in a conical flask at room temperature and then heated up to 55°C. The urea : guest ratio used was 6 : 1 (0.5 g of urea and ~0.15 g of the guests) and 3 ml of methanol were added to the solution until the urea and the guest were completely dissolved. Once a homogeneous solution was obtained at 55°C, the flasks were placed in an incubator, and the temperature was decreased slowly and gradually to

room temperature (the usual cooling rate was $-0.01\text{ }^{\circ}\text{C/min}$). In most cases, the crystals were hexagonal flat plates.

The samples obtained were characterized at Cardiff University using an optical microscope, single crystal X-ray diffraction and powder X-ray diffraction (PXRD) (See section 2.2.3 and 2.2.4 for more details on the instruments). Single crystal X-ray diffraction was used to solve the crystal structure for 1,6-diaminohexane/urea/methanol at room temperature and powder X-ray diffraction was used to study the decomposition behaviour.

3.3 – 1,6-Diaminohexane/Methanol/Urea

Previously, the shortest α,ω -diaminoalkane guest molecule studied was 1,7-DAH [1, 3]. In the present work, the family was extended by investigating the inclusion compound formed with 1,6-diaminohexane (1,6-DAHx) as the guest molecule. The crystal structure determination of 1,6-diaminohexane/methanol/urea inclusion compound (1,6-DAHx/ MeOH/Urea) was carried out from single-crystal X-ray diffraction data collected on a Nonius Kappa CCD diffractometer at ambient temperature using monochromated $\text{MoK}\alpha$ radiation ($\lambda = 0.71073\text{ \AA}$). The crystal structure was solved using SHELXS [5] and refined using SHELXL [5] ($R1 = 0.0538$,

$wR2 = 0.1331$ [$I > 2\sigma(I)$]. The crystal structure for 1,6-DAHX/ MeOH/Urea is monoclinic, with space group $P2_1/c$ and unit cell parameters $a = 13.2901(4)$ Å, $b = 7.7411(3)$ Å, $c = 15.0043(5)$ Å and $\beta = 106.1080(10)^\circ$ (Figure 3.6). (See Appendix A for extended crystallographic data).

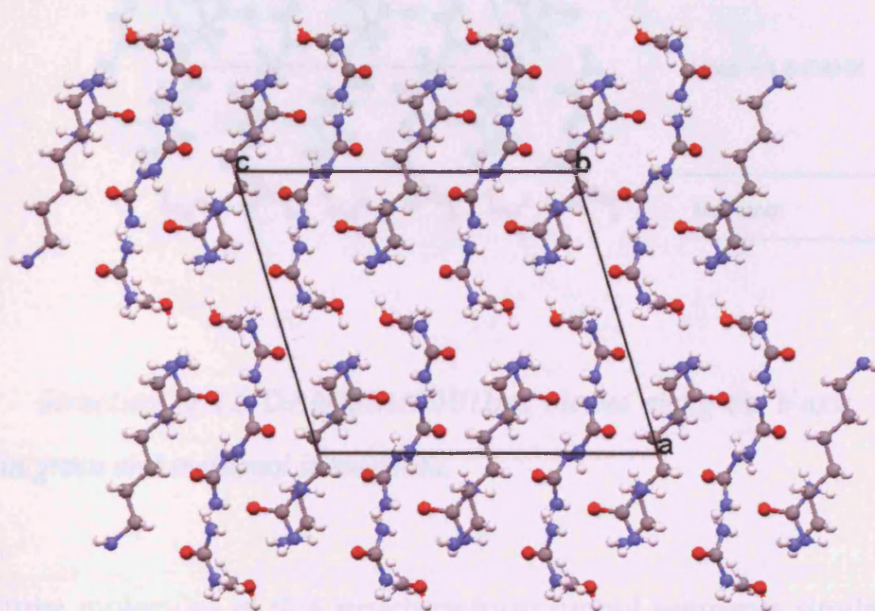


Figure 3.6 The 1,6-DAHX/MeOH/Urea inclusion compound viewed along the b -axis.

Although the space group and the unit cell parameters are different from the rest of the family members studied (Table 3.1), there is a resemblance regarding the internal unit cell arrangement. The crystal structure formed with 1,6-DAHX is also a layered UIC containing methanol molecules in between layers of urea and 1,6-DAHX molecules (Figure 3.7).

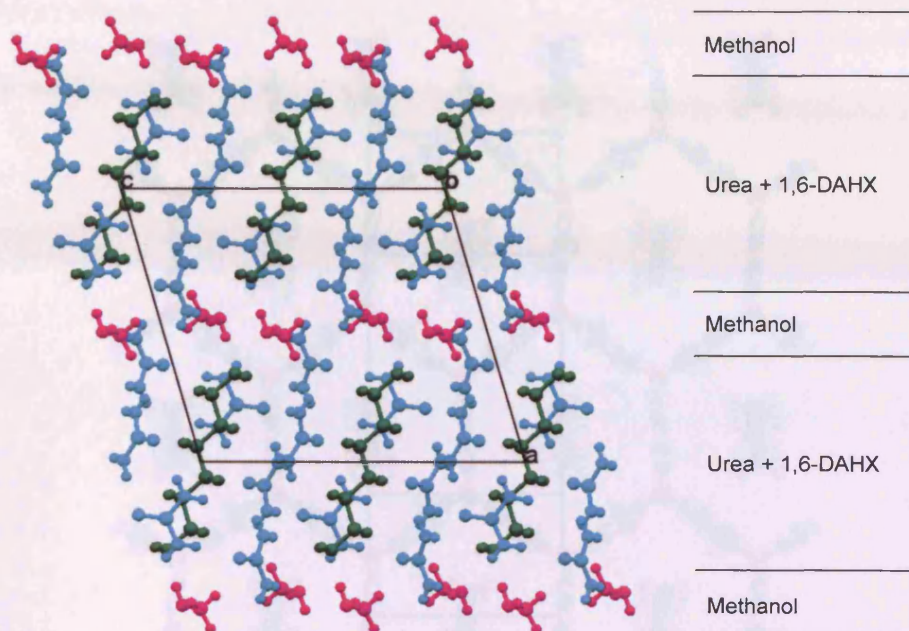


Figure 3.7 Structure of 1,6-DAHx/MeOH/Urea viewed along the *b*-axis. Urea in cyan, 1,6-DAHx in green and methanol in magenta.

The urea molecules in this structure form tunnel segments similar to those in the conventional UICs. The section of the tunnels for this particular case is a distortion of a hexagon and the direction of the tunnel segment is not parallel to any of the crystallographic axes (Figure 3.8). The tunnel segments are shorter than in the previous structures and contain one molecule of 1,6-DAHx and the urea/guest/methanol ratio is 6:1:2.

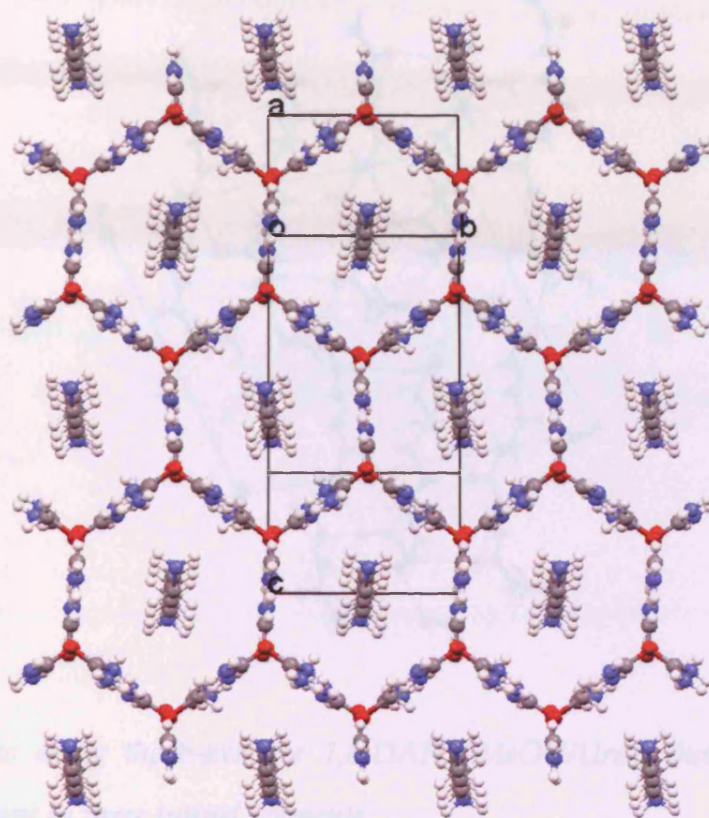


Figure 3.8 View along the tunnel segments for 1,6-DAHx/MeOH/Urea.

An important analogy with the other members of the family is the hydrogen bonding arrangement of the urea molecules within the tunnel segment, as well as the hydrogen bonding array in the interlayer regions (Figure 3.9). The methanol molecules are connected by hydrogen bonding to a 1,6-DAHx molecule in one layer and to two urea molecules in the adjacent layer.

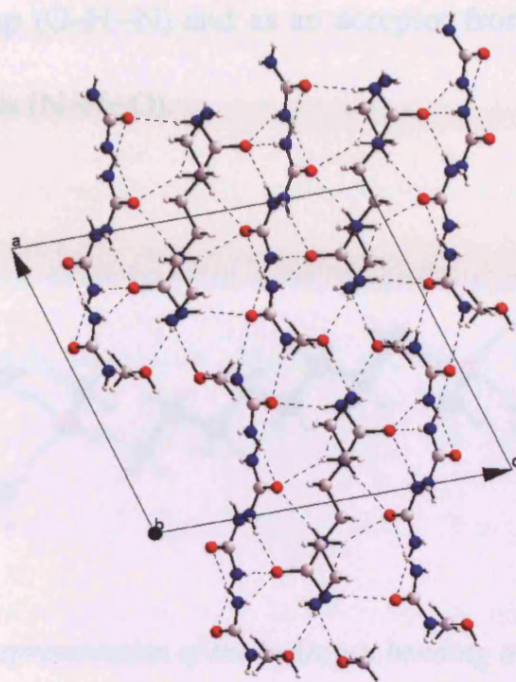


Figure 3.9 View along the *b*-axis for 1,6-DAHx/MeOH/Urea, showing the hydrogen bonding arrangement in three tunnel segments.

As seen in Figure 3.9, in the host-guest layer, the urea molecules are hydrogen bonded to each other in a comparable manner to the conventional UICs. Each oxygen atom in the urea molecule is an acceptor for N–H...O hydrogen bonds with the NH₂ groups of four different urea molecules. As a common feature in all UICs, the 1,6-DAHx molecule does not form hydrogen bonds with the urea molecules constructing the tunnel.

A detailed scheme of hydrogen bonding concerning the methanol molecules is shown in Figure 3.10. Each oxygen in the methanol acts as a donor to a nitrogen in the

1,6-DAHx amino group ($\text{O}-\text{H}\cdots\text{N}$) and as an acceptor from the NH_2 groups of two different urea molecules ($\text{N}-\text{H}\cdots\text{O}$).

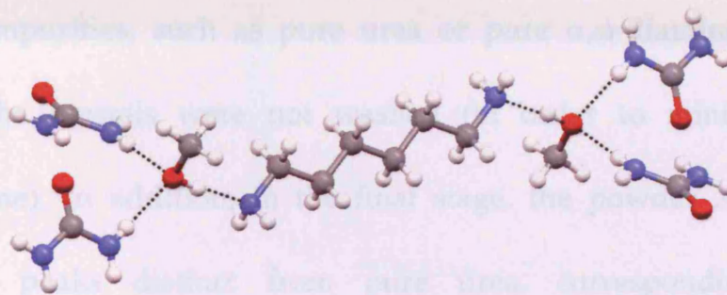


Figure 3.10 Detailed representation of the hydrogen bonding arrangement for the methanol molecules in 1,6-DAHx/MeOH/Urea.

3.4 – Decomposition Behaviour

3.4.1 – Introduction

While carrying out some preliminary powder X-ray diffraction characterization, it was found that the α,ω -diaminoalkane/methanol/urea inclusion compounds undergo a structural change over a period of time at room temperature. This section is focused on exploring the structural evolution of this process.

This decomposition is also evident from visual inspection of the crystals. Thus, the crystals, which are almost transparent in solution, become cloudy and white

shortly after they have been removed from the mother liquor. This effect can be minimized as much as possible by minimizing the time between collecting the crystals and the first data recording. In some powder X-ray patterns for the initial phase, some impurities, such as pure urea or pure α,ω -diaminoalkanes, may be observed as the crystals were not washed (in order to minimize the sample preparation time). In addition, in the final stage, the powder X-ray pattern may contain other peaks distinct from pure urea, corresponding to the pure α,ω -diaminoalkanes, since they are solid at room temperature. All the powder X-ray patterns shown in this section were recorded at room temperature with Cu $K\alpha_1$ radiation, $\lambda = 1.5406 \text{ \AA}$ (See section 2.2.4 for more details on the instrument). Time in these experiments is stated in days, with day 1 corresponding to the day of the collection of the crystals from the crystallization solution, day 2 after 24 hours, day 3 after 48 hours and so on.

3.4.2 – 1,7-Diaminoheptane/Methanol/Urea Inclusion Compound

The first material to be studied with regard to decomposition behaviour was 1,7-diaminoheptane/methanol/urea inclusion compound (1,7-DAH/MeOH/Urea). The powder X-ray pattern for this material is shown in *Figure 3.11*.

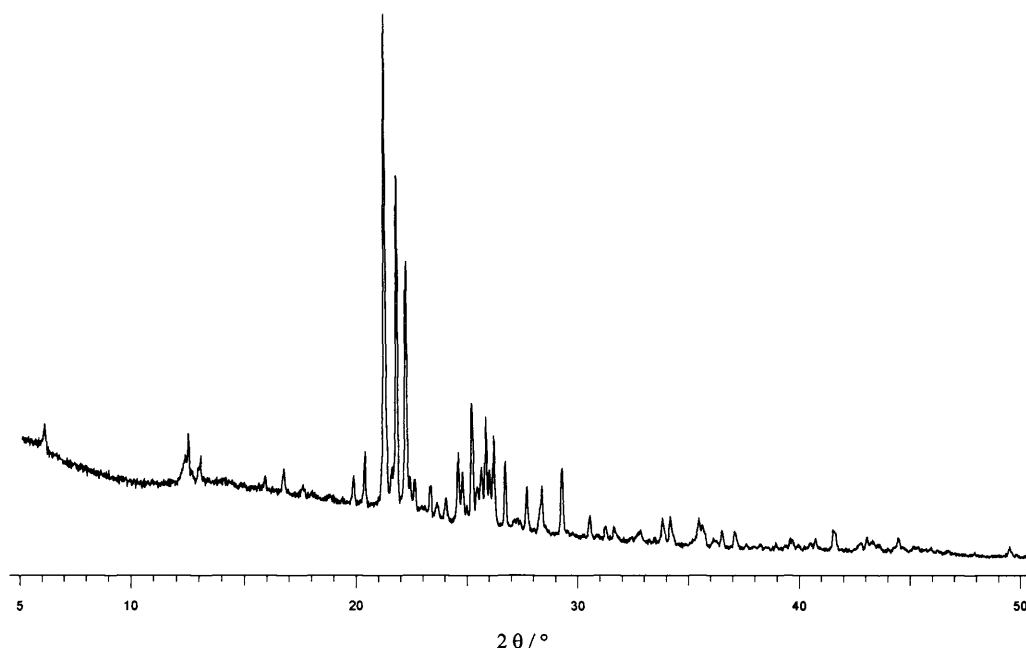


Figure 3.11 Powder X-ray diffraction pattern of the 1,7-diaminoheptane/methanol/urea inclusion compound.

The decomposition in this case occurs rapidly, and a pure phase of 1,7-DAH/MeOH/Urea was only be observed on day 1, by day 2, the sample was a mixture of the 1,7-DAH/MeOH/Urea with the conventional UIC (Figure 3.12). There was a coexistence of these two phases until day 4, when the starting phase had disappeared and pure urea (Figure 3.13) started to appear. Urea and the conventional UIC coexisted until day 15 (Figure 3.14). After that, mainly pure urea remained. Once the pure urea stage was reached, no further changes were observed as a function of time and the process was considered finished.

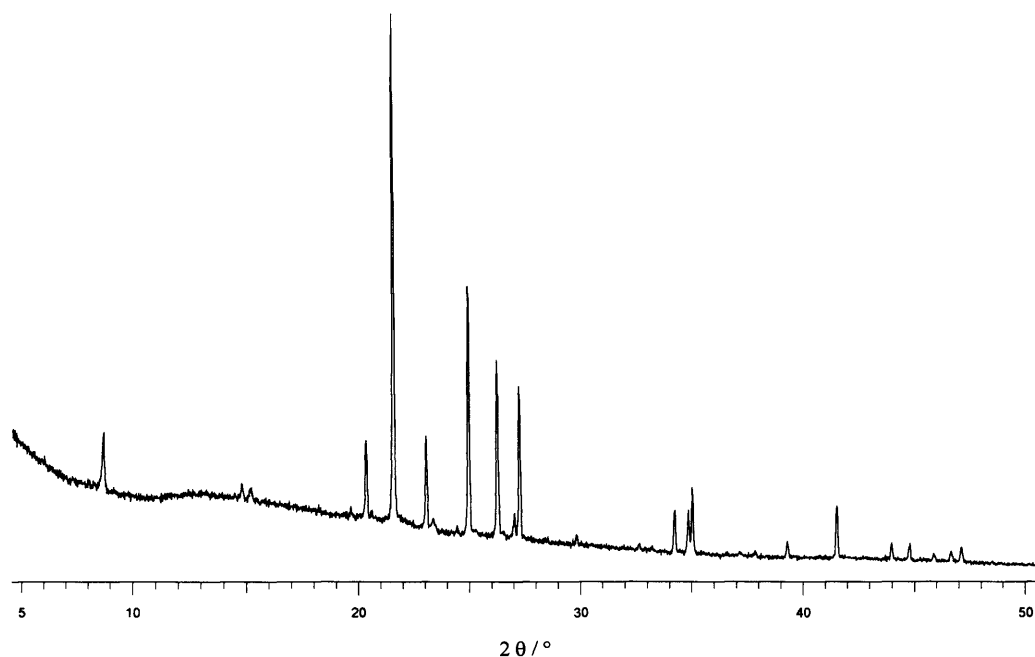


Figure 3.12 Powder X-ray diffraction for a conventional UIC, in this case the 1,10-dibromodecane/urea inclusion compound.

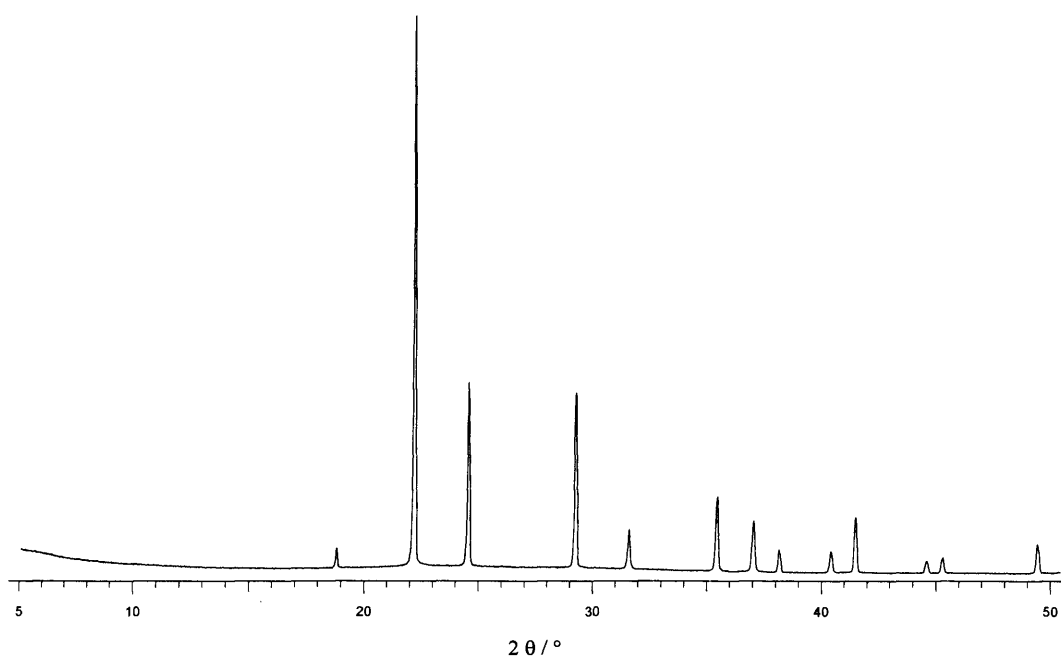


Figure 3.13 Powder X-ray diffraction pattern for pure urea.

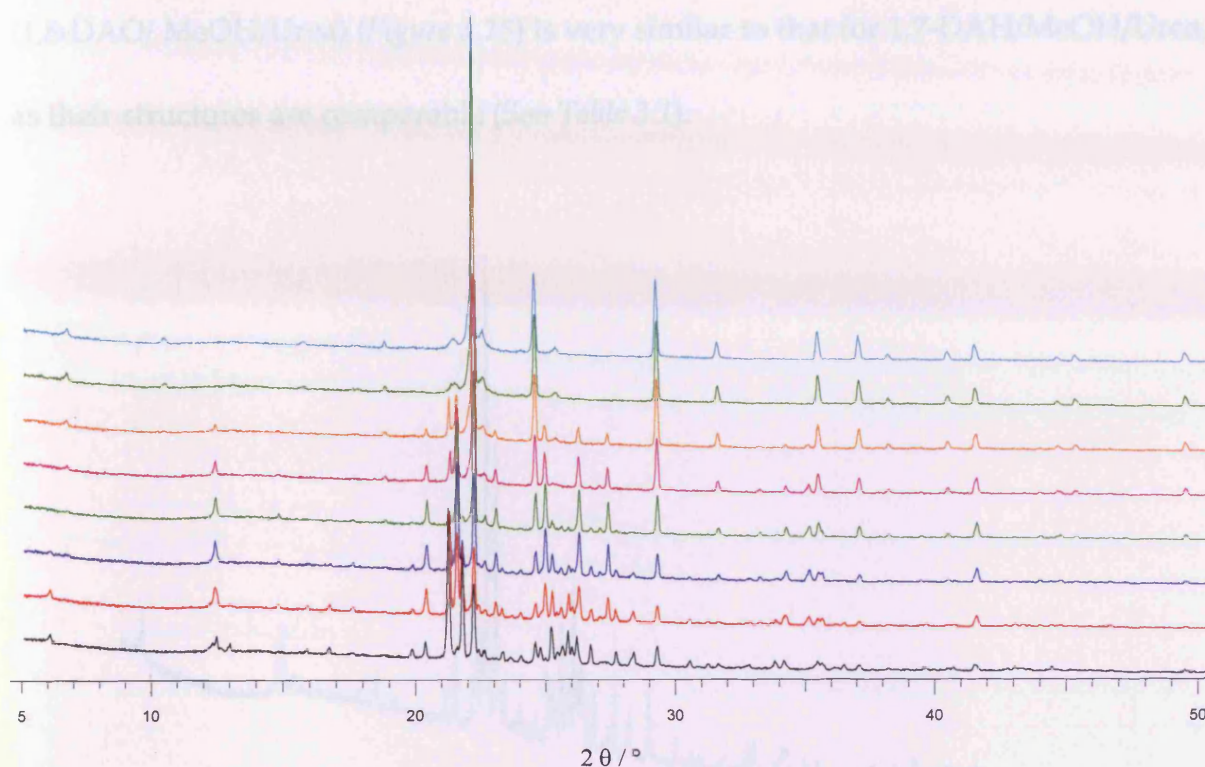


Figure 3.14 Powder X-ray diffraction patterns showing the decomposition of the 1,7-diaminoheptane/methanol/urea inclusion compound as a function of time: after day 1 (black), day 2 (red), day 3 (blue), day 4 (green), day 8 (purple), day 12 (orange), day 16 (dark green) and day 36 (cyan).

3.4.3 – 1,8-Diaminooctane/Methanol/Urea Inclusion Compound

Having detected the decomposition process with 1,7-DAH/MeOH/Urea, it was decided that the other known members of the α,ω -diaminoalkanes family should be examined as well to assess differences in the rate of decomposition behaviour. The powder pattern of the 1,8-diaminooctane/methanol/urea inclusion compound

(1,8-DAO/ MeOH/Urea) (*Figure 3.15*) is very similar to that for 1,7-DAH/MeOH/Urea, as their structures are comparable (See *Table 3.1*).

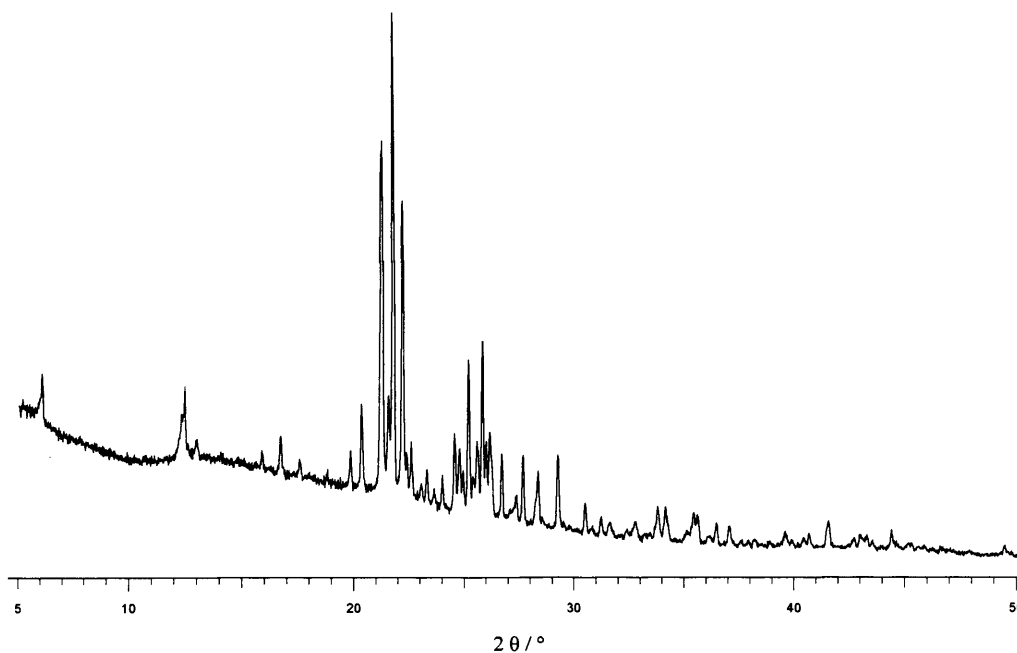


Figure 3.15 Powder X-ray diffraction pattern of the 1,8-diaminooctane/methanol/urea inclusion compound.

Although being similar in structure and exhibiting the same kind of decomposition behaviour, the process for 1,8-DAO/MeOH/Urea occurs over a longer period of time (*Figure 3.16*). Thus, the appearance of conventional UIC can be observed on day 2, the starting phase disappears on day 3, and pure urea emerges on day 7. The material is a mixture of conventional UIC and pure urea until day 65, after which predominantly pure urea remains.

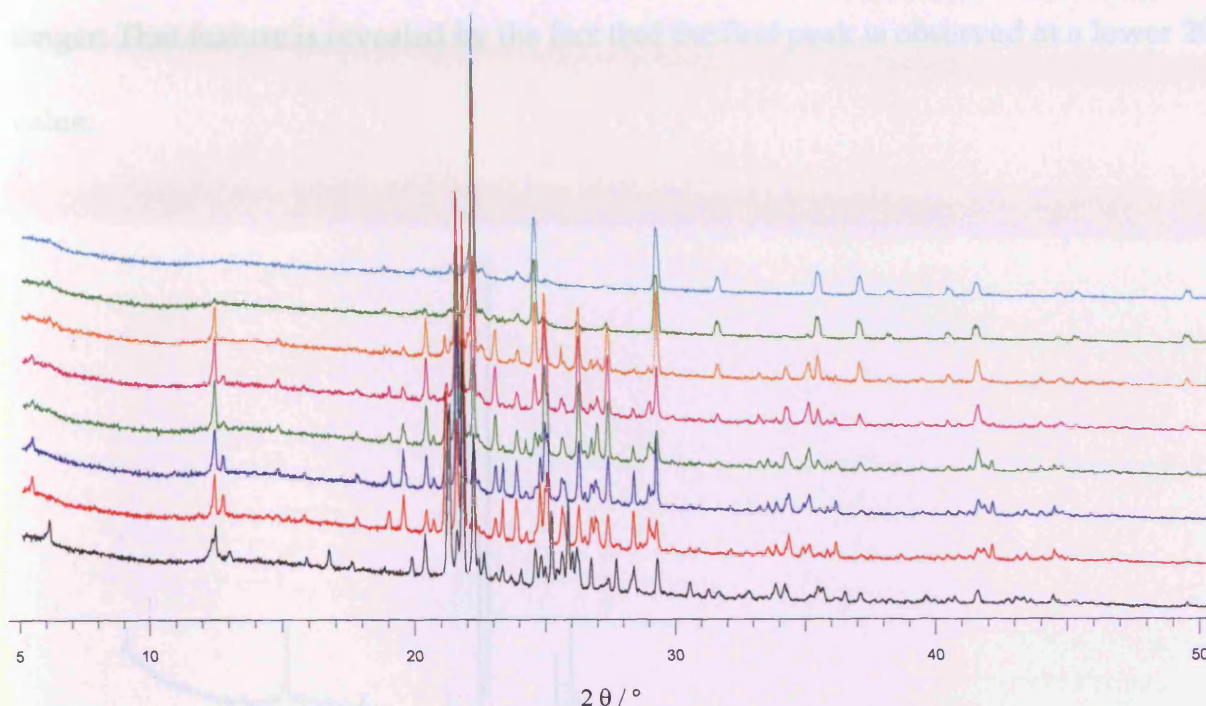


Figure 3.16 Powder X-ray diffraction patterns showing the decomposition of the 1,8-diaminooctane/methanol/urea inclusion compound as a function of time: after day 1 (black), day 2 (red), day 3 (blue), day 10 (green), day 18 (purple), day 36 (orange), day 59 (dark green) and day 72 (cyan).

3.4.4 – 1,9-Diaminononane/Methanol/Urea Inclusion Compound

The PXRD pattern for the 1,9-diaminononane/methanol/urea inclusion compound (1,9-DAN/MeOH/Urea) is shown in Figure 3.17. Although the crystal structure is still monoclinic, the urea:guest:methanol ratio is different from 1,7-DAH/MeOH/Urea and 1,8-DAO/MeOH/Urea. There are 8 urea molecules (See

Table 3.1) for each guest molecule and the c -axis of the unit cell is correspondingly longer. That feature is revealed by the fact that the first peak is observed at a lower 2θ value.

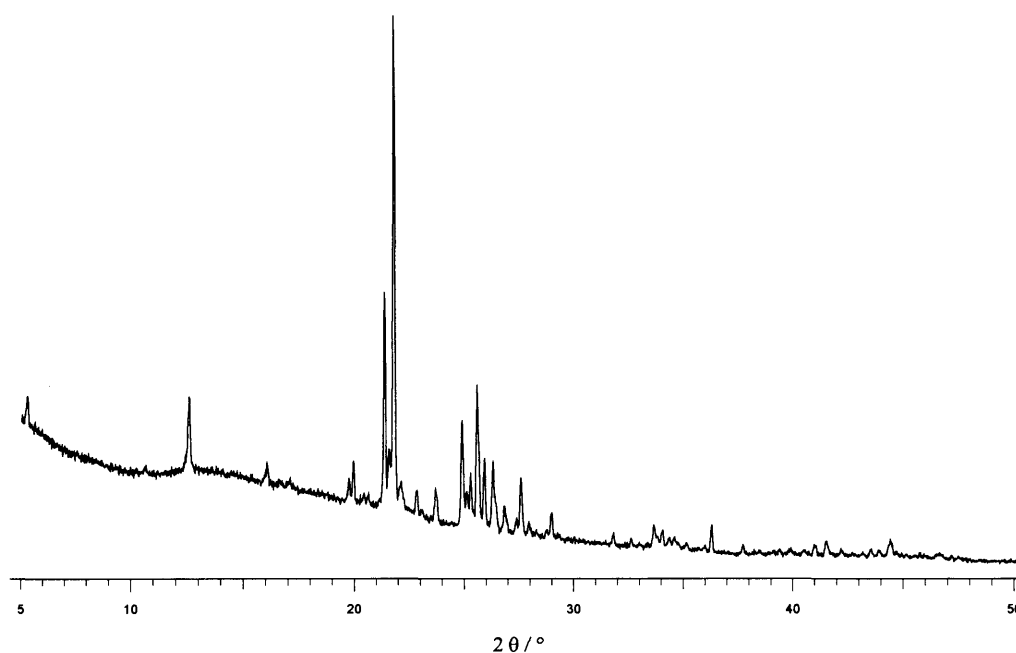


Figure 3.17 Powder X-ray diffraction pattern of the 1,9-diaminononane/methanol/urea inclusion compound.

Regarding the decomposition behaviour, there is a resemblance with the other materials discussed above, although the timescale is different. As observed in Figure 3.18, the appearance of conventional UIC occurs on day 2 and the disappearance of the starting phase (1,9-DAN/MeOH/Urea) occurs on day 3. Pure urea appears on day

12, after which it coexists with the conventional UIC. By day 118, the sample comprises principally pure urea.

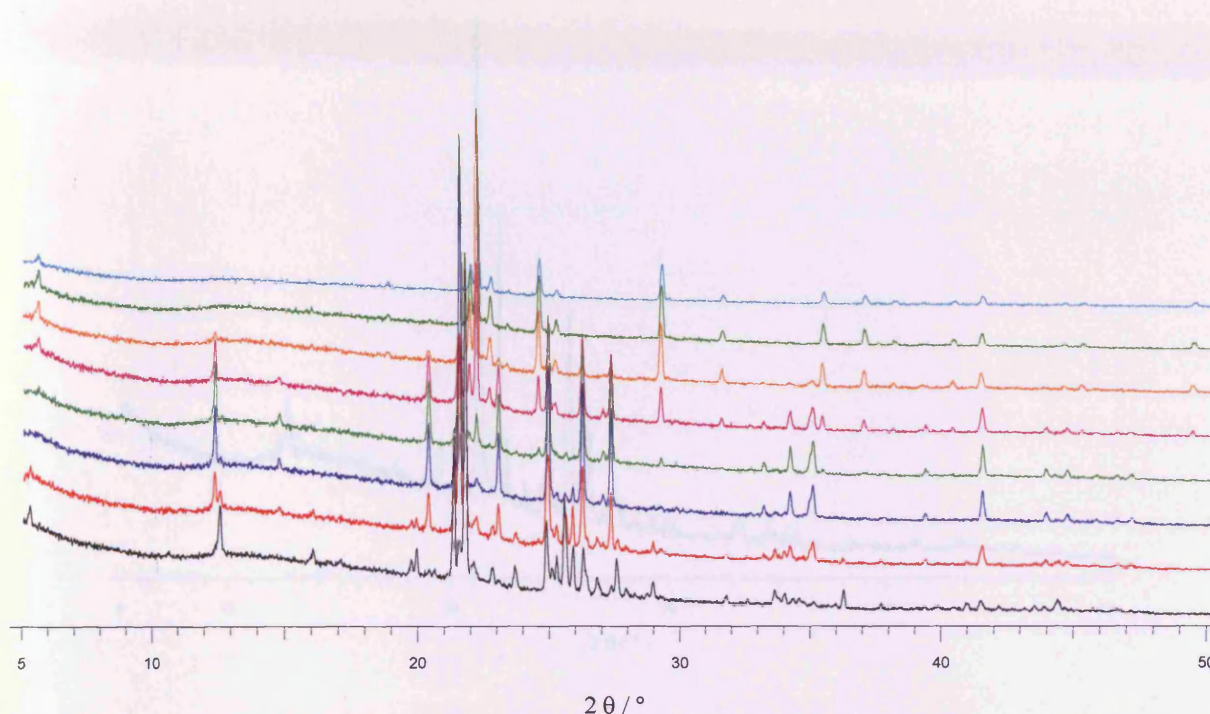


Figure 3.18 Powder X-ray diffraction patterns showing the decomposition of the 1,9-diaminononane/methanol/urea inclusion compound as a function of time: after day 1 (black), day 2 (red), day 3 (blue), day 8 (green), day 32 (purple), day 107 (orange), day 225 (dark green) and day 423 (cyan).

3.4.5 – 1,10-Diaminodecane/Methanol/Urea Inclusion Compound

After seeing that the decomposition also occurred in 1,8-DAO/MeOH/Urea and 1,9-DAN/MeOH/Urea, the experiments were extended to an additional member:

the 1,10-diaminodecane/methanol/urea inclusion compound (1,10-DAD/MeOH/Urea). The PXRD pattern for this material is shown in *Figure 3.19*.

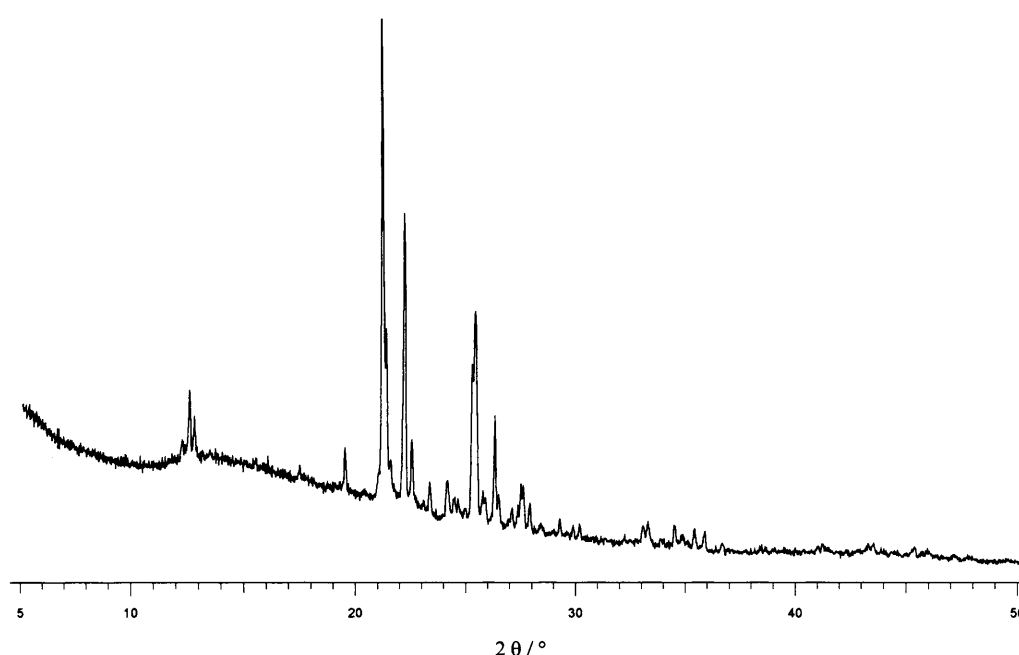


Figure 3.19 Powder X-ray diffraction pattern of the 1,10-diaminodecane/methanol/urea inclusion compound.

The decomposition for 1,10-DAD/MeOH/Urea takes place in a similar manner (*Figure 3.20*). Although being similar with the previous cases concerning the disappearance of the starting phase (day 4) and the appearance of conventional UIC (day 2), the urea appears later (day 14) and coexists for longer (120 days) with the conventional UIC until day 134, after which mainly pure urea is present. In addition,

the conventional UIC is present as a pure phase for a longer period of time than in the other cases (for a total of 10 days, between day 4 and day 14).

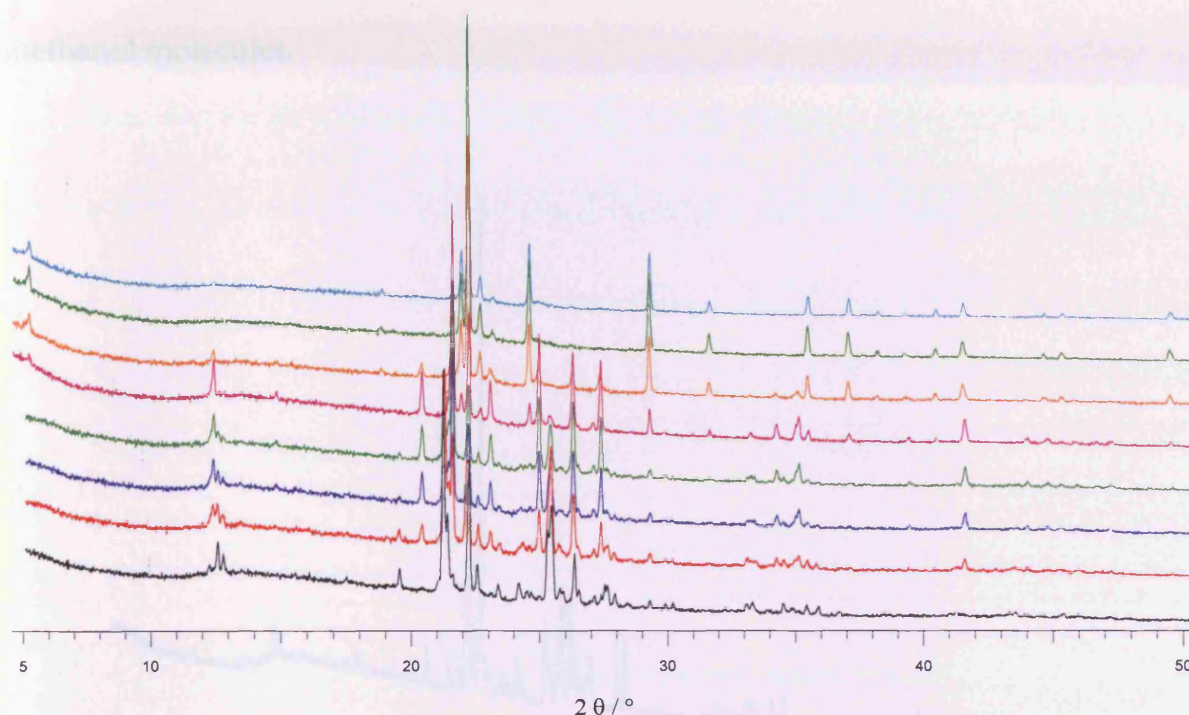


Figure 3.20 Powder X-ray diffraction pattern showing the decomposition of the 1,10-diaminododecane/methanol/urea inclusion compound as a function of time: after day 1 (black), day 2 (red), day 3 (blue), day 4 (green), day 26 (magenta), day 115 (orange), day 149 (dark green) and day 311 (cyan).

3.4.6 – 1,12-Diaminododecane/Methanol/Urea Inclusion Compound

Finally, the last material investigated was the 1,12-diaminododecane/methanol/ urea inclusion compound (1,12-DADD/MeOH/Urea) (Figure 3.21). It

contains the longest α,ω -diaminoalkane molecule examined in this family, and consequently has the longest c -axis repeat (40.300 Å). In the 1,12-DADD/MeOH/Urea structure, there are ten urea molecules per 1,12-DADD molecule and per two methanol molecules.

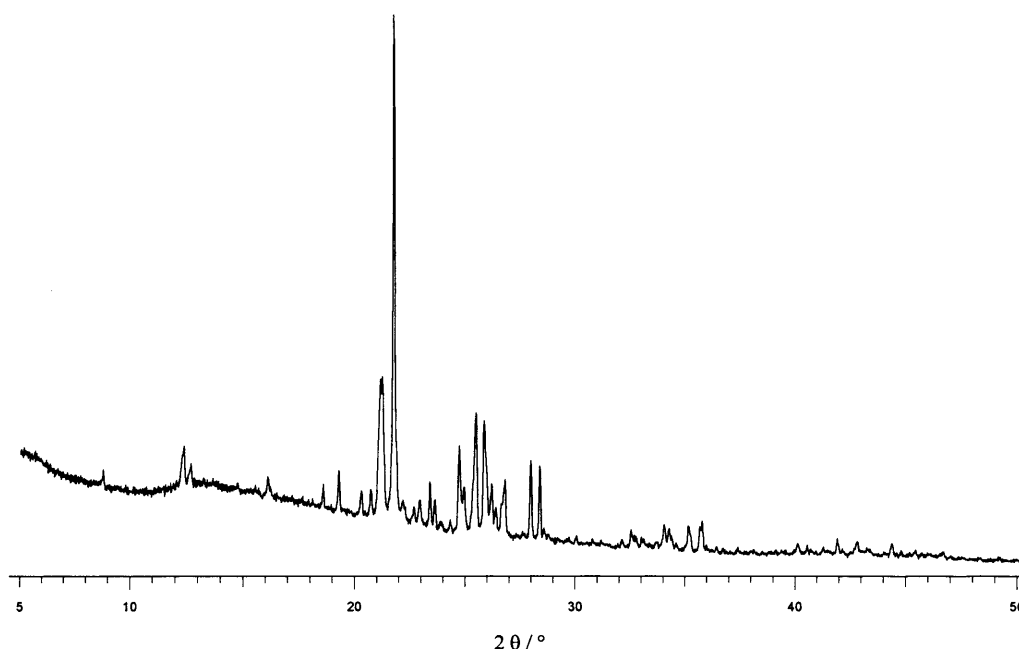


Figure 3.21 Powder X-ray diffraction pattern of the 1,12-diaminododecane/methanol/urea inclusion compound.

The decomposition analysis carried out for this compound (*Figure 3.22*) resembled the previous studies to a large extent. The conventional UIC appears near the beginning (day 2) and the starting phase disappears rapidly, on day 4, which replicates the situations observed for the other materials in this family. However, a

noticeable divergence is that on completion of the experiment (day 311), some amounts of the conventional UIC still coexisted with pure urea (which appeared on day 22).

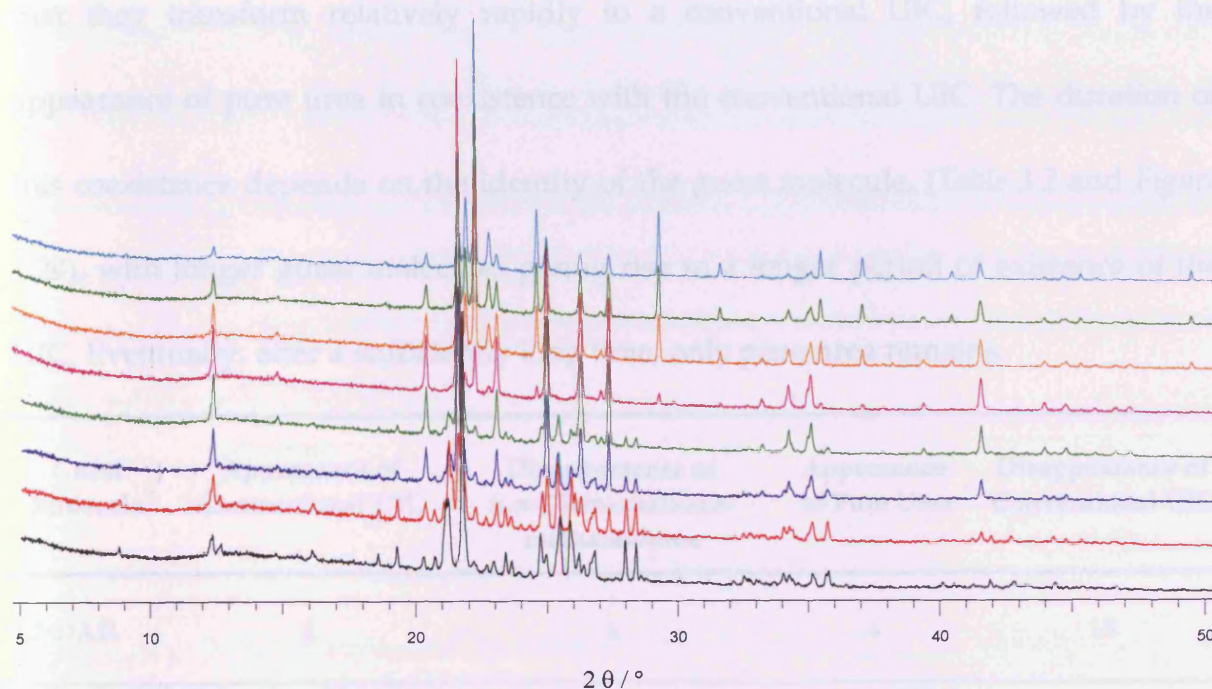


Figure 3.22 Powder X-ray diffraction patterns showing the decomposition of the 1,12-diaminododecane/methanol/urea inclusion compound as a function of time: after day 1 (black), day 2 (red), day 3 (blue), day 4 (green), day 26 (magenta), day 115 (orange), day 149 (dark green) and day 311 (cyan).

3.5 – Conclusions and Future Work

After investigating the structural evolution of the family of α,ω -diaminoalkane/methanol/urea inclusion compounds at room temperature, we can conclude that they transform relatively rapidly to a conventional UIC, followed by the appearance of pure urea in coexistence with the conventional UIC. The duration of this coexistence depends on the identity of the guest molecule, (*Table 3.2* and *Figure 3.24*), with longer guest molecules giving rise to a longer period of existence of the UIC. Eventually, after a sufficiently long time, only pure urea remains.

| Guest Molecule | Appearance of Conventional UIC | Disappearance of α,ω -Diaminoalkane/methanol/urea | Appearance of Pure Urea | Disappearance of Conventional UIC |
|----------------|--------------------------------|---|-------------------------|-----------------------------------|
| 1,7-DAH | 2 | 4 | 4 | 15 |
| 1,8-DAO | 2 | 3 | 7 | 65 |
| 1,9-DAN | 2 | 3 | 12 | 118 |
| 1,10-DAD | 2 | 4 | 14 | 134 |
| 1,12-DADD | 2 | 4 | 22 | ----- |

Table 3.2 Summary of the different members and times (in days) at which the different phases appear and disappear.

The first stage of the process seems to occur at a comparable rate regardless of the guest molecule in the structure. Thus, after 3 or 4 days, the starting phase (α,ω -diaminoalkane/methanol/urea inclusion compound) has already disappeared in all cases, and correspondingly, from day 2 the conventional UIC exists initially as a pure phase.

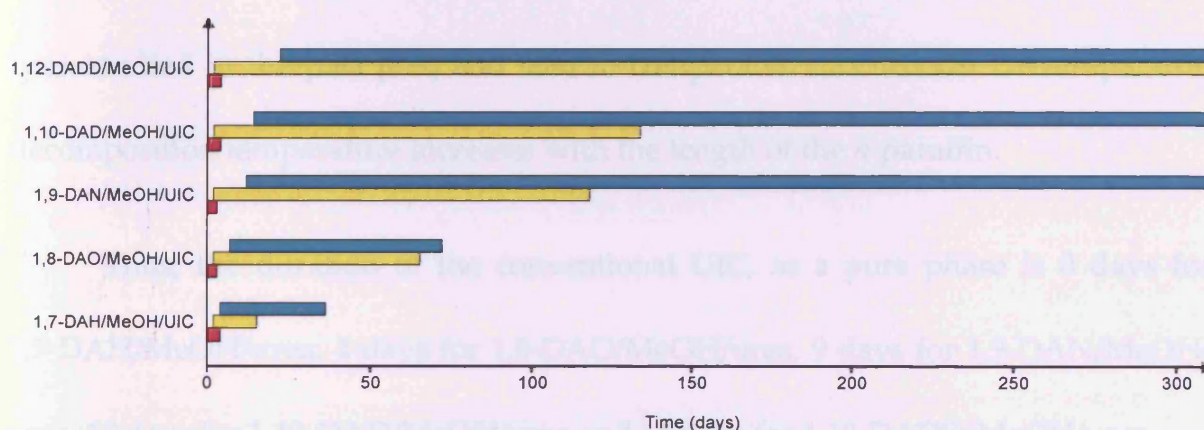


Figure 3.23 Graph showing the coexistence of the different phases for the different guest molecules. The presence of the starting material is shown in magenta, the conventional UIC in yellow and pure urea in cyan.

The fact that the formation of the conventional UIC occurs at a comparable rate irrespective of the length of the α,ω -diaminoalkane suggests that the initial stage of the process is driven by the loss of methanol from the parent structure. In each case, the conventional UIC exists as a pure phase for several days before any detectable amount of pure urea is observed. It is clear from this sequence of events

that the pure urea arises from decomposition of the conventional UIC, and does not arise from the decomposition of the α,ω -diaminoalkane/methanol/urea inclusion compound. Importantly, we find that as the α,ω -diaminoalkane becomes longer, the appearance of pure urea is observed to occur after a longer period of time, indicating that the rate of decomposition of the conventional UIC is slower as the guest molecule becomes longer. Thermal decomposition of urea inclusion compounds has been studied in the past [6-9] and lead to comparable conclusions. Urea/*n*-paraffin decomposition temperature increases with the length of the *n*-paraffin.

Thus, the duration of the conventional UIC, as a pure phase is 0 days for 1,7-DAH/MeOH/urea, 4 days for 1,8-DAO/MeOH/urea, 9 days for 1,9-DAN/MeOH/urea, 10 days for 1,10-DAD/MeOH/urea and 18 days for 1,12-DADD/MeOH/urea.

It would be extremely useful and interesting to rationalize a strategy for quantifying the relative amounts of the different coexisting phases during the decomposition process. Rietveld refinement of the PXRD patterns, have been attempted unsuccessfully thus far, possibly due to the complication of having three different phases and the overlapping of peaks between them. This information would provide understanding about the kinetics involved in the process. Moreover, extending the family to other lengths of guest molecule would be extremely revealing.

3.6 – References

- [1] S. O. Lee, B. M. Kariuki, A. L. Richardson and K. D. M. Harris, *J. Am. Chem. Soc.*, **123**, 12684-12685 (2001)
- [2] S. O. Lee, B. M. Kariuki and K. D. M. Harris, *Angew. Chem.-Int. Edit.*, **41**, 2181-2184 (2002)
- [3] S. O. Lee, A. Morte-Ródenas, B. M. Kariuki and K. D. M. Harris, *In preparation*, A family of layered inclusion compounds of urea and α,ω -diaminoalkanes
- [4] S. O. Lee, B. M. Kariuki and K. D. M. Harris, *New J. Chem.*, **29**, 1266-1271 (2005)
- [5] G. M. Sheldrick, *Acta Cryst. A*, **64**, 112-122 (2008)
- [6] K. D. M. Harris, *J. Phys. Chem. Solids*, **53**, 529-537 (1992)
- [7] H. G. McAdie, *Can. J. Chem.*, **36**, 635-651 (1958)
- [8] H. G. McAdie, *Can. J. Chem.*, **40**, 2195-2203 (1962)
- [9] H. G. McAdie, *Can. J. Chem.*, **41**, 2144-2153 (1963)

Chapter 4

X-ray Dichroism and X-ray Birefringence in Thiourea Inclusion Compounds

4.1 – Introduction

One of the recently explored applications of urea and thiourea inclusion compounds (TICs) is their potential to be used as X-ray dichroic filters [1-3]. This chapter is aimed at achieving further understanding of the correlation between the X-ray dichroism and X-ray birefringence measured on single crystals of molecular solids and the distribution of certain chemical bonds within the crystal, focusing in particular on birefringence studies to evaluate changes in molecular orientations at

order-disorder phase transitions. We emphasize that these are the first reported studies of X-ray birefringence carried out on any organic material.

Dichroic filters are materials that have different absorption coefficients for plane polarized radiation for different orientations of the material (*Figure 4.1*). The famous Polaroid filters [4] and Nicol's prisms [Iceland Spar polarizer (calcite) invented by W. Nicol in 1829] are well known examples of materials that produce plane-polarized light by only letting through the light that has a component with the electric vector vibrating in a plane parallel to the polarization plane.

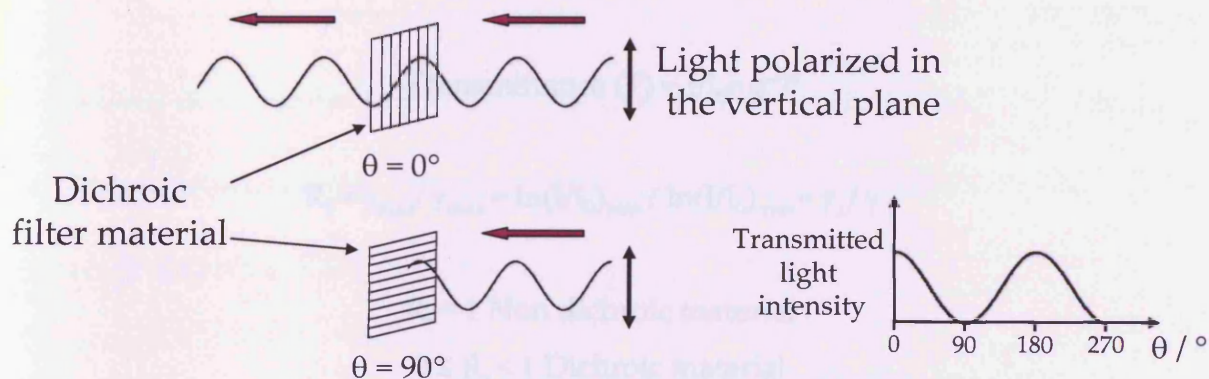


Figure 4.1 Schematic representation of the performance of a dichroic filter with different orientations. On the right the transmitted light intensity as a function of the orientation. Note that the maxima are 180° apart.

Transmittance (below) is defined as the fraction of incident radiation that passes through a sample and is the ratio between I , the transmitted intensity, and I_0 , the intensity of the incident radiation. The transmittance depends on the thickness of the crystal (t) and on the linear absorption coefficient (γ). To simplify the calculations, we assume that thickness of the crystal is the same regardless the orientation. R_γ , the ratio between the minimum and maximum values of γ , is 1 when the material is non dichroic (same γ in all orientations) and is in the range $0 \leq R_\gamma < 1$ when the material is dichroic. The lower the value of R_γ , the greater the dichroism exhibited by the material. We note that the values of γ and hence R_γ are dependent on the wavelength (λ) of the radiation.

$$\text{Transmittance (T)} = I/I_0 = e^{-\gamma t}$$

$$R_\gamma = \gamma_{\min} / \gamma_{\max} = \ln(I/I_0)_{\min} / \ln(I/I_0)_{\max} = \gamma_{\perp} / \gamma_{\parallel}$$

$$R_\gamma = 1 \text{ Non dichroic material}$$

$$0 \leq R_\gamma < 1 \text{ Dichroic material}$$

It is well known that materials that exhibit dichroism also show birefringence. Birefringence is the difference between the maximum and minimum refractive indices in an anisotropic material (*Figure 4.2*). Isotropic materials only have one refractive index (physical properties are equally propagated in all possible directions) and therefore isotropic materials are neither birefringent nor dichroic. The

maximum birefringence occurs when the “optical axis” is oriented at 45° from the orientation of γ_{\max} OR γ_{\min} .

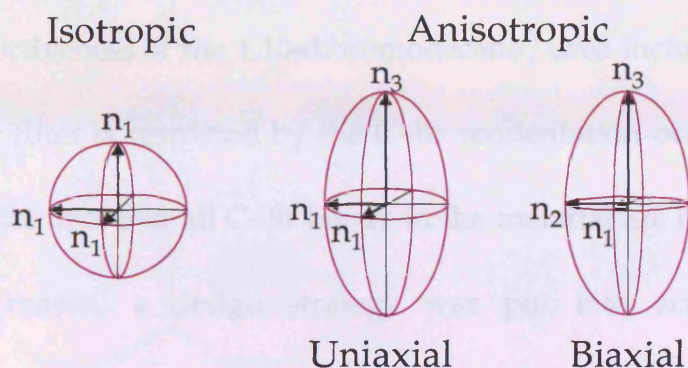


Figure 4.2 Representation of refractive indices for isotropic materials and anisotropic materials (uniaxial and biaxial).

In the present work, the anisotropy arises from the anisotropy of C–Br bond orientations of the guest molecules in thiourea inclusion compounds. The molecular anisotropy detected with X-rays is analogous to the anisotropy of the optical properties observed in the case of visible light.

X-ray dichroism data has been reported in the past [1-3] for two different solid inclusion compounds: the 1,10-dibromodecane / urea inclusion compound and the 1-bromoadamantane/thiourea inclusion compound (Figure 4.3). The first studies [1] focused on the 1,10-dibromodecane / urea inclusion compound, and demonstrated that this material behaves as an X-ray dichroic filter at X-ray energies close to the bromine K-edge, (13.474 keV). The material exhibits significant dichroism, with an R_γ

value of 0.65, representing a successful X-ray dichroic filter material. Indeed, this material was utilized in an application as an X-ray dichroic filter, specifically in polarization analysis of magnetic X-ray scattering from antiferromagnetic holmium. However, the effectiveness of the 1,10-dibromodecane / urea inclusion compound as an X-ray dichroic filter is restricted by the C–Br reorientation occurring at ambient temperature and the fact that all C–Br bonds in the material are not parallel to each other. For that reason, a design strategy was put into action [2], and the 1-bromoadamantane/thiourea inclusion compound (*Figure 4.3*) was proposed as a material in which the C–Br bonds of all guest molecules would be parallel to each other. Even though the guest molecules are disordered in two orientations, all the C–Br bonds are parallel to the tunnel and therefore the performance as an X-ray dichroic filter is unaffected by the disorder. The maximum dichroism is found between the parallel and perpendicular orientations of the tunnel and gives an improved R_{γ} value of 0.32 (compared to 0.65 for the 1,10-dibromodecane / urea inclusion compound). The experimentally observed value of $R_{\gamma} = 0.32$ is in exact agreement with the theoretically predicted optimal value [1] for a material in which all C–Br bonds are parallel to each other.

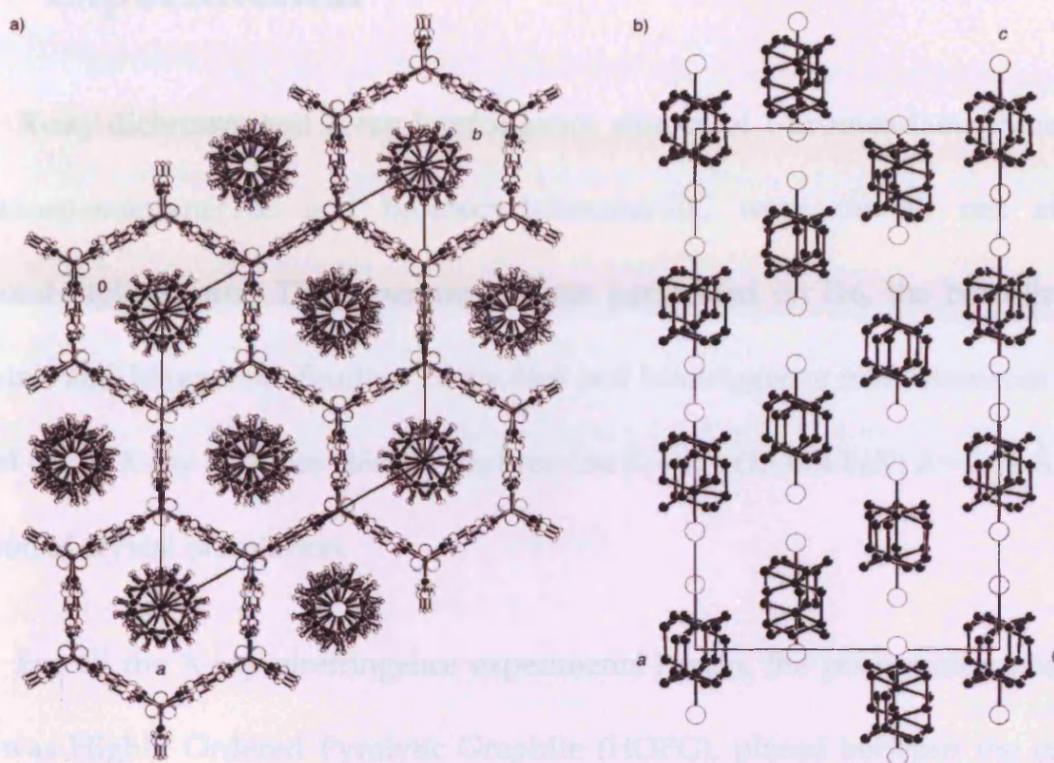


Figure 4.3 Structure of 1-bromoadamantane/thiourea inclusion compound. a) view along the *c*-axis, showing the host (thiourea) hexagonal tunnels and the included guest (1-bromoadamantane), and b) view along the *a*-axis (with thiourea molecules omitted for clarity).[2]

Following these investigations, this chapter is focused on further research carried out on the 1-bromoadamantane/thiourea inclusion compound, evaluating the performance as an X-ray dichroic filter of 2-bromoadamantane/thiourea inclusion compound and pioneering X-ray birefringence studies on the bromocyclohexane/thiourea inclusion compound, particularly concerning order-disorder phase transitions in this material.

4.2 – Experimental

X-ray dichroism and X-ray birefringence studies of 1-bromoadamantane/TIC, 2-bromoadamantane/TIC and bromocyclohexane/TIC were carried out at the Diamond Light Source. The experiments were performed on I16, the beamline for Materials and Magnetism Studies. Dichroism and birefringence measurements were carried out at X-ray energies close to the bromine K-edge (13.474 keV; $\lambda = 0.92 \text{ \AA}$) as a function of crystal orientation.

For all the X-ray birefringence experiments herein, the polarization analyser used was Highly Ordered Pyrolytic Graphite (HOPG), placed between the crystal and the detector and oriented at 90° to the polarization plane of the incident X-rays (synchrotron radiation is 95% linearly polarized in the horizontal plane), creating a ‘cross polarizer’ geometry. In this ‘cross polarizer’ setting, a lack of transmittance is indicative of isotropy, which would be interpreted for these materials as isotropic disorder of the C–Br bonds.

Beamline I16 is equipped with a six-circle kappa diffractometer [5], which allows the rotation of the sample through different angles to reach the optimal position for the relevant measurements. A low temperature stage (Oxford Cryostream) was utilized for selected experiments, cooling the sample down to 80 K. A schematic representation of the experimental set up and definitions of relevant

angles are shown in *Figure 4.4* and in *Figure 4.5*, and the actual experimental set up is shown in *Figure 4.6*.

Good quality single crystals of the TICs of interest were glued to a glass or metal fibre. Maximum care was taken while mounting the crystal to ensure that the needle axis of the crystal (the tunnel axis) was parallel to the fibre. The alignment was further optimized *a posteriori* with additional adjustments in the goniometer head.

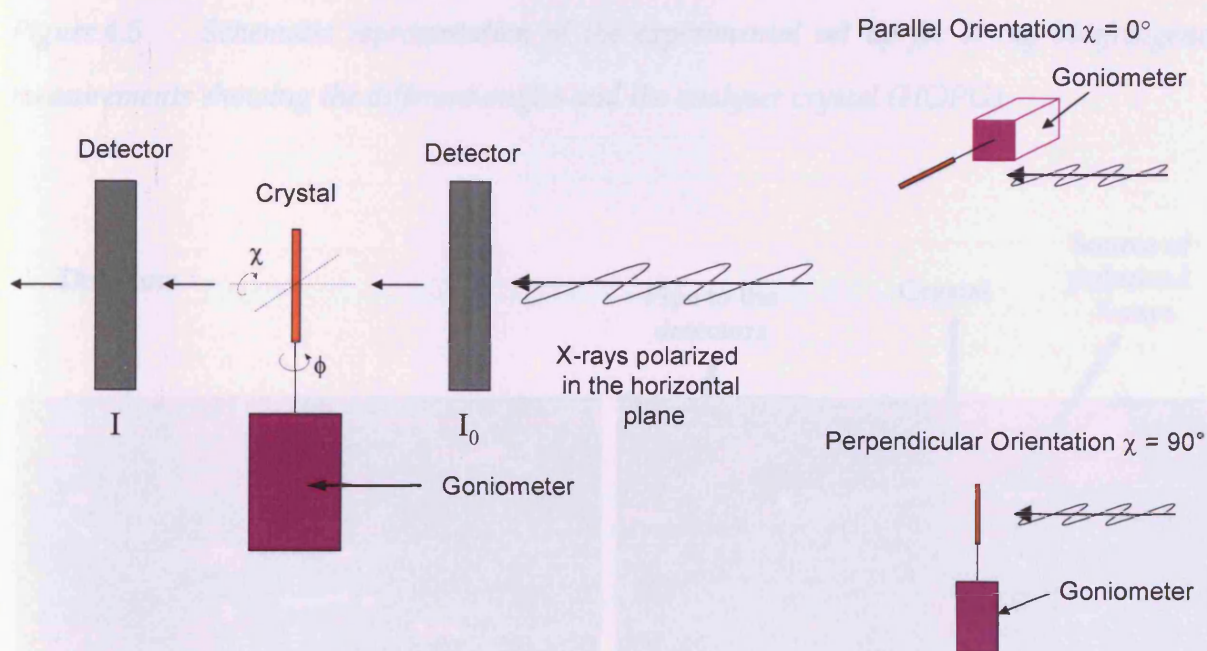


Figure 4.4 Schematic representation of the experimental set up for X-ray dichroism measurements showing the different angles and sample orientations.

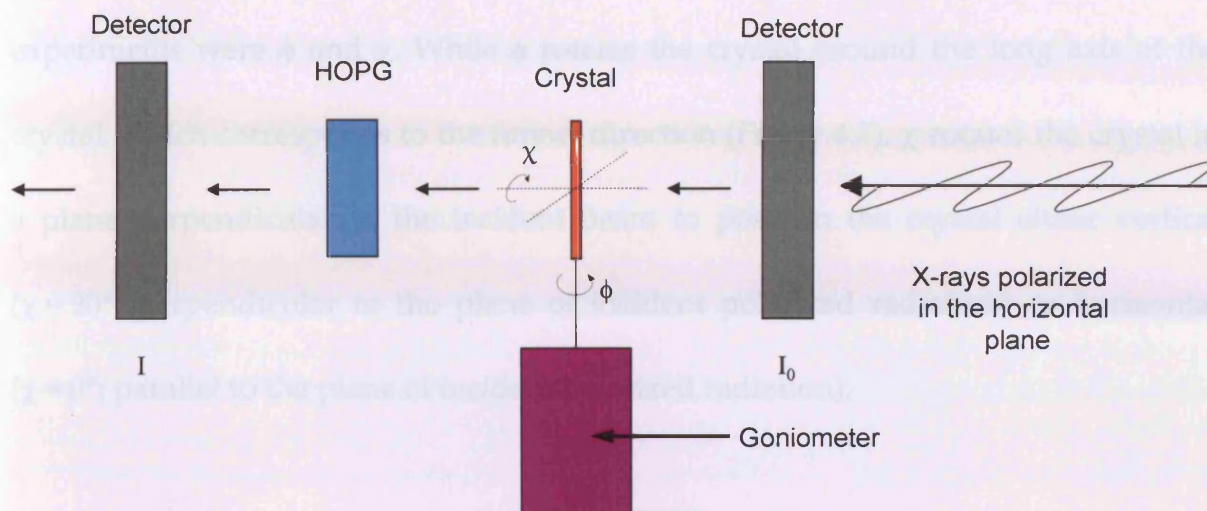


Figure 4.5 Schematic representation of the experimental set up for X-ray birefringence measurements showing the different angles and the analyser crystal (HOPG).

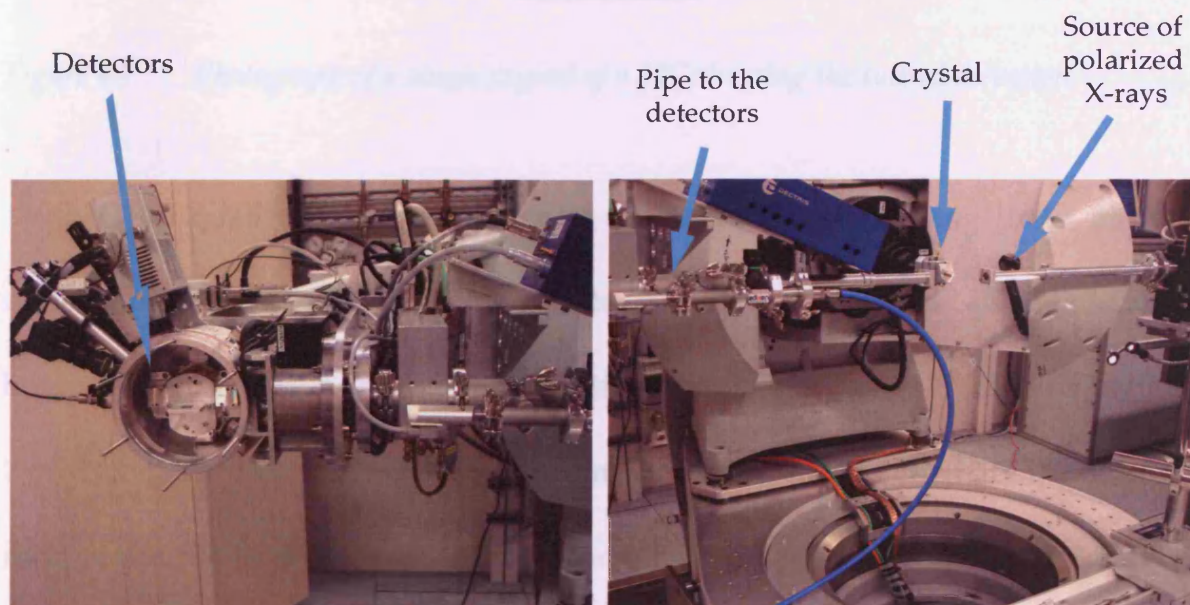


Figure 4.6 Experimental set up in beamline I16.

As seen in *Figure 4.4* and *Figure 4.5*, the two main angles varied during the experiments were ϕ and χ . While ϕ rotates the crystal around the long axis of the crystal, which corresponds to the tunnel direction (*Figure 4.7*), χ rotates the crystal in a plane perpendicular to the incident beam to position the crystal either vertical ($\chi = 90^\circ$; perpendicular to the plane of incident polarized radiation) or horizontal ($\chi = 0^\circ$; parallel to the plane of incident polarized radiation).



Figure 4.7 Photograph of a single crystal of a TIC showing the tunnel direction.

Good quality single crystals were grown by slowly cooling [from 55 °C to room temperature with a cooling rate of -0.01 °C/min in an incubator] a homogeneous solution of the commercially obtained guest (1-bromoadamantane, 2-bromoadamantane or bromocyclohexane) and thiourea in methanol. The molar ratio of the thiourea to guest in these inclusion compounds is typically 3:1 or 4:1. However, when preparing the crystallization solution, the guest was added in excess. Large (a range of sizes up to 1 mm × 1 mm × 1 cm), hexagonal, needle-morphology crystals were obtained (*Figure 4.7*).

Crystal structure determination of 2-bromoadamantane/TIC and bromocyclohexane/TIC was carried out from single-crystal X-ray diffraction data collected at Cardiff University on a Nonius Kappa CCD diffractometer at 110 K using monochromated MoK α radiation ($\lambda = 0.71073$ Å). The crystal structures were solved (using SHELXS [6]) and refined (using SHELXL [6]) by Dr Benson Kariuki. Powder X-ray diffraction data for bromocyclohexane/TIC were recorded on station 9.1 at the synchrotron facilities at Daresbury SRS, with $\lambda = 0.9992$ Å. The sample was packed in a 0.5 mm capillary and an Oxford cryostream system was used to cool the sample to 80 K. Differential Scanning Calorimetry (DSC) data were recorded using a Q100 TA Instruments with a cooling rate of 10 °C/min.

4.3 – 1-Bromoadamantane / Thiourea Inclusion Compound

As described in section 4.1, the 1-bromoadamantane/thiourea inclusion compound (1-BA/TIC) exhibits strong X-ray dichroism close to the bromine K-edge ($R_{\gamma} = 0.32$ at 13.479 keV) [2]. In this section, 1-BA/TIC is utilized as the prototype to investigate X-ray birefringence, as this compound was specifically designed and demonstrated to exhibit maximum dichroism. 1-BA/TIC is a well-behaved system in terms of the C–Br bond orientations with respect to the tunnel direction (all C–Br

bonds are parallel to the tunnel direction) and does not undergo any phase transitions at low temperature.

X-ray birefringence measurements for 1-BA/TIC are in agreement with the previous X-ray dichroism results [2]. *Figure 4.8* shows the X-ray transmittance as a function of energy. As expected for 1-BA/TIC, the maximum birefringence is found when the tunnel axis of the crystal is orientated at $\chi = 45^\circ$ (*Figure 4.9a*), which is mid-way between the orientations corresponding to minimum $\chi = 90^\circ$, and maximum $\chi = 0^\circ$ transmittance. In this case, minima in birefringence are observed at $\chi = 0^\circ$ and $\chi = 90^\circ$.

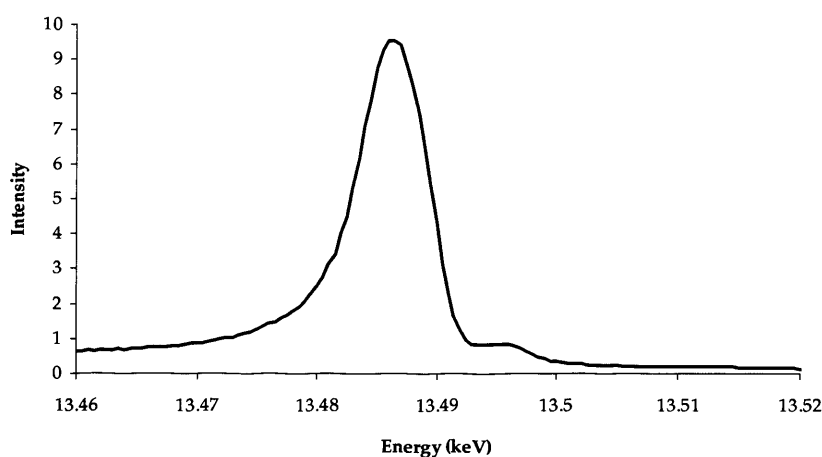


Figure 4.8 X-ray birefringence measurement for 1-BA/TIC at $\chi = 45^\circ$.

In theory, for a perfect single crystal of 1-BA/TIC, no dependence on the angle ϕ is expected as the orientation of the C–Br bonds is invariant to rotation of ϕ . In the measurement shown in *Figure 4.9b*, a small dependence on ϕ is observed because of

the combination of two factors: i) the thickness of the crystal varies slightly with ϕ (in principle, only a crystal of cylindrical shape would have a constant thickness as a function of ϕ) and ii) the alignment of the crystal may not be perfect. Both of these explanations are compatible with the observation that the results in *Figure 4.9b* are symmetric on rotation of the crystal by 180° about ϕ .

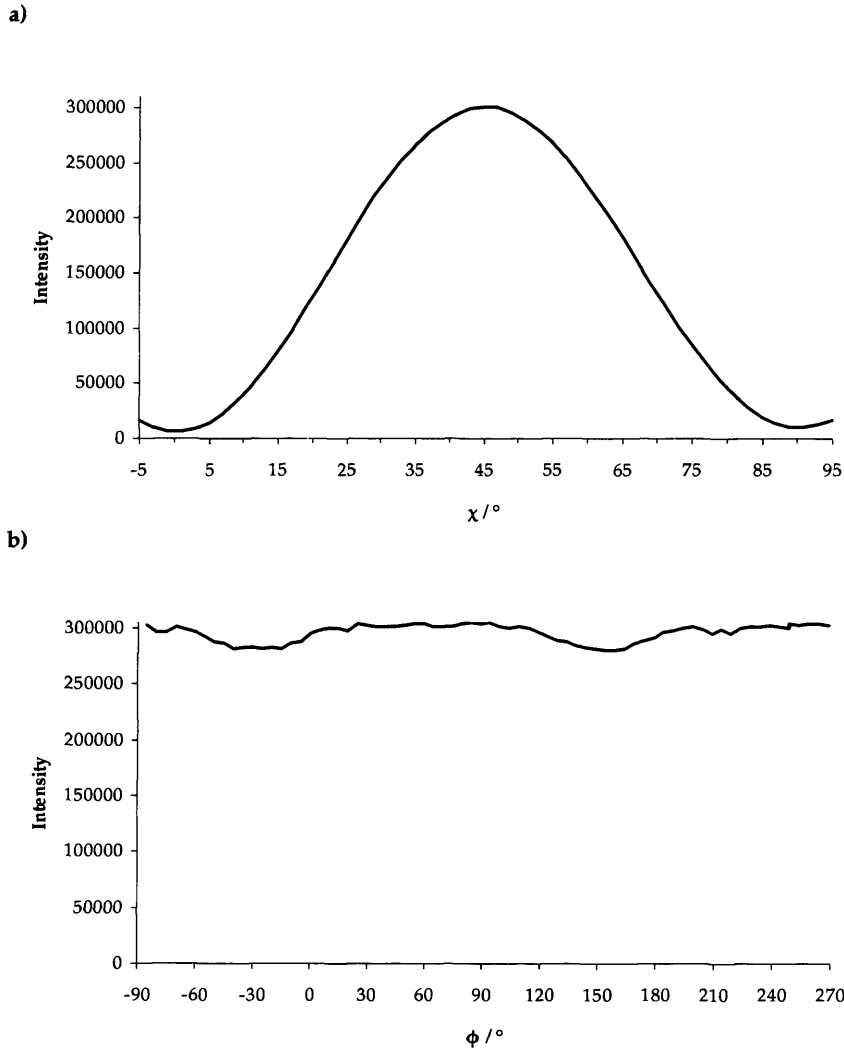


Figure 4.9 The dependence of X-ray birefringence on (a) χ and on (b) ϕ at fixed X-ray energy (13.485 keV).

4.4 – 2-Bromoadamantane / Thiourea Inclusion Compound

More exhaustive research was carried out on the 2-bromoadamantane/thiourea inclusion compound (2-BA/TIC) including determination of the crystal structure from single crystal X-ray diffraction, as well as X-ray dichroism and X-ray birefringence measurements.

The crystal structure, determined at 110 K, is trigonal with space group $R\bar{3}c$ and unit cell parameters: $a = b = 16.1180(2)$ Å, $c = 61.6020(4)$ Å ($R1 = 0.1405$ and $wR2 = 0.3493$ [$I > 2\sigma(I)$]) (See Appendix B for extended crystallographic data). Although the guest molecules (2-BA) exhibit orientational disorder inside the tunnel, the C–Br bonds in all the disorder components have roughly the same orientation and are almost parallel to the thiourea tunnel direction (*Figure 4.10* and *Figure 4.11*), suggesting that this material should show good performance as an X-ray dichroic filter material.

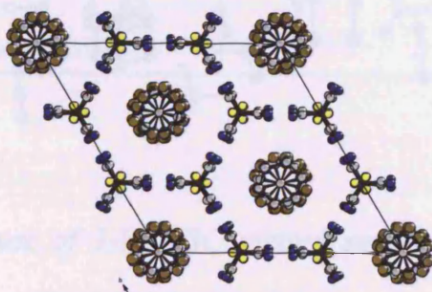


Figure 4.10 Crystal structure of 2-BA/TIC viewed along the c -axis (the tunnel direction).

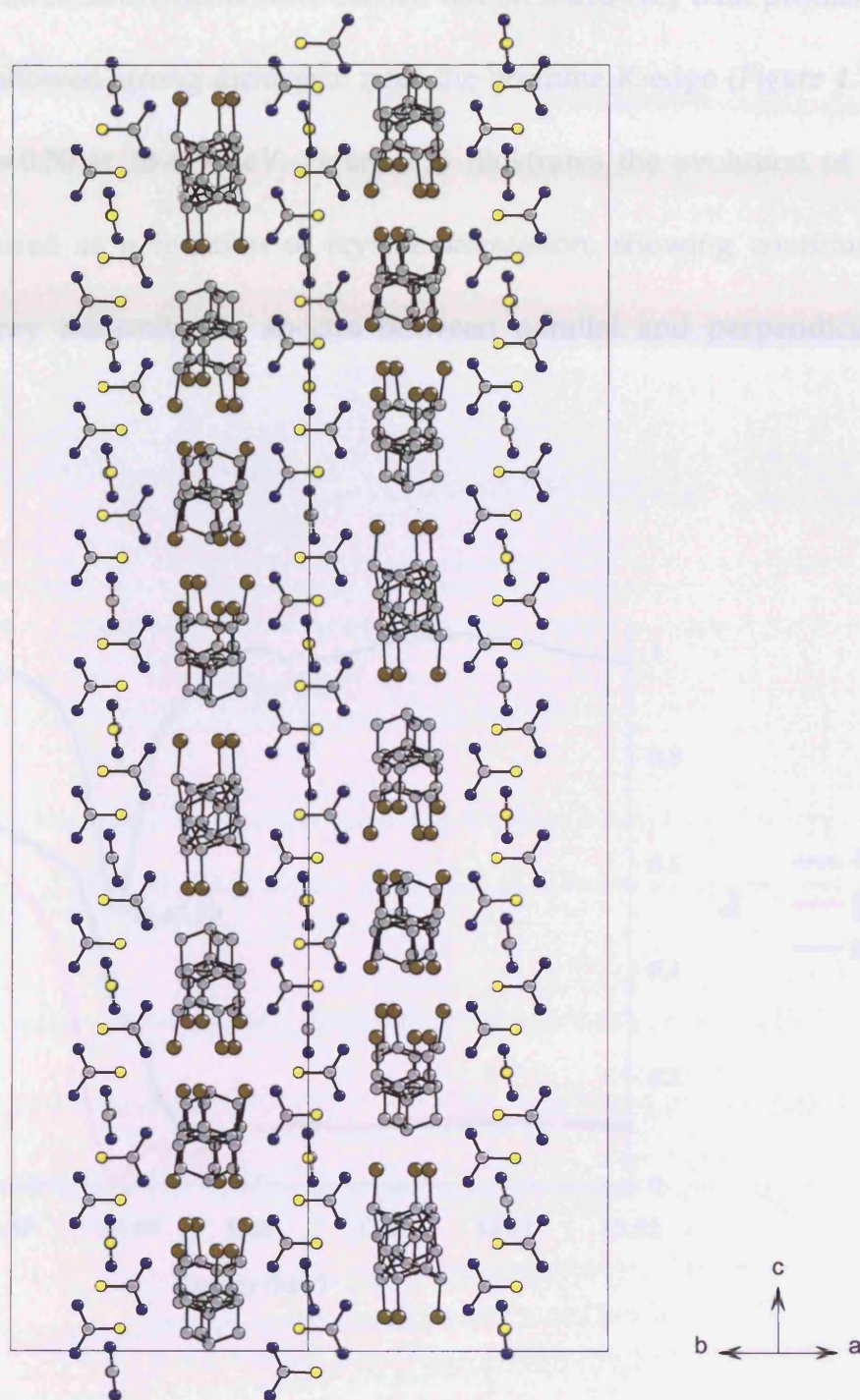


Figure 4.11 Crystal structure of 2-BA/TIC viewed perpendicular to the tunnels. Some thiourea molecules have been omitted for clarity of the guest molecule distribution inside the tunnel.

X-ray dichroism measurements were carried out on 2-BA/TIC, with promising results. The crystal showed strong dichroism near the bromine K-edge (Figure 4.12), achieving a low $R_\gamma = 0.50$ at 13.479 keV. Figure 4.13 illustrates the evolution of the transmittance measured as a function of crystal orientation, showing continuous variation in the X-ray transmittance spectra between parallel and perpendicular orientations.

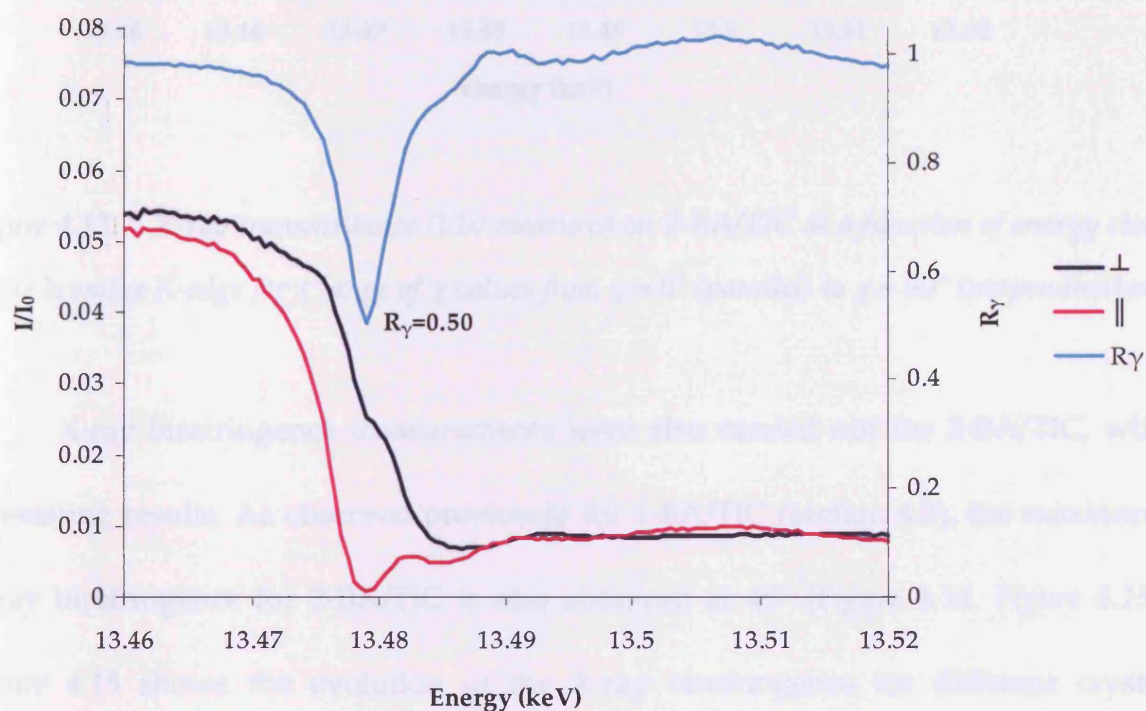


Figure 4.12 X-ray transmittance (I/I_0) measured on 2-BA/TIC as a function of energy close to the bromine K-edge for the two orientations \perp (C–Br bonds perpendicular to the incident X-ray polarization plane) and \parallel (C–Br bonds parallel to the incident X-ray polarization plane).

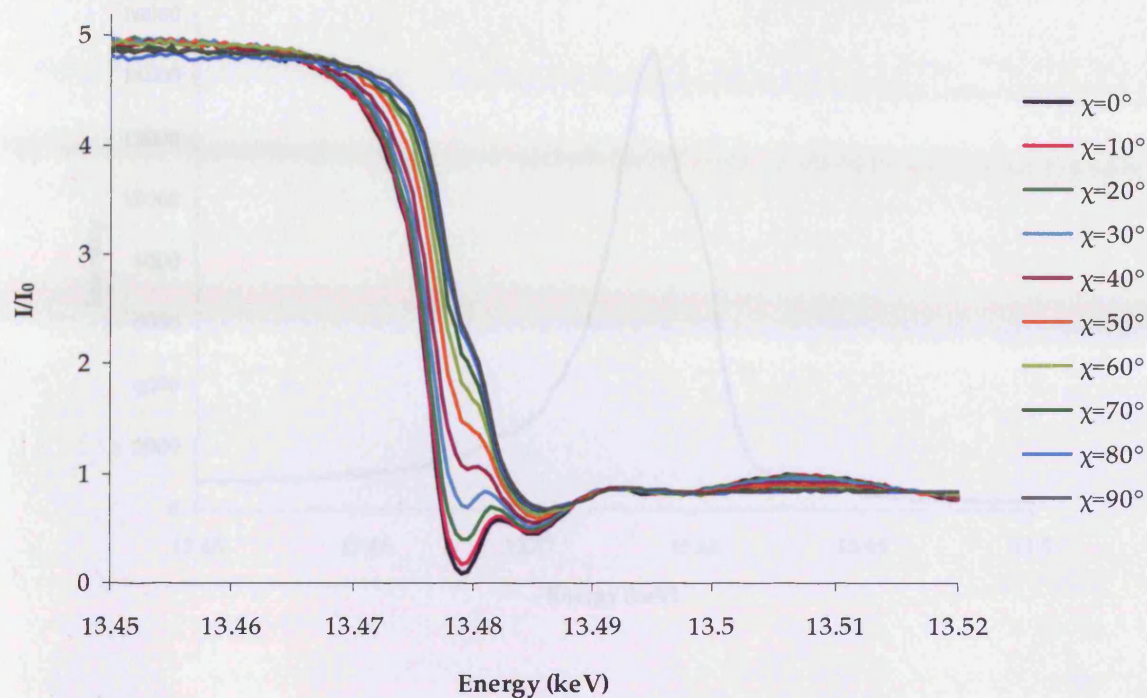


Figure 4.13 X-ray transmittance (I/I_0) measured on 2-BA/TIC as a function of energy close to the bromine K-edge for a range of χ values from $\chi = 0^\circ$ (parallel) to $\chi = 90^\circ$ (perpendicular).

X-ray birefringence measurements were also carried out for 2-BA/TIC, with interesting results. As observed previously for 1-BA/TIC (section 4.3), the maximum X-ray birefringence for 2-BA/TIC is also observed at 45° (Figure 4.14, Figure 4.15). Figure 4.15 shows the evolution of the X-ray birefringence for different crystal orientations, including several intermediate orientations between parallel ($\chi = 0^\circ$) and perpendicular ($\chi = 90^\circ$) orientations.

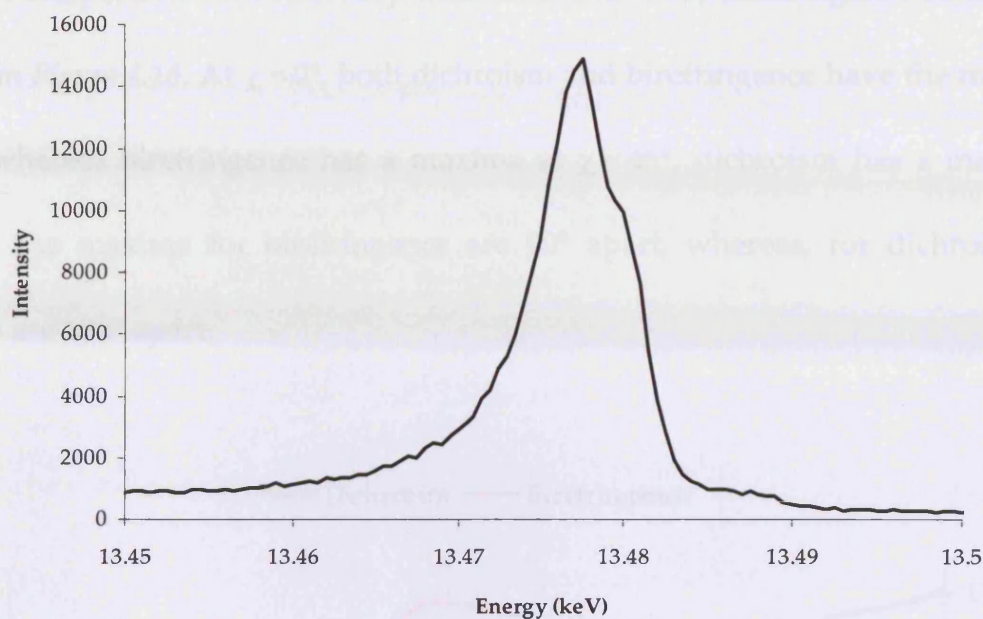


Figure 4.14 X-ray birefringence measurement for 2-BA/TIC.

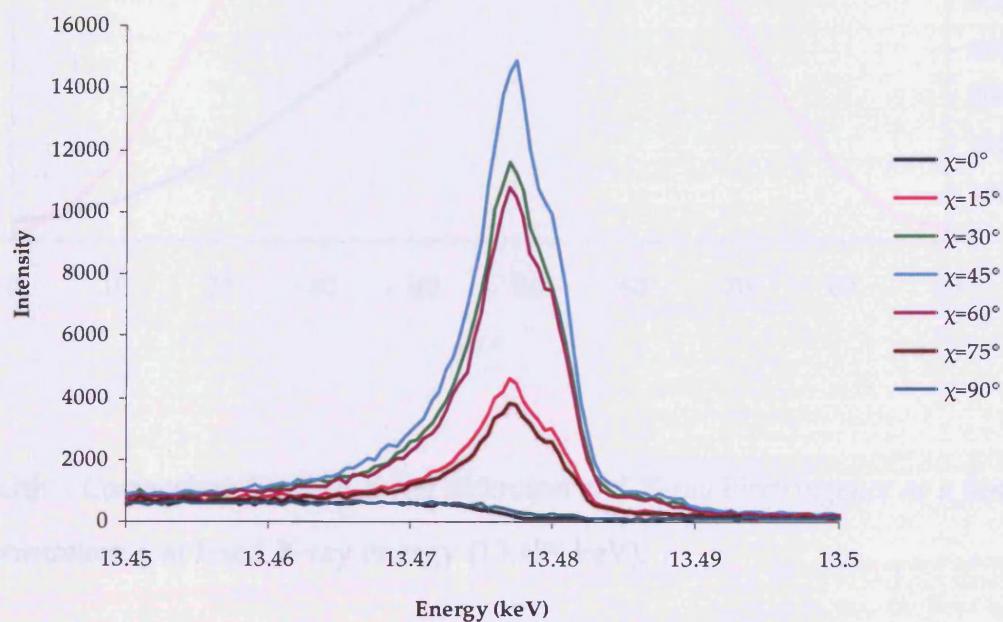


Figure 4.15 X-ray birefringence for different χ values, with maximum birefringence observed at $\chi = 45^\circ$.

A comparison between X-ray dichroism and X-ray birefringence behaviour is shown in Figure 4.16. At $\chi = 0^\circ$, both dichroism and birefringence have the minimum value, whereas birefringence has a maxima at $\chi = 45^\circ$, dichroism has a maxima at $\chi = 90^\circ$. The maxima for birefringence are 90° apart, whereas, for dichroism, the maxima are 180° apart.

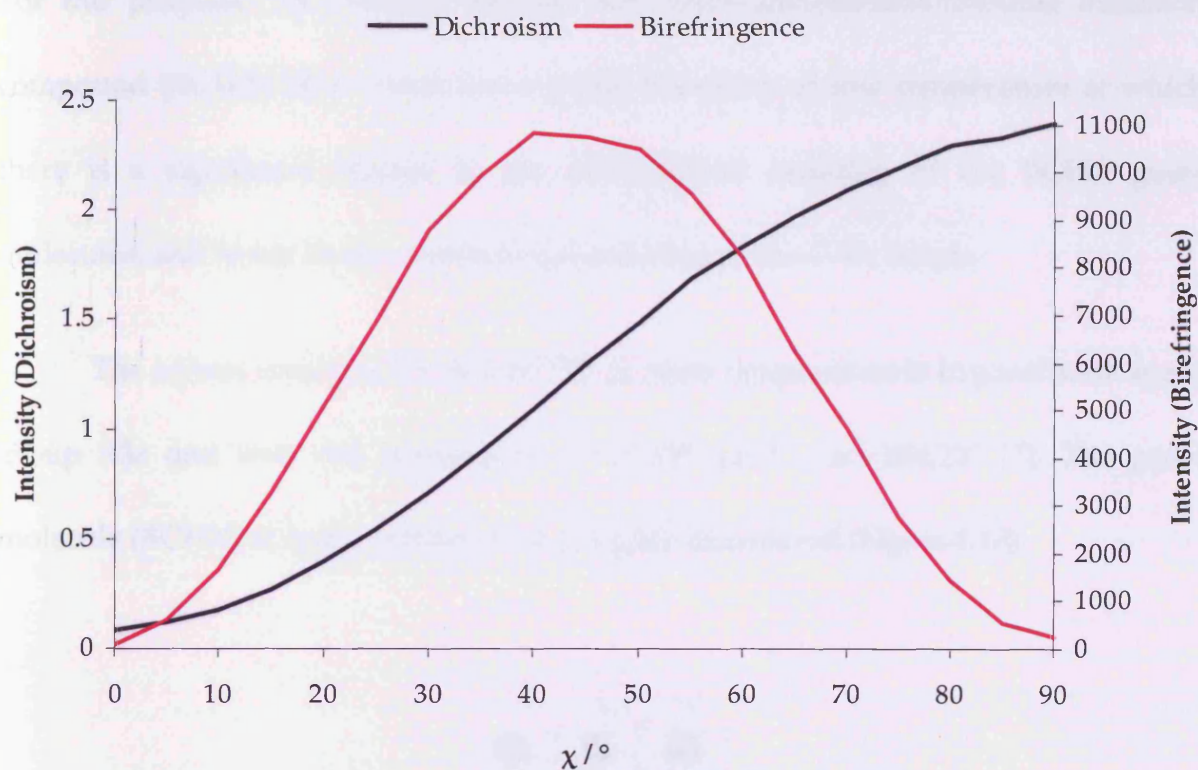


Figure 4.16 Comparison between X-ray dichroism and X-ray birefringence as a function of crystal orientation χ at fixed X-ray energy (13.479 keV).

4.5 – Bromocyclohexane / Thiourea Inclusion Compound

In this section X-ray dichroism and X-ray birefringence experiments are approached from a different perspective. The ultimate aim here is to utilize such measurements as a means of evaluating the C–Br bonds orientations in the crystal. For this purpose, the material studied was bromocyclohexane/thiourea inclusion compound (BCHX/TIC), which has a phase transition at low temperature at which there is a significant change in the orientational ordering of the BCHX guest molecules, and hence in the orientational ordering of the C–Br bonds.

The crystal structure for BCHX/TIC at room temperature is trigonal with space group $R\bar{3}c$ and unit cell parameters: $a = 10.193\ (3)\ \text{\AA}$, $\alpha = 104.23^\circ$ [7]. The guest molecule (BCHX) at room temperature is highly disordered (*Figure 4.17*).

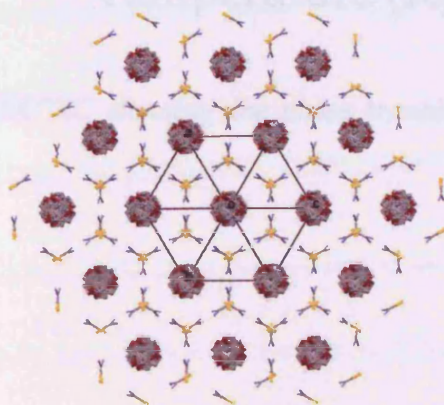


Figure 4.17 Crystal structure of BCHX/TIC viewed along the c -axis.

BCHX/TIC undergoes a phase transition at 233 K (232 K on cooling and 234 K on heating) (Figure 4.18), associated with a lowering of the crystal symmetry from rhombohedral to monoclinic, seen in Figure 4.19 as the appearance of extra peaks in the powder X-ray diffraction pattern (PXRD).

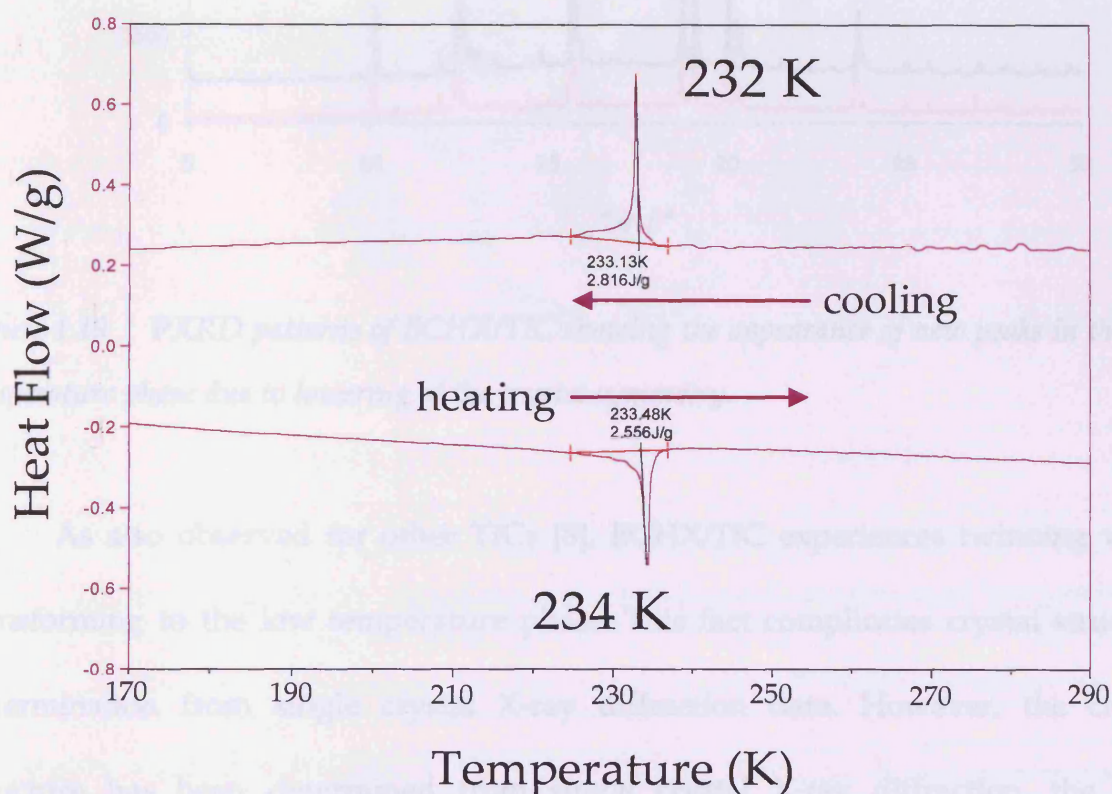


Figure 4.18 DSC for BCHX/TIC showing the phase transition at 232 K on cooling and 234 K on heating. (Exo up)

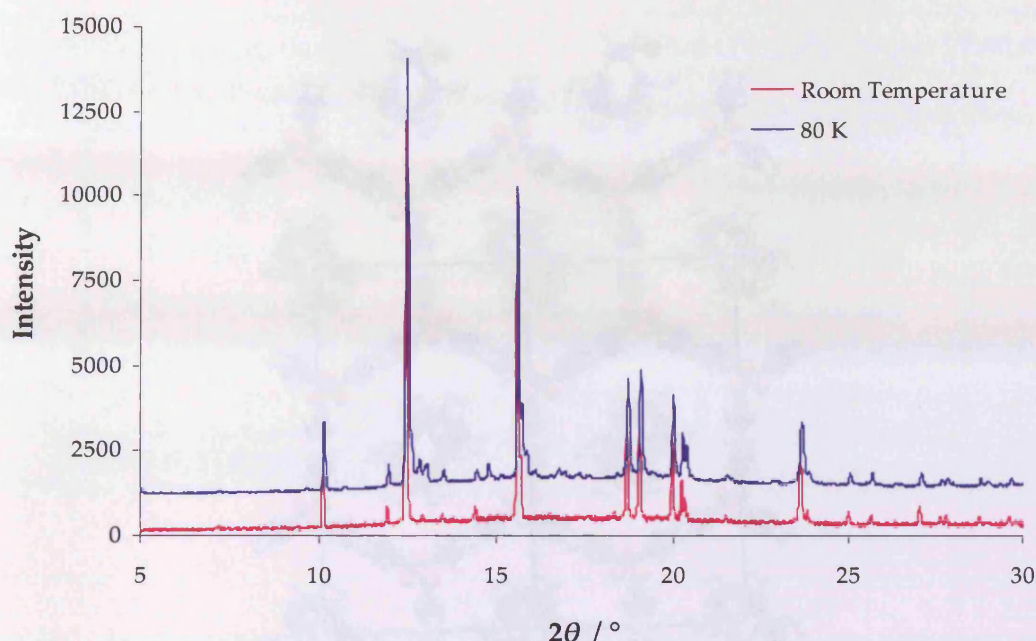


Figure 4.19 PXRD patterns of BCHX/TIC showing the appearance of new peaks in the low temperature phase due to lowering of the crystal symmetry.

As also observed for other TICs [8], BCHX/TIC experiences twinning when transforming to the low temperature phase. This fact complicates crystal structure determination from single crystal X-ray diffraction data. However, the crystal structure has been determined from single crystal X-ray diffraction, the low-temperature phase of BCHX/TIC is monoclinic with space group $P2_1/a$ and unit cell parameters: $a = 9.653 \text{ \AA}$, $b = 15.956 \text{ \AA}$, $c = 12.286 \text{ \AA}$, $\beta = 111.83^\circ$ ($R1 = 0.0644$, $wR2 = 0.1436 [I > 2\sigma(I)]$) (Figure 4.20) (See Appendix C for extended crystallographic data). BCHX/TIC shares structural characteristics (similar unit cell parameters and the same space group) with the isostructural materials chlorocyclohexane/TIC [9-11] and cyclohexane/TIC [12, 13].

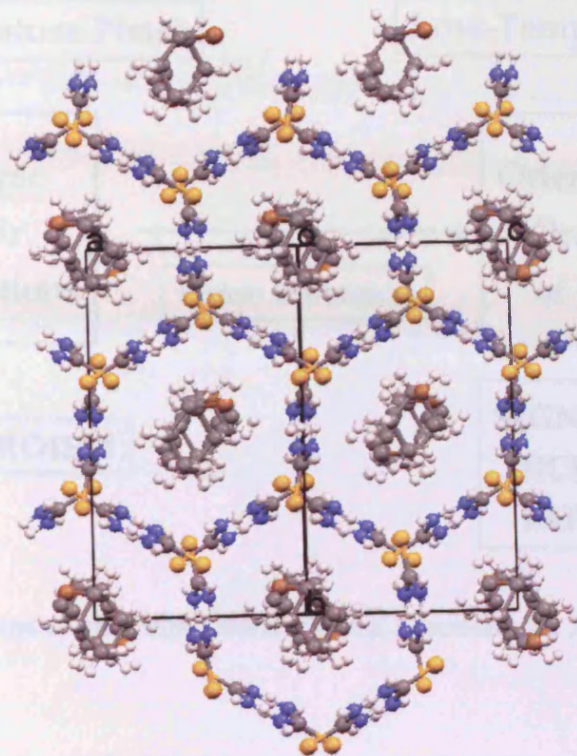


Figure 4.20 Crystal structure of BCHX/TIC viewed along the tunnel direction.

Concerning the X-ray dichroism and birefringence experiments, for a material with a disordered distribution of the C–Br bonds at room temperature that undergoes a phase transition involving ordering of the C–Br bond orientations, significant dichroism and therefore birefringence are expected only in the low-temperature phase (Figure 4.21). Thus, X-ray dichroism and X-ray birefringence measurements should serve as a sensitive probe of changes in molecular orientation at such phase transitions, and the present work represents the first attempts to explore this issue.

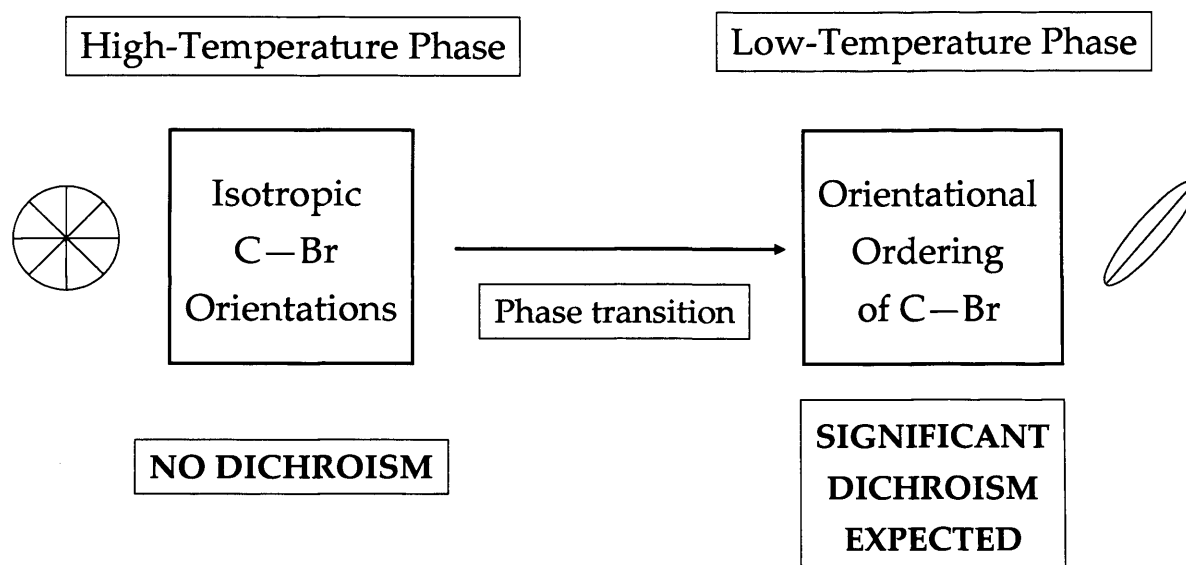


Figure 4.21 Implications of an order-disorder phase transition on X-ray dichroism.

X-ray dichroism and birefringence experiments were carried out on BCHX/TIC over a range of temperatures above and below the phase transition (233 K). No significant dichroism was observed in the high temperature phase (Figure 4.22) for the temperatures studied (300 K and 250 K). However, at the temperatures studied below the phase transition (200 K, 150 K and 100 K), BCHX/TIC showed significant dichroism. Furthermore, a decrease in the R_γ is observed when cooling the material within the low-temperature phase, reaching a low value of 0.65 at 100K (Figure 4.23). This observation suggests that there is a progressive increase in the degree of orientational ordering of the C—Br bonds as the temperature is decreased within the low-temperature phase.

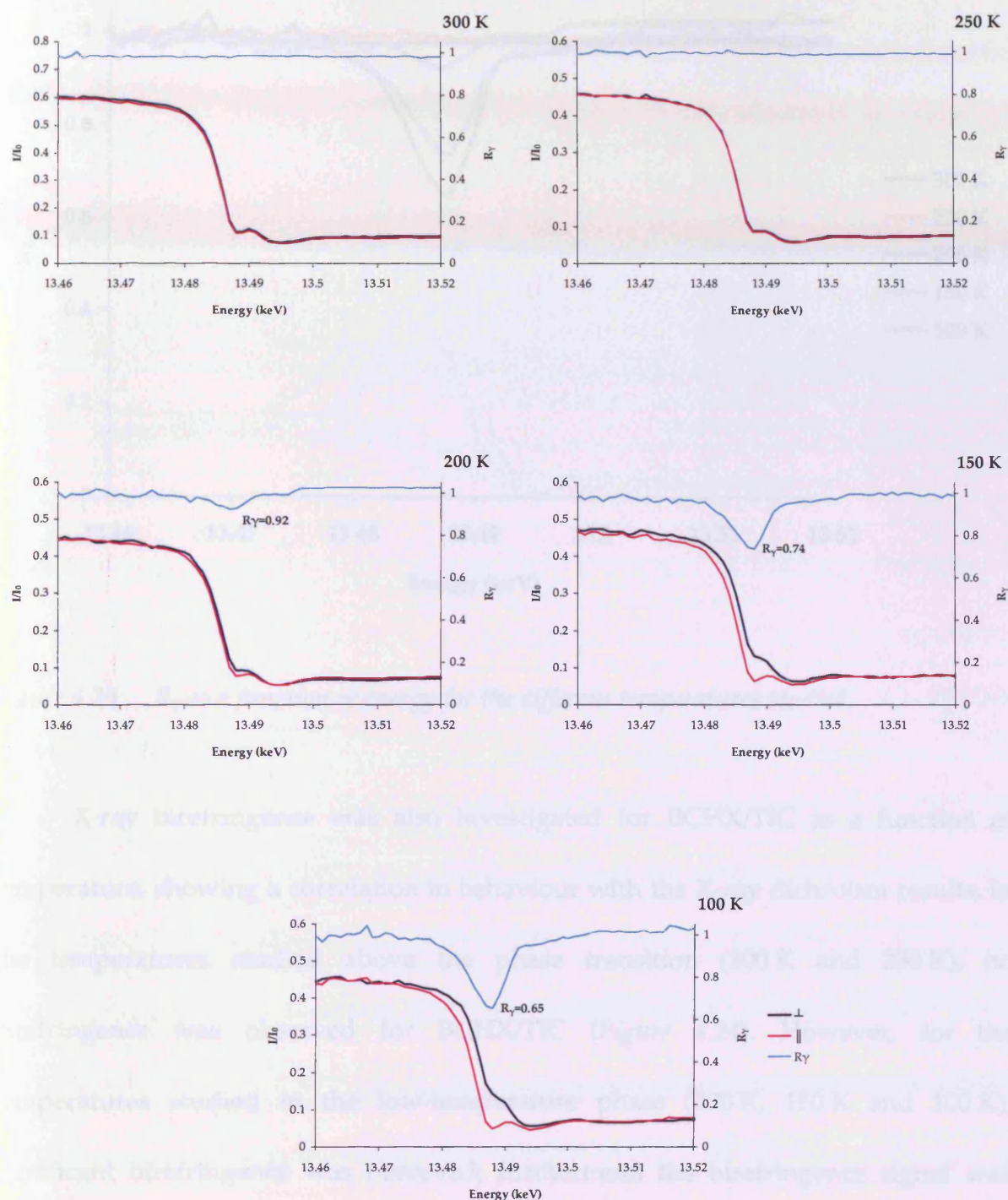


Figure 4.22 X-ray transmittance (I/I_0) of BCHX/TIC as a function of energy at different temperatures. R_γ is also shown for the different temperatures.

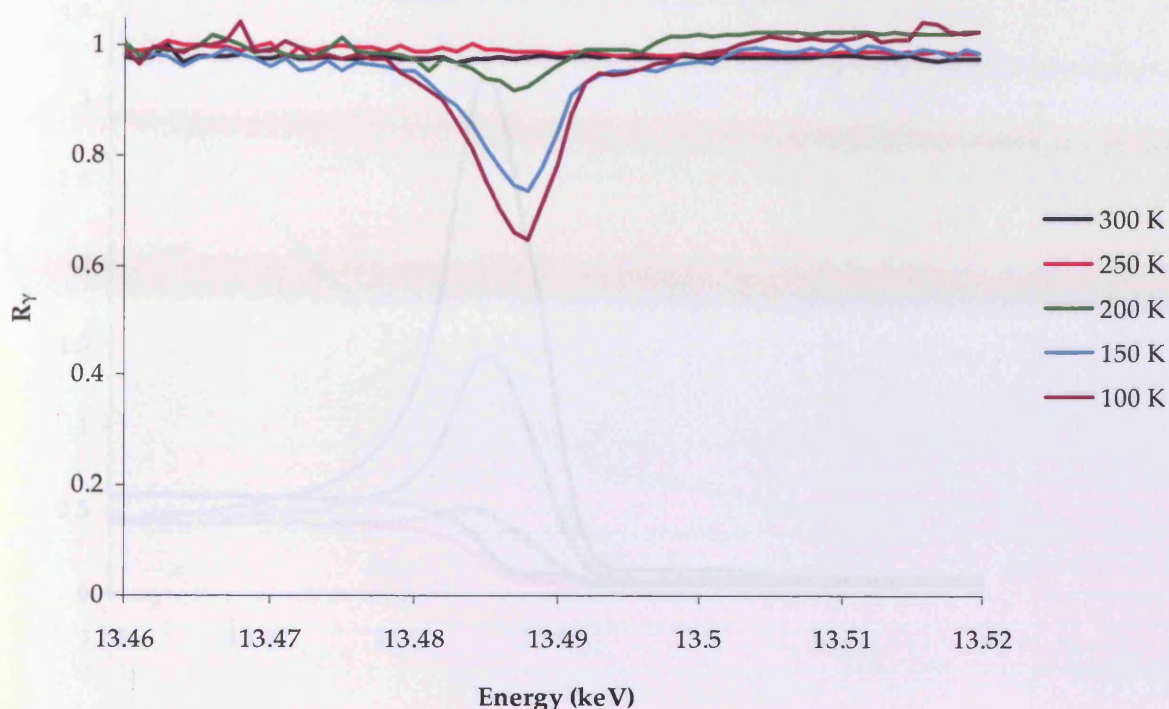


Figure 4.23 R_γ as a function of energy for the different temperatures studied.

X-ray birefringence was also investigated for BCHX/TIC as a function of temperature, showing a correlation in behaviour with the X-ray dichroism results. In the temperatures studied above the phase transition (300 K and 250 K), no birefringence was observed for BCHX/TIC (Figure 4.24). However, for the temperatures studied in the low-temperature phase (200 K, 150 K and 100 K), significant birefringence was observed; furthermore the birefringence signal was observed to increase as temperature was decreased within the low-temperature phase.

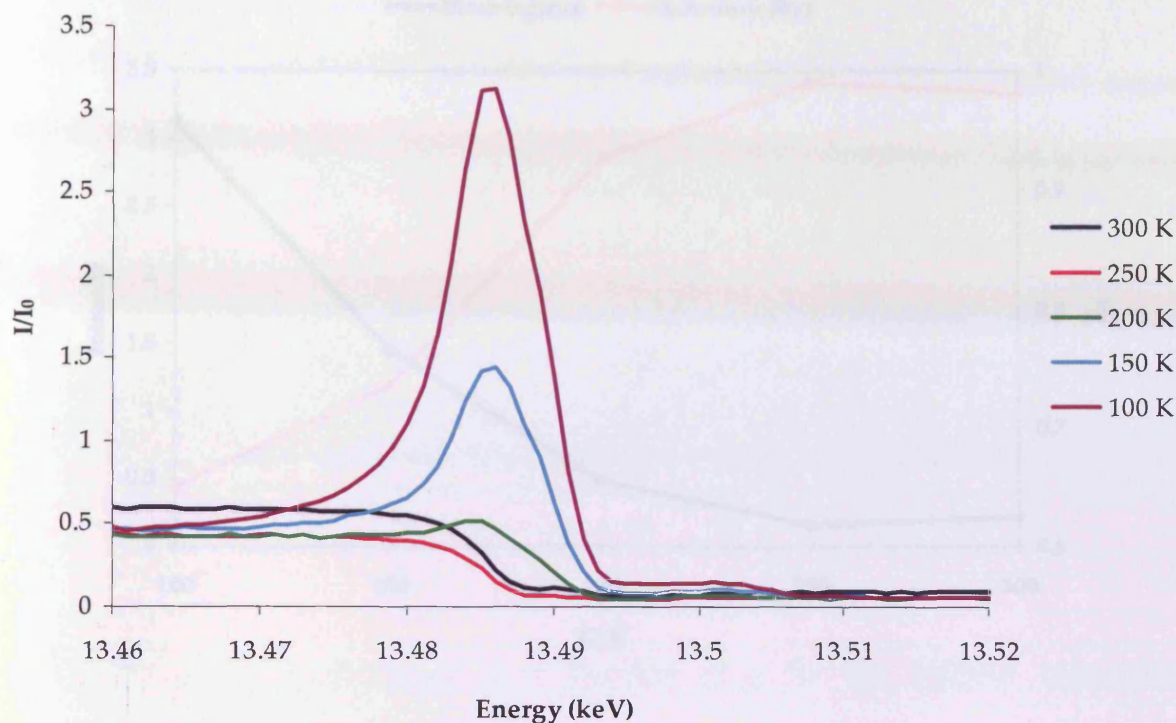


Figure 4.24 X-ray birefringence intensity as a function of energy for the different temperatures investigated.

Both X-ray dichroism and X-ray birefringence emerge only in the low-temperature phase (below 233 K) (Figure 4.25). In addition, an enhancement in the X-ray dichroism (lower R_γ values imply stronger dichroism) and X-ray birefringence is observed as the temperature is decreased within the low temperature phase, suggesting a progressive increase in the ordering of the C–Br orientations (instead of a sudden transition to a completely ordered state at the phase transition temperature).

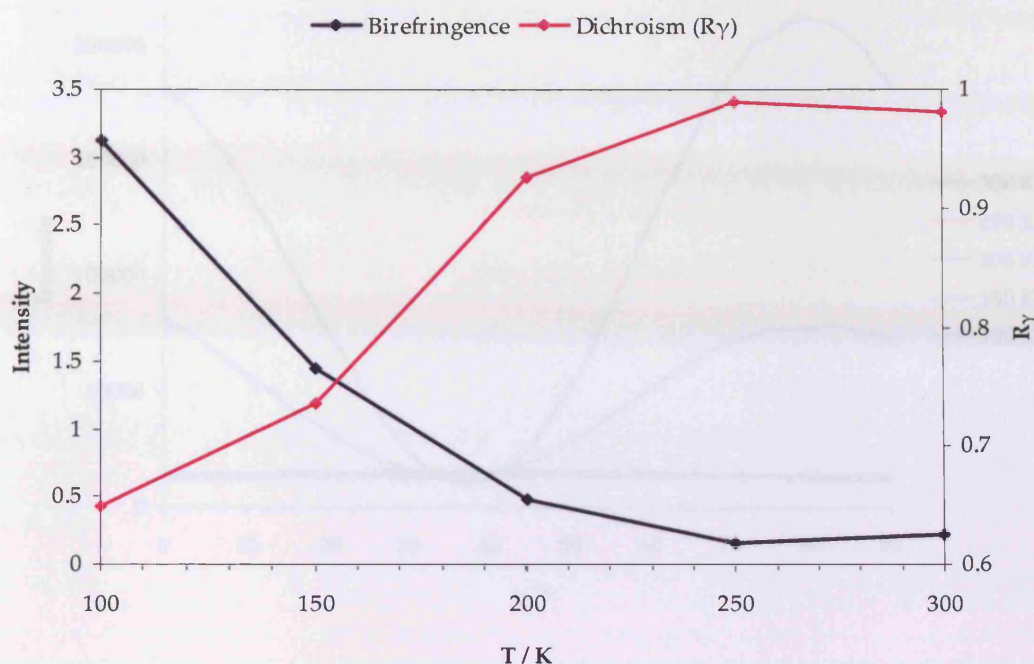


Figure 4.25 X-ray dichroism and X-ray birefringence results on BCHX/TIC as a function of temperature.

It is remarkable to note that the X-ray birefringence signal in the low temperature phase depends not only on χ (Figure 4.26) but also depends on ϕ (Figure 4.27). Nevertheless, this dependence is not apparent immediately at the phase transition temperature, but appears only within the low temperature phase, supporting the idea that orientational ordering does not occur abruptly at the phase transition. Interestingly, it seems that the dependence on χ appears at higher temperatures than ϕ , which suggests that the ordering of the C–Br bonds of the BCHX molecules occurs initially with respect to tunnel axis, and subsequently with respect to orientation around the tunnel axis.

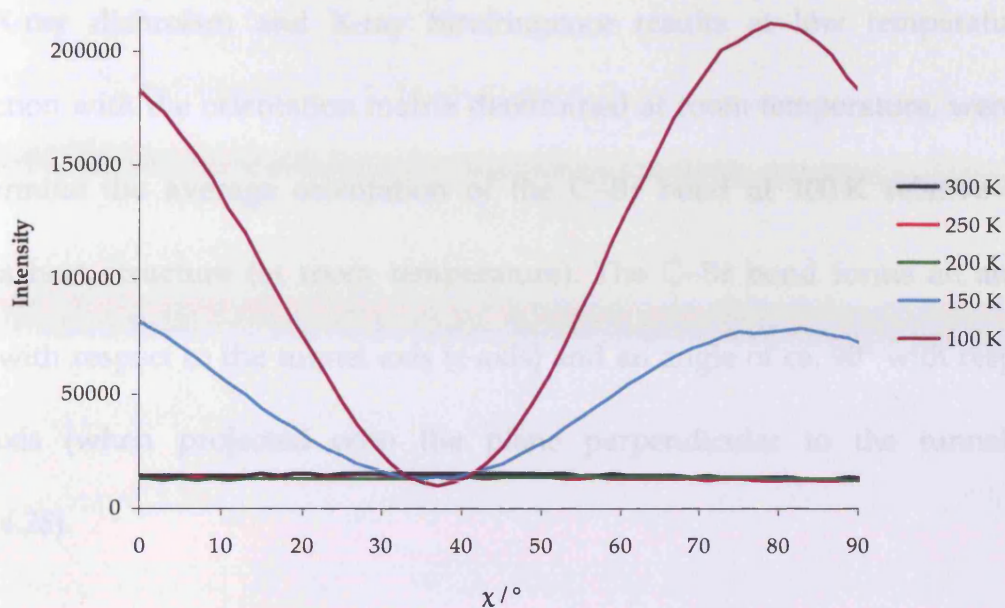


Figure 4.26 X-ray birefringence as a function of χ for the different temperatures investigated at fixed energy (13.485 keV)

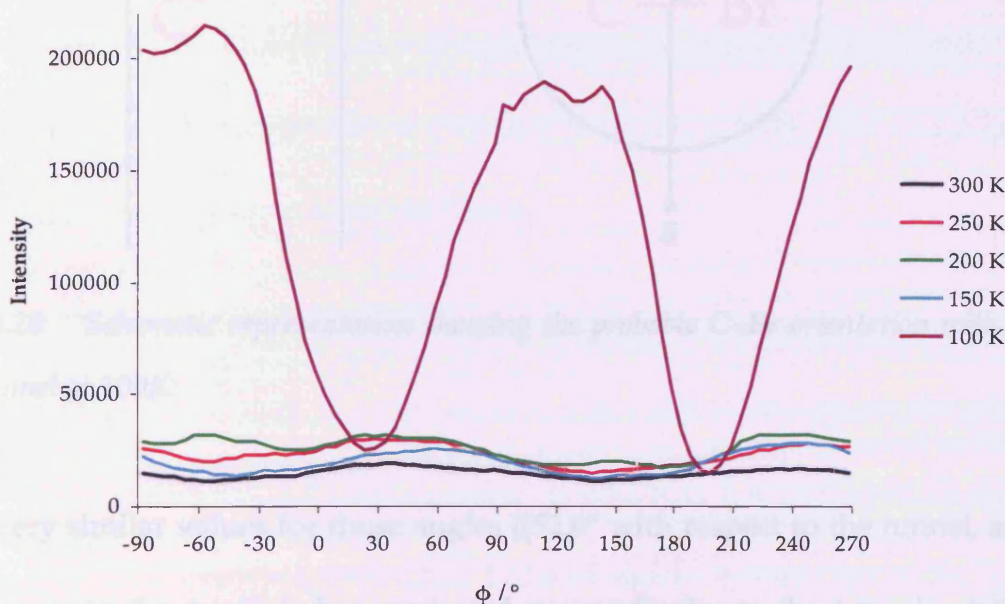


Figure 4.27 X-ray birefringence as a function of ϕ for the different temperatures studied at fixed energy (13.485 keV).

X-ray dichroism and X-ray birefringence results at low temperature, in conjunction with the orientation matrix determined at room temperature, were used to determine the average orientation of the C–Br bond at 100 K relative to the thiourea host structure (at room temperature). The C–Br bond forms an angle of ca. 55° with respect to the tunnel axis (c -axis) and an angle of ca. 90° with respect to the a -axis (when projected onto the plane perpendicular to the tunnel axis) (Figure 4.28).

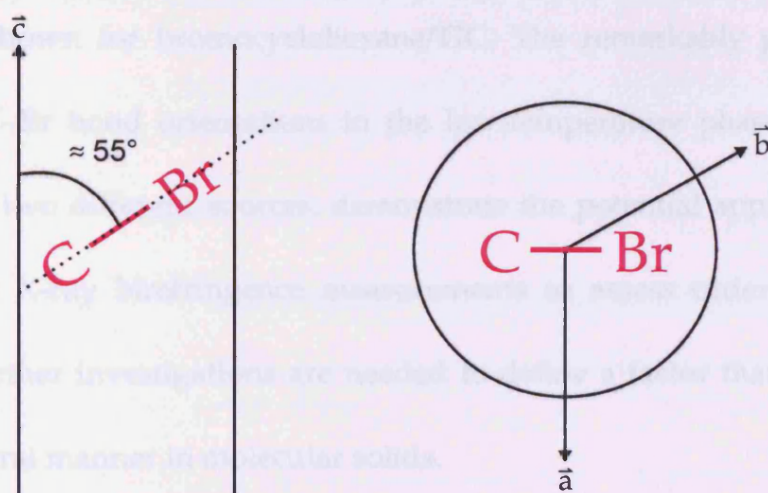


Figure 4.28 Schematic representation showing the probable C–Br orientation with respect to the tunnel at 100K.

Very similar values for those angles [52.6° with respect to the tunnel, and 85° with respect to the a -axis (when projected perpendicular to the tunnel axis)] were determined independently from the structural characterization of the low-temperature phase of BCHX/TIC from single crystal X-ray diffraction.

4.6 – Conclusions and Future Work

X-ray dichroism and X-ray birefringence experiments reported in this chapter clearly demonstrate that there is an unambiguous correlation between the orientational ordering of the C–Br bonds in the guest molecules and the extent of dichroism and birefringence observed. We have demonstrated for the first time that order-disorder phase transitions can be diagnosed by an increase in the birefringence signal and a decrease of the R_γ value when the degree of orientational order increases, as shown for bromocyclohexane/TIC. The remarkably good agreement between the C–Br bond orientations in the low-temperature phase of BCHX/TIC, obtained from two different sources, demonstrate the potential application of X-ray dichroism and X-ray birefringence measurements to assess order-disorder phase transitions. Further investigations are needed to define a factor that could quantify order in a general manner in molecular solids.

Both 2-bromoadamantane/TIC and 1-bromoadamantane/TIC, are potentially suitable materials to be used as X-ray dichroic filters due to the significant dichroism shown close to the bromine K-edge energies. In addition, it is important to note that, although the TIC crystals studied herein become slightly brown after a few hours of being exposed to X-rays (Figure 4.29), suggesting some extent of sample degradation, no deterioration of the dichroic properties is observed.

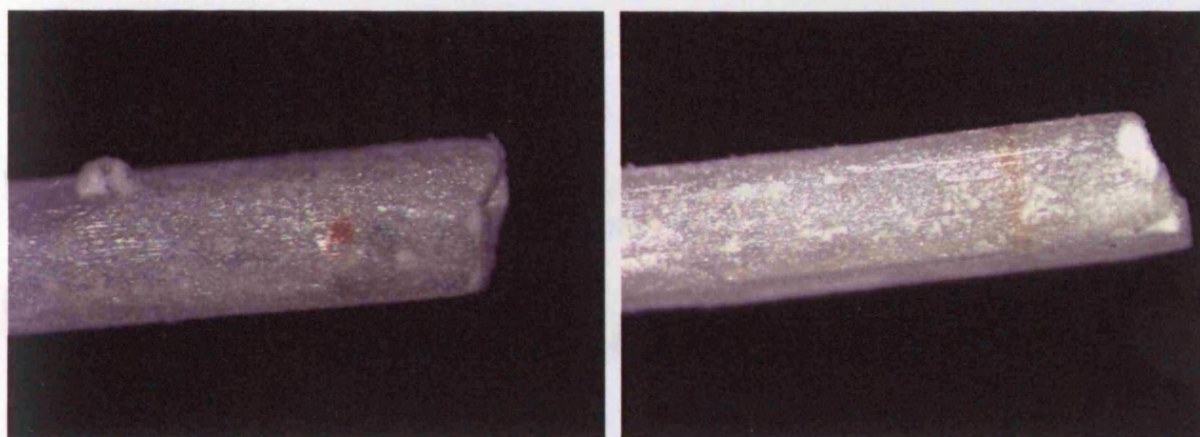


Figure 4.29 Photographs of a TIC single crystal after a few hours of exposure to X-rays. Brown colouration can be observed revealing the X-ray beam path. Left: brown spot, crystal perpendicular to the beam. Right: brown line, crystal parallel to the beam.

The investigations in this chapter are focused only on TICs containing C–Br bonds, however expanding the range of X-ray energies (by analysing materials with other elements instead of Br, such as Cu, I and Fe) would be enlightening.

- [10] P. A. Schofield, K. D. M. Harris, I. J. Shannon and A. J. O. Richards, *J. Chem. Soc. Chem. Commun.*, 1288–1295 (1998)
- [11] M. J. Jopek, I. J. Shannon and K. D. M. Harris, *J. Chem. Soc. Perkin Trans. 2*, 325–329 (1996)
- [12] A. Desmet, S. J. Kim, F. Guillaume, M. Couzi, K. D. M. Harris and E. H. Rezakhanlou, *Phys. Rev. B*, 64, 1–21 (2001)
- [13] Z. Fan, A. Desmet, E. J. MacLennan, F. Guillaume and K. D. M. Harris, *J. Phys. Chem. C*, 112, 839–847 (2008)

4.7 – References

- [1] S. P. Collins, D. Laundy, K. D. M. Harris, B. M. Kariuki, C. L. Bauer, S. D. Brown and P. Thompson, *J. Phys. Cond. Matt.*, **14**, 123-134 (2002)
- [2] M. H. Chao, B. M. Kariuki, K. D. M. Harris, S. P. Collins and D. Laundy, *Angew. Chem. Int. Ed.*, **42**, 2982-2985 (2003)
- [3] N. P. Bannister, K. D. M. Harris, S. P. Collins, A. Martindale, P. S. Monks, G. Solan and G. W. Fraser, *Exp. Astron.*, **21**, 1-12 (2006)
- [4] E. H. Land, *J. Opt. Soc. Am.*, **41**, 957-963 (1951)
- [5] H. You, *J. Appl. Cryst.*, **32**, 614-623 (1999)
- [6] G. M. Sheldrick, *Acta Cryst. A*, **64**, 112-122 (2008)
- [7] T. Ishibashi, M. Machida and N. Koyano, *J. Korean Phys. Soc.*, **46**, 228 (2005)
- [8] L. Yeo, K. D. M. Harris and B. M. Kariuki, *J. Sol. State Chem.*, **156**, 16-25 (2001)
- [9] K. D. M. Harris and J. M. Thomas, *J. Chem. Soc. Farad. Trans.*, **86**, 1095-1101 (1990)
- [10] P. A. Schofield, K. D. M. Harris, I. J. Shannon and A. J. O. Rennie, *J. Chem. Soc. Chem. Commun.*, 1293-1295 (1993)
- [11] M. J. Jones, I. J. Shannon and K. D. M. Harris, *J. Chem. Soc. Farad. Trans.*, **92**, 273-279 (1996)
- [12] A. Desmedt, S. J. Kitchin, F. Guillaume, M. Couzi, K. D. M. Harris and E. H. Bocanegra, *Phys. Rev. B*, **64**, 1-21 (2001)
- [13] Z. Pan, A. Desmedt, E. J. MacLean, F. Guillaume and K. D. M. Harris, *J. Phys. Chem. C*, **112**, 839-847 (2008)

Chapter 5

Solid-State Reaction and Polymorphism of Oxalyl Dihydrazide at High Temperature

5.1 – Introduction

The phenomenon of polymorphism, first reported by Mitscherlich in 1821 [1], is abundant in crystalline solids. One of the most popular examples for inorganic materials is silicon dioxide [SiO₂], which exists in various forms such as α -quartz, β -quartz and tridymite amongst others. Polymorphism arises when two or more elements or compounds have the same chemical composition but different crystal structures. As a consequence, the solid-state properties of different polymorphs are

typically very different. The upsurge of polymorphism research in recent years resides in industrial interest, especially in pharmacy, pigments, explosives, agrochemicals and even food; for example, cocoa butter exists in six different polymorphs [2]. Thus far, the largest number of polymorphs reported in the Cambridge Structural Database (CDS) for a particular organic system is seven. That material is 5-methyl-2-[(2-nitrophenyl)amino]-3-thiophenecarbonitrile, known as ROY [3, 4] for its colour properties (the different polymorphs have different colours, including red, orange and yellow).

Another organic compound with a significant number of polymorphs is oxalyl dihydrazide (ODH) (*Figure 5.1*) [5, 6] for which the crystal structures for five polymorphs (α , β , γ , δ , ϵ) have been determined. In addition, the relative thermodynamic stability of the polymorphs and solid-state transformations between the polymorphs have been investigated.

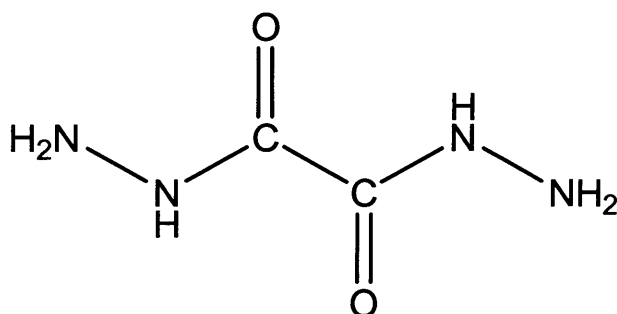


Figure 5.1 Scheme showing the oxalyl dihydrazide (ODH) molecule.

Until now, the α , γ , δ , and ε polymorphs have been crystallized consistently as monophasic samples following the described crystallization conditions [6, 7]. However, the β polymorph has been prepared only once, and was obtained as a mixture with the α polymorph. All subsequent attempts to prepare the β polymorph have been unsuccessful, suggesting an “elusive polymorph” [8]. As a result, the β polymorph could not be analyzed in the present work.

The crystal structures of all ODH polymorphs (*Table 5.1*) are monoclinic, with space group $P2_1/c$, and in all cases the molecule has a trans-trans-trans conformation of the N–N–C–C–N–N backbone. The orientations of the NH_2 groups relative to the backbone (different NH– NH_2 torsional angles) and the hydrogen bonding array are different in the different polymorphs.

| | Crystallographic system | <i>a</i> (Å) | <i>b</i> (Å) | <i>c</i> (Å) | β (°) | Space group | <i>Z</i> | Unit Cell Volume (Å ³) |
|---------------|-------------------------|--------------|--------------|--------------|-------------|-------------|----------|------------------------------------|
| α | Monoclinic | 3.6221(4) | 6.8322(7) | 9.1294(10) | 99.298(9) | $P2_1/c$ | 2 | 222.96(4) |
| β | Monoclinic | 3.762(4) | 11.652(5) | 5.619(2) | 92.793(5) | $P2_1/c$ | 2 | 246.0(3) |
| γ | Monoclinic | 5.0795(4) | 14.6679(14) | 7.0345(7) | 114.160(6) | $P2_1/c$ | 4 | 478.20(3) |
| δ | Monoclinic | 3.6608(5) | 14.550(2) | 5.0646(8) | 119.006(9) | $P2_1/c$ | 2 | 235.93(6) |
| ε | Monoclinic | 5.3642(3) | 3.8412(2) | 12.3191(6) | 108.999(3) | $P2_1/c$ | 2 | 240.01(2) |

Table 5.1 Summary of the crystal structure parameters for the five known ODH polymorphs.

Although the crystal structures were solved by single crystal X-ray diffraction, powder X-ray diffraction (PXRD) data were also recorded on the samples to ensure that the single crystal chosen for the experiment was representative of the bulk. The experimental PXRD patterns (left) and the simulated PXRD patterns for the five polymorphs are shown in *Figure 5.2*. All experimental PXRD patterns shown, correspond to pure phases (α , γ , δ , ϵ) with the exception of the β polymorph, which could only be crystallized as a mixture with the α polymorph (marked with * in *Figure 5.2*).

The ODH molecule in the α , β , δ and ϵ polymorphs is located on a crystallographic inversion centre, and, thus, the molecular conformation is centrosymmetric, and the asymmetric unit consists of half of the ODH molecule. For these polymorphs, the volume of the unit cell is comparable. However, in the γ polymorph, the asymmetric unit consists of one ODH molecule, and the unit cell volume is roughly twice that of the other polymorphs. Further structural characteristics and details of the hydrogen bonding in the different polymorphs are discussed elsewhere [6, 7].

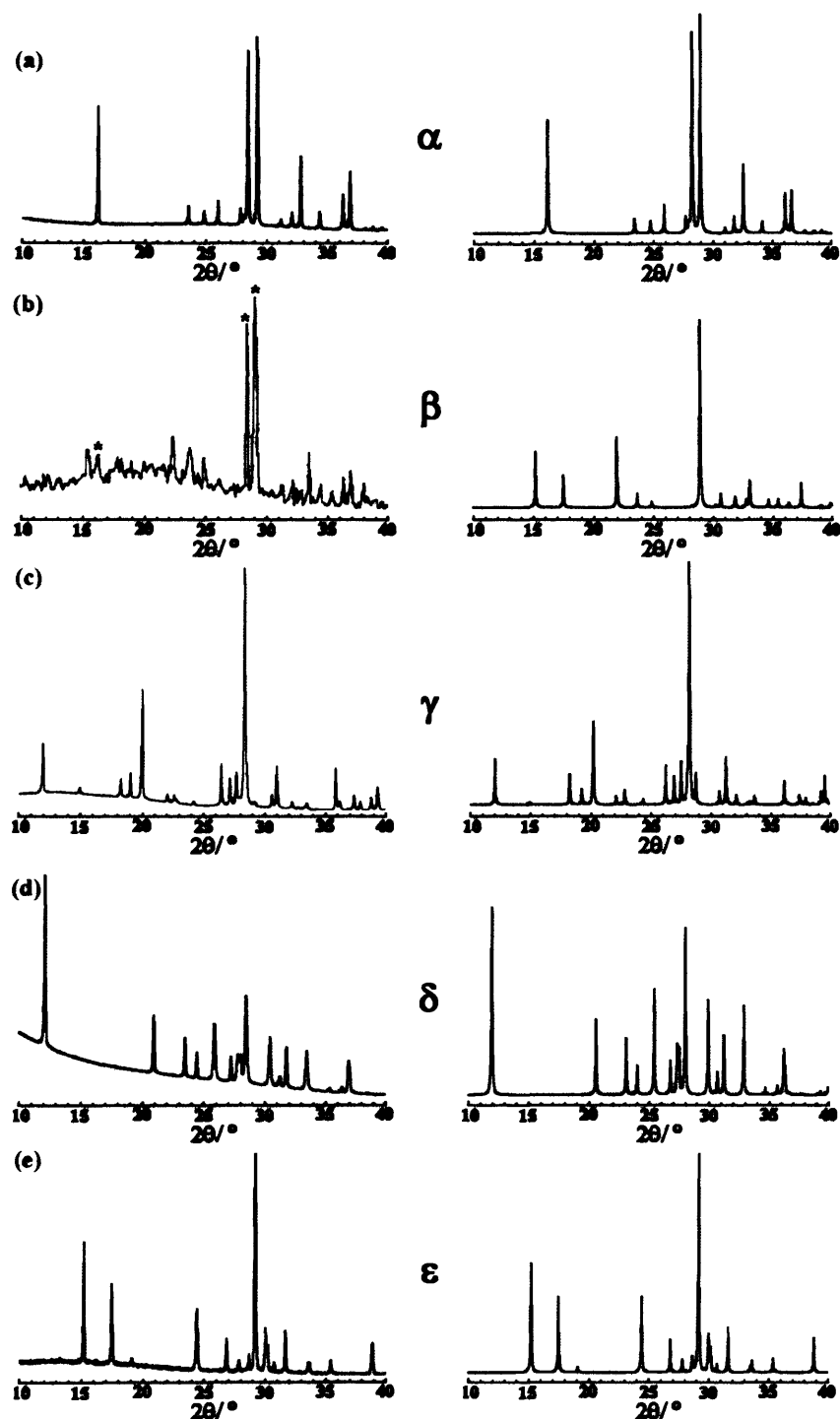


Figure 5.2 PRXD patterns for the five known ODH polymorphs. (a) α polymorph, (b) β polymorph, (c) γ polymorph, (d) δ polymorph, (e) ϵ polymorph. The PRXD patterns on the left side are experimental and the PRXD patterns on the right are simulated using the structures determined from single crystal X-ray diffraction data [6].

The relationship between the different ODH polymorphs, and their relative thermodynamic stabilities were also investigated at high temperature [6, 7]. Differential Scanning Calorimetry (DSC) measurements performed on the four polymorphs α , γ , δ and ϵ (Figure 5.3) uncovered a solid-state reaction for all the polymorphs at ca. 250 °C, prior to melting. In addition, DSC data for the α , δ and ϵ polymorphs include another endothermic peak below the temperature of the solid-state reaction (208 °C for α , 212 °C for δ and 210.3 °C for ϵ) corresponding to an irreversible phase transition to produce the γ polymorph. For the γ polymorph, no thermal events were observed preceding the solid-state reaction.

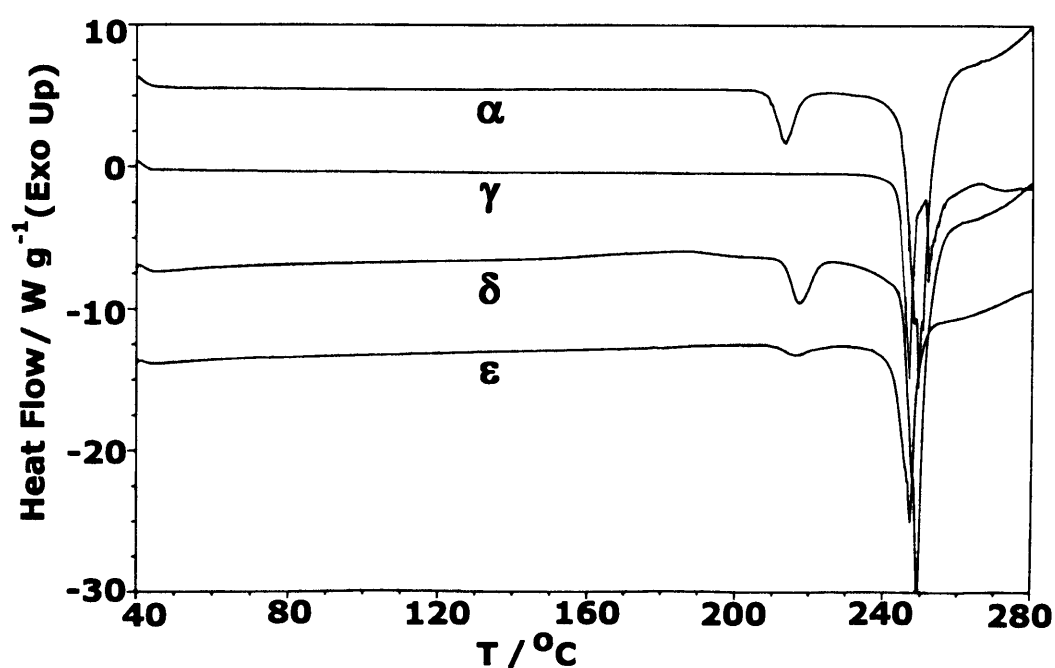


Figure 5.3 DSC data for the α polymorph, γ polymorph, δ polymorph and ϵ polymorph of ODH [6].

According to the “heat of transition rule” [9, 10], the endothermic polymorphic transformation suggests that the α , δ , and ϵ polymorphs have an enantiotropic relationship to the γ polymorph, which is assigned as the most stable polymorph at high temperature. At room temperature, observations suggest that the α polymorph is the most stable polymorph.

The products of the solid-state reaction (*Figure 5.4*) (large endothermic peak around 250 °C) are *N,N'*-dioxalylhydrazidylhydrazine (DOHH) and hydrazine (gaseous at the temperature at which the reaction takes place). In earlier investigations [7], the product (DOHH) crystal structure was solved from PXRD data. DOHH belongs to the orthorhombic system and space group *Fdd2*, the unit cell parameters are $a = 13.948 \text{ \AA}$, $b = 25.508 \text{ \AA}$, $c = 4.7841 \text{ \AA}$, and the unit cell volume is 1702.11 \AA^3 .

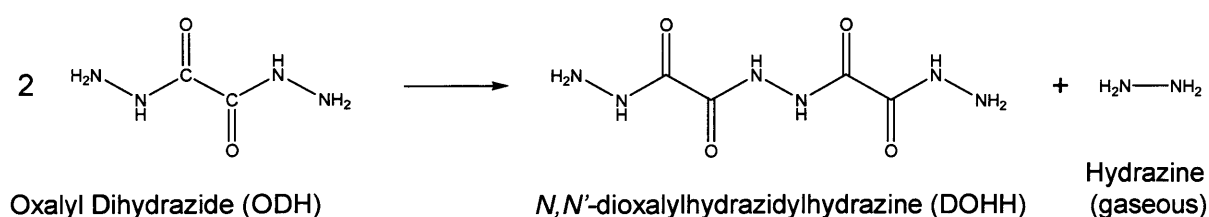


Figure 5.4 Scheme of the ODH solid-state reaction.

Preliminary time-resolved high-temperature PXRD experiments using laboratory equipment were performed in the past [7]. However, the quality of the data obtained was not sufficient to draw conclusions and rapid transformations may have been neglected due to the longer time required for each scan. For these reasons, higher quality data were collected again with synchrotron radiation and are reported in this chapter, focusing especially on the α polymorph.

5.2 – Experimental

Following the previous work with ODH [6, 7], the behaviour of the different known polymorphs (with the exception of the β polymorph, see section 5.1) was further investigated using the synchrotron facilities at Daresbury SRS. The experiments were carried out at station 6.2 [11, 12] using time-resolved high-temperature powder X-ray diffraction (*Figure 5.5*). The wavelength for the X-rays was fixed at 1.4 Å.

The curved WAXS (Wide-Angle X-ray Scattering) detector (*Figure 5.5* and *Figure 5.6*) allowed the simultaneous collection of data in a 2θ range of 60° . Fast time resolution was then achieved, which was necessary to study the abrupt and rapid transformations among the different ODH polymorphs as a function of time. Good quality PXRD data were recorded in just 10 seconds.

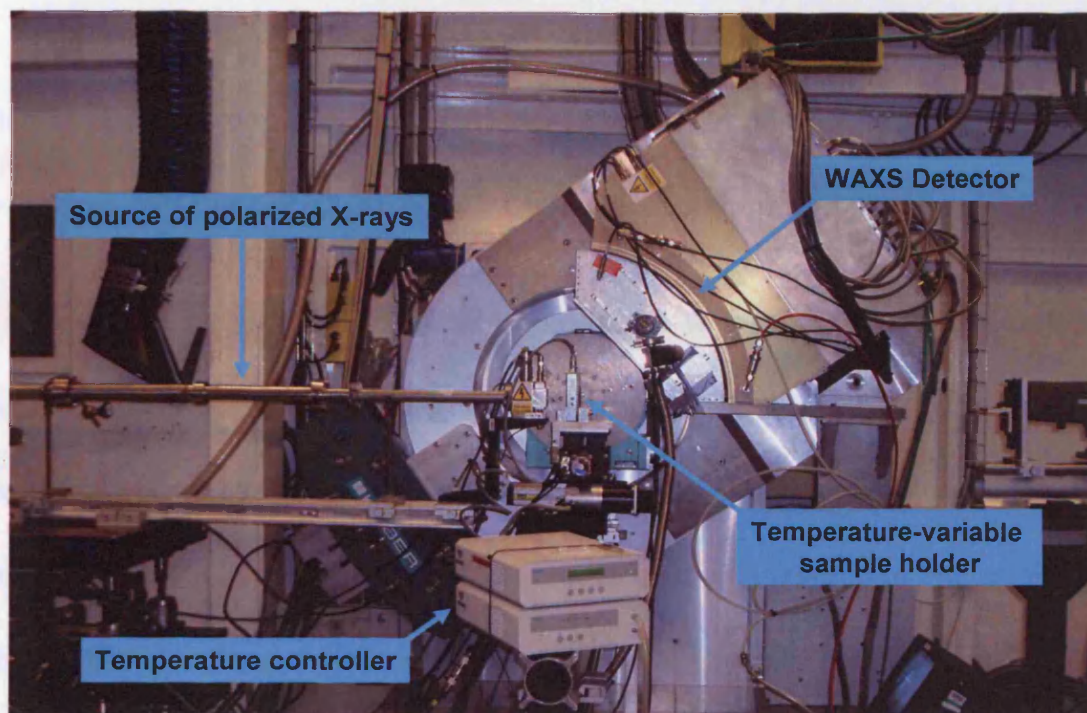


Figure 5.5 Experimental set up of station 6.2 at Daresbury SRS.

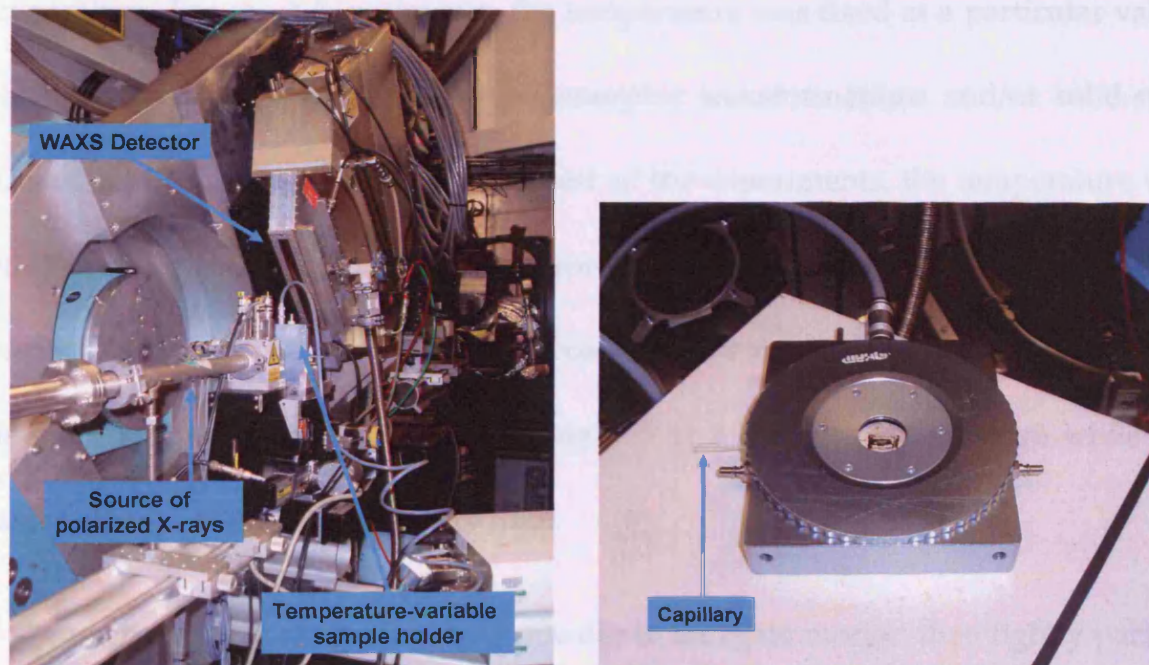


Figure 5.6 Left: experimental set up viewed from another angle. Right: detail of the sampler holder and the relative capillary position.

The sample holder/heating stage (*Figure 5.6*) was connected to a temperature controller unit that was managed remotely. The material in contact with the capillary was ceramic and the rest of the holder was made from aluminium.

For each experiment, the data comprised several frames, with each frame being a PXRD pattern collected generally for 10 or 20 sec. There was a wait time between the frames. The running time and the waiting time were calculated depending on the sample nature, the rates of transformations (to avoid losing information regarding the phase transitions) and the experiment type (to allocate enough time for the solid-state reaction to reach completion at the different temperatures studied). Two different approaches were adopted with regard to temperature. For most experiments, the temperature was fixed at a particular value, which allowed us to monitor the polymorphic transformations and/or solid-state reaction as a function of time. For the rest of the experiments, the temperature was set to ramp at a certain heating rate, reproducing the DSC studies. This chapter is mostly focused on the first type of approach, where the samples were heated up to the exact temperature of study and remained at a constant temperature while the data were collected as a function of time.

Each sample was ground to a powder in an agate mortar, then tightly packed into a 1 mm quartz capillary and finally the capillary was placed in the centre of the sample holder/heating stage. One of the inconveniences of the experimental set-up

was the fact that the capillary was static. This factor contributed to a large extent to the high preferred orientation observed for some ODH polymorphs (discussed later in this chapter).

5.3 – Results

Research at the synchrotron was carried out on the α , γ , δ and ϵ polymorphs. However, this chapter is focussed on the relationship between the α and γ polymorphs and the solid-state reaction. Investigations on the δ and ϵ polymorphs suggesting enantiotropic relationships with the α polymorph and in turn with the γ polymorph will be reported shortly elsewhere [13].

The starting phase for the experiments was the α polymorph of ODH. The sample was heated up rapidly and data were collected as a function of time once the desired temperature was reached. The set temperatures were 186 °C, 188 °C, 190 °C, 192 °C, 194 °C, 196 °C, 198 °C, 200 °C, 202 °C, 204 °C, 207 °C, 210 °C, 213 °C, 216 °C and 220 °C.

The data are shown in density plots where the x axis is the 2θ angle (for $\lambda = 1.4$ Å), the y axis is the time in minutes and the colours represent the intensity of the peaks, with red being the most intense and blue being the least intense. The red threshold is set above either 5 % or 10 % (depending on the dataset) of the maximum

intensity for each dataset. Below the red threshold, the colours are distributed linearly using the RGB colour setting. Each row in the graphs represents 4 or 5 frames added together (depending on dataset) and a baseline was fitted to subtract the background.

Figure 5.7 shows a schematic representation of the characteristic peak positions for the different phases observed in the experiments reported here. The 2θ values for the key peaks of the α polymorph (shown in magenta) are: 14.75° , 21.33° , 22.25° , 23.65° and 25.85° ; those for the γ polymorph (shown in green) are: 10.95° , 13.41° , 16.39° and 20.52° ; and those for DOHH (shown in cyan) are: 12.71° , 13.03° , 18.12° , 20.21° , 23.89° and 24.34° . Only representative peaks for phase identification are shown, avoiding weak peaks, those that overlap with other phases, and those that are excessively close.

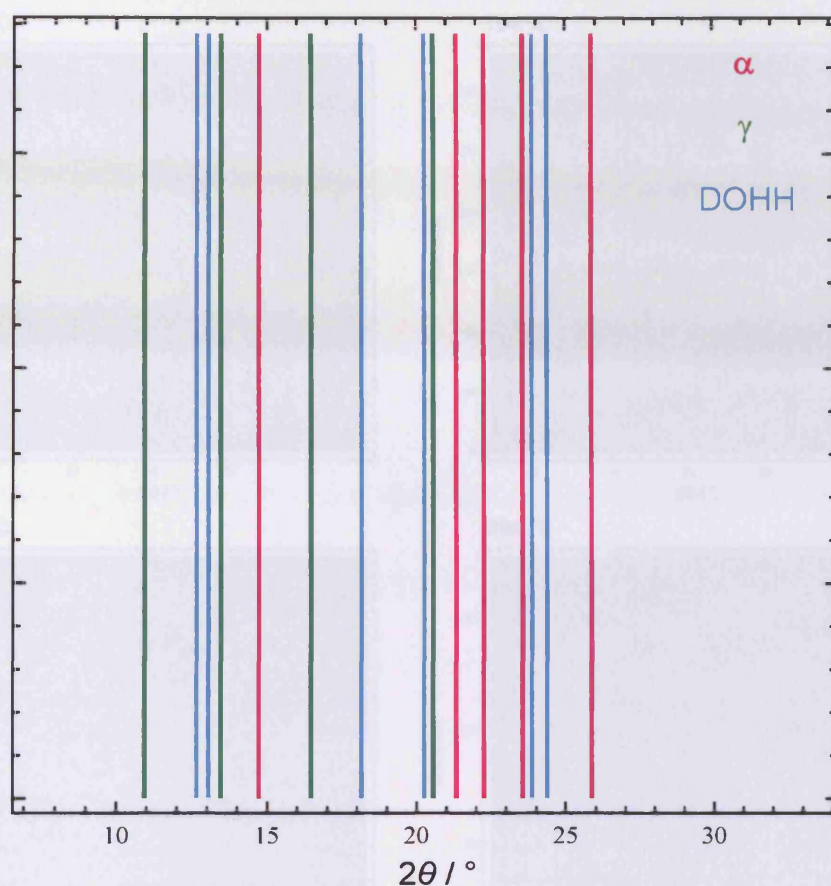


Figure 5.7 Schematic showing the main characteristic peaks for each phase of interest (the α and γ polymorphs of ODH and the reaction product DOHH).

The results of the different experiments are summarized in Figure 5.8. The rest of the dataset graphs can be found in Appendix D. The temperatures selected for the summary are 186 °C, 194 °C, 196 °C, 204 °C, 207 °C and 220 °C. In between the different non-consecutive temperatures (from 186 °C to 194 °C, from 196 °C to 204 °C and from 207 °C to 220 °C), the behaviour of the system was consistent with that observed in the data shown (Figure 5.9).

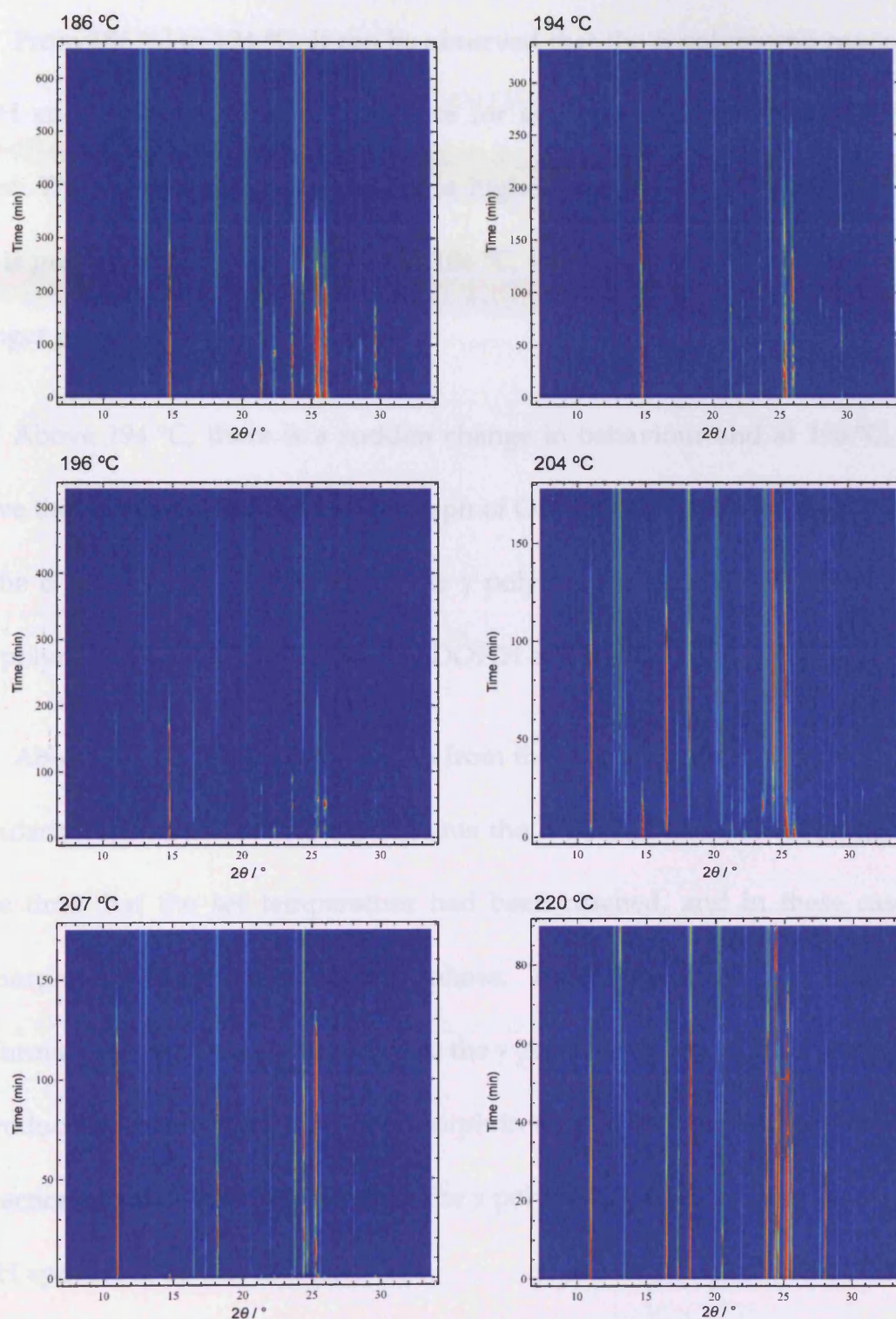


Figure 5.8 Graphs showing the evolution of the α polymorph of ODH, the γ polymorph of ODH and DOHH as a function of time at different temperatures, with intensity represented in different colours (dark blue the least intense and red the most intense)[14].

From 186 °C to 194 °C, it can be observed that the α polymorph reacts to give DOHH and hydrazine without evidence for any other polymorph of ODH being formed. The transformation is quicker at higher temperature. The α polymorph of ODH is present until ca. 450 minutes at 186 °C, whereas at 194 °C the α polymorph is no longer present after ca. 300 minutes.

Above 194 °C, there is a sudden change in behaviour and at 196 °C, we can observe the appearance of the γ polymorph of ODH. From 196 °C to 204 °C, it is clear that the α polymorph transforms to the γ polymorph, and simultaneously both of these polymorphs of ODH react to give DOHH and hydrazine.

Above 207 °C, the transformation from the α polymorph to the γ polymorph is particularly fast, and for most experiments the α polymorph was no longer present by the time that the set temperature had been reached, and in these cases the γ polymorph represents the starting phase. As a result of the high rate of transformation from the α polymorph to the γ polymorph, the DOHH and hydrazine are produced entirely from the γ polymorph in these cases. For higher temperatures, the reaction occurs more rapidly, with the γ polymorph disappearing earlier and the DOHH appearing earlier as well.

It is important to note that the intensity of the peaks due to the α polymorph is highly variable in all the graphs, due to severe preferred orientation. However, for

the γ polymorph, produced as a result of the polymorphic transformation from the α polymorph, this phenomenon was not obvious.

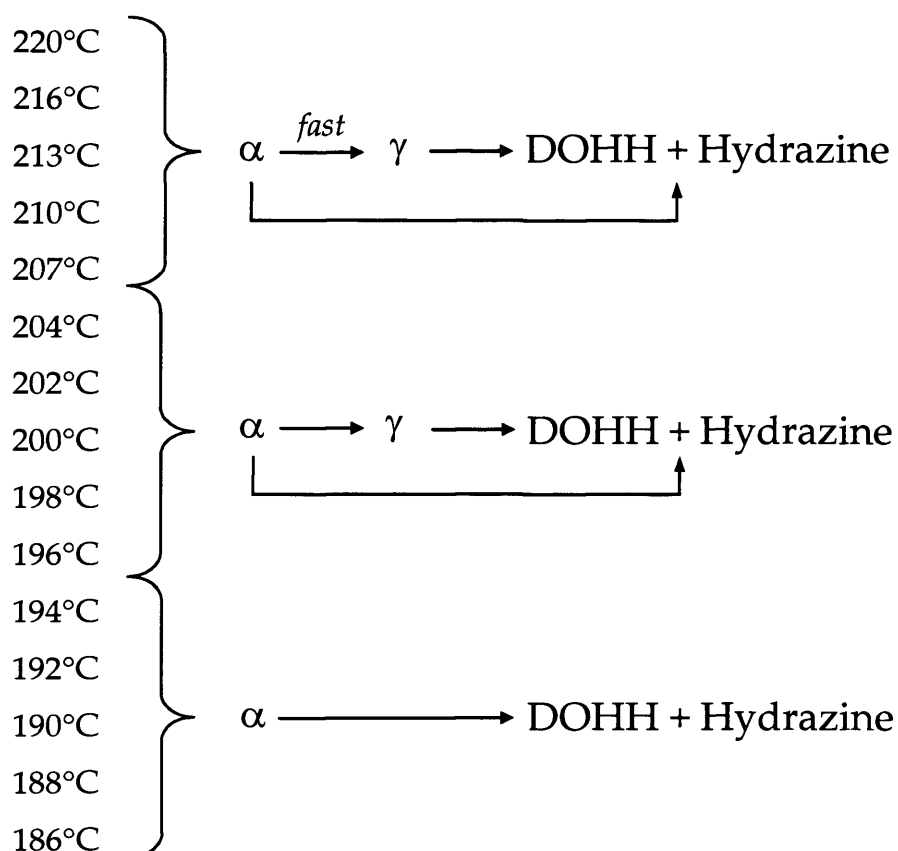


Figure 5.9 Schematic representation of the behaviour of the α polymorph and γ polymorph as a function of temperature.

One interesting aspect of this system at the lower temperatures studied (below 196 °C), is that the intensities of peaks due to DOHH are characterized by an initial increase then decrease (Figure 5.10). The explanation is not straightforward, and further research is necessary to clarify this issue, but several possible causes may be suggested.

(i) Recently, it has been found that the product (analysed by mass spectroscopy) contains molecules of higher mass than DOHH. As the crystalline component in the PXRD pattern of the reaction product is accounted for entirely by the known crystal structure of DOHH, these additional reaction products of higher mass than DOHH must be present in an amorphous component. The formation of amorphous materials within the reaction product is supported by the observation that the background of the PXRD patterns increased with time during the reaction. The initial increase and then decrease in the intensity of peaks due to DOHH could be a consequence of reactions occurring between the DOHH and ODH or any of the longer molecules, which would consume DOHH and would therefore lead to a decrease in the contribution to the PXRD pattern from crystalline DOHH.

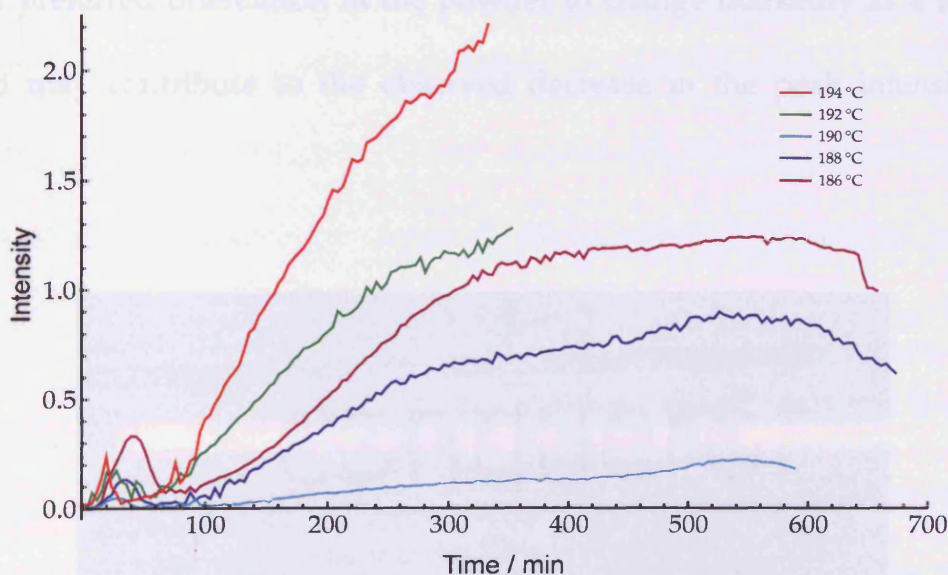


Figure 5.10 Graph showing the initial rise in DOHH intensity at the different temperatures [14].

(ii) Another explanation would be related to the particle size of DOHH, forming big crystals at the beginning of the reaction, with the crystallites diminishing in size (leading to significant peak broadening) at later stages due perhaps to the occurrence of subsequent reactions of DOHH to give products of higher molecular mass.

(iii) The last suggestion is related to a macroscopic physical effect. Due to the difficulty of the gaseous hydrazine to escape from the capillary, it was observed that the powder sample accumulates in an inhomogeneous spatial distribution (non-continuous array of spheres) within the capillary, regardless of the temperature or the starting phase (*Figure 5.11*). Thus far, the consequences of this effect in the PXRD pattern have not been identified, but certainly this effect could cause the degree of preferred orientation in the powder to change markedly as a function of time, and may contribute to the observed decrease in the peak intensity due to DOHH.



Figure 5.11 Capillary after running the experiments, the spheres of powder sample can be observed.

5.4 – Conclusions and Future Work

To recapitulate, below 196 °C, the α polymorph of ODH reacts to give DOHH and hydrazine without undergoing any polymorphic transformation. In the range from 196 °C to 204 °C, the α polymorph transforms to the γ polymorph and contemporaneously reacts to give DOHH and hydrazine; the γ polymorph simultaneously undergoes the solid-state reaction to give DOHH and hydrazine. Above 204 °C, the α polymorph (if at all present when reaching the set temperature) transforms rapidly to the γ polymorph, which in turn reacts to produce DOHH and hydrazine.

Unfortunately, due to strong preferred orientation (in particular for the α polymorph), Rietveld refinement of the data was not viable, therefore no quantitative information could be established on relative amounts of the different solid phases present as a function of time. Further studies with a carefully designed experimental set-up, guided by our previous experiences, would be required to explain and improve the data and elucidate other aspects of the system. Features in the experimental set-up to take into account for development are the following: having a spinning capillary instead of a static one, mounting the sample as a mixture with an amorphous material [relevant with regard to both the preferred orientation issues and reduction of the effect of the gaseous product (see below)] and/or finding

a porous material to construct capillaries which would allow the gaseous product (hydrazine) to escape.

Although it is known that the reaction produces other amorphous by-products, additional investigations (such as solid-state NMR, mass spectroscopy and TGA) are required to ascertain quantitative information on all the products from the reaction. In addition, current research is being carried out to determine whether the solid-state reaction may be reversible, involving a gas-solid reaction between the solid reaction products and gaseous hydrazine.

5.5 – References

- [1] E. Mitscherlich, *Ann. Chim. Phys.*, **19**, 350-419 (1821)
- [2] R. Wille and E. Lutton, *J. Am. Oil Chem. Soc.*, **43**, 491-496 (1966)
- [3] S. Chen, I. A. Guzei and L. Yu, *J. Am. Chem. Soc.*, **127**, 9881-9885 (2005)
- [4] L. Yu, *Acc. Chem. Res.*, DOI: 10.1021/ar100040r (in press)
- [5] F. Quaeyhaegens, H. O. Desseyn, B. Bracke and A. T. H. Lenstra, *J. Mol. Struct.*, **238**, 139-157 (1990)
- [6] S. Y. Ahn, F. Guo, B. M. Kariuki and K. D. M. Harris, *J. Am. Chem. Soc.*, **128**, 8441-8452 (2006)
- [7] F. Guo, PhD Thesis, Cardiff University, 2007
- [8] J. D. Dunitz and J. Bernstein, *Acc. Chem. Res.*, **28**, 193-200 (1995)
- [9] A. Burger and R. Ramberger, *Mikrochimica Acta [Wien]*, **II**, 259-271 (1979)
- [10] A. Burger and R. Ramberger, *Mikrochimica Acta [Wien]*, **II**, 273-316 (1979)
- [11] R. J. Cernik, P. Barnes, G. Bushnell-Wye, A. J. Dent, G. P. Diakun, J. V. Flaherty, G. N. Greaves, E. L. Heeley, W. Helsby, S. D. M. Jacques, J. Kay, T. Rayment, A. Ryan, C. C. Tang and N. J. Terrill, *J. Synchrotron Rad.*, **11**, 163-170 (2004)
- [12] C. C. Tang, C. M. Martin, D. Laundry, S. P. Thompson, G. P. Diakun and R. J. Cernik, *Nucl. Instr. and Meth. in Phys. Res. B*, **222**, 659-666 (2004)
- [13] A. Morte-Ródenas, C. E. Hughes, F. Guo, B. M. Kariuki and K. D. M. Harris, *In preparation*, Mapping the polymorphic phase transformations of oxalyl dihydrazide.
- [14] Graphs made with *Mathematica* by Dr Colan E. Hughes.

Chapter 6

Solid-State Dehydration of *t*-Butylammonium Acetate Monohydrate

6.1 – Introduction

Several different types of structural transformation [1-5] may occur in crystalline organic materials, including solid-state chemical reactions, transformations between polymorphic forms, processes involving solvent exchange, solvation or desolvation among solvate and non-solvate forms, and the formation of new materials by solid-state grinding (mechanochemical synthesis). Clearly, an essential pre-requisite for understanding such transformations is to establish the

details of the structural changes that take place. In favourable cases, transformations in crystalline materials proceed in a single crystal-to-single crystal manner [6-14], such that a single crystal of the parent phase transforms into a single crystal of the product phase. In such cases, single-crystal X-ray diffraction may be exploited to monitor the structural changes associated with the transformation, and in particular to determine the structure of the product phase. However, solid-state transformations often proceed instead with intrinsic loss of single-crystal integrity. In such cases, a single crystal of the parent phase typically yields a microcrystalline powder following the transformation, and structure determination of the product phase by single-crystal X-ray diffraction is not viable. Clearly, an alternative approach is required for structure determination, for example using powder X-ray diffraction, although it is important to recall that the task of carrying out structure determination of organic molecular solids directly from powder X-ray diffraction data [15-19] is significantly more challenging than structure determination from single-crystal X-ray diffraction. However, recent years have seen advances in the opportunities for carrying out structure determination of organic materials directly from powder X-ray diffraction data [20-31], particularly due to the development of the direct-space strategy for structure solution [20]. The emergence of these techniques provides a viable route for structural characterization of polycrystalline product phases produced directly by solid-state transformations of the type

discussed above [32-42]. In the present work, we exploit these techniques (using an implementation of the direct-space genetic algorithm (GA) technique for structure solution [43-47]) to elucidate structural details of a solid-state dehydration process - in particular, dehydration of solid *t*-butylammonium acetate monohydrate – that yields an anhydrous product phase as a microcrystalline powder. As discussed in more detail below, structural interest in materials such as *t*-butylammonium acetate (and solvate phases thereof) is motivated in part by the aim of understanding the resultant crystal packing arrangements in materials for which there is both the opportunity to utilize strong hydrogen-bond donor and strong hydrogen-bond acceptor functionalities in the formation of favourable hydrogen-bonding arrangements and the need to address steric issues arising from the presence of bulky substituents (in this case the *t*-butyl groups).

6.2 – Experimental

Slow evaporation of solvent from a solution prepared by mixing *t*-butylamine (2.744 g) dropwise to dilute aqueous acetic acid (2.255 g of acetic acid in 11.38 g of water) produced a crystalline material which was shown (from single-crystal X-ray diffraction and TGA analysis discussed below) to be a monohydrate phase of *t*-butylammonium acetate. Colourless crystals were formed with typical dimensions ca. $0.5 \times 0.5 \times 1 \text{ mm}^3$. As no other hydrate phase of *t*-butylammonium acetate is

known, we subsequently refer to this material simply as the "hydrate phase". To date, we have been unable to obtain a pure (non-solvate) crystalline phase of *t*-butylammonium acetate by crystallization from solution. However, when the hydrate phase was exposed to the atmosphere at ambient temperature, it was observed (by optical microscopy) to lose single crystal integrity over a period of time of the order of an hour or so, resulting in a microcrystalline powder. Isothermal TGA studies (carried out at 24 °C) starting from the hydrate phase confirm that this transformation corresponds to the complete loss of water (after ca. 30 min at 24 °C), (measured percentage mass loss, 11.88 %; percentage mass of water in the hydrate phase, 11.92 %). Powder X-ray diffraction (*Figure 6.1*) confirmed that the product was a new crystalline phase, with no detectable amounts of the parent hydrate phase present.

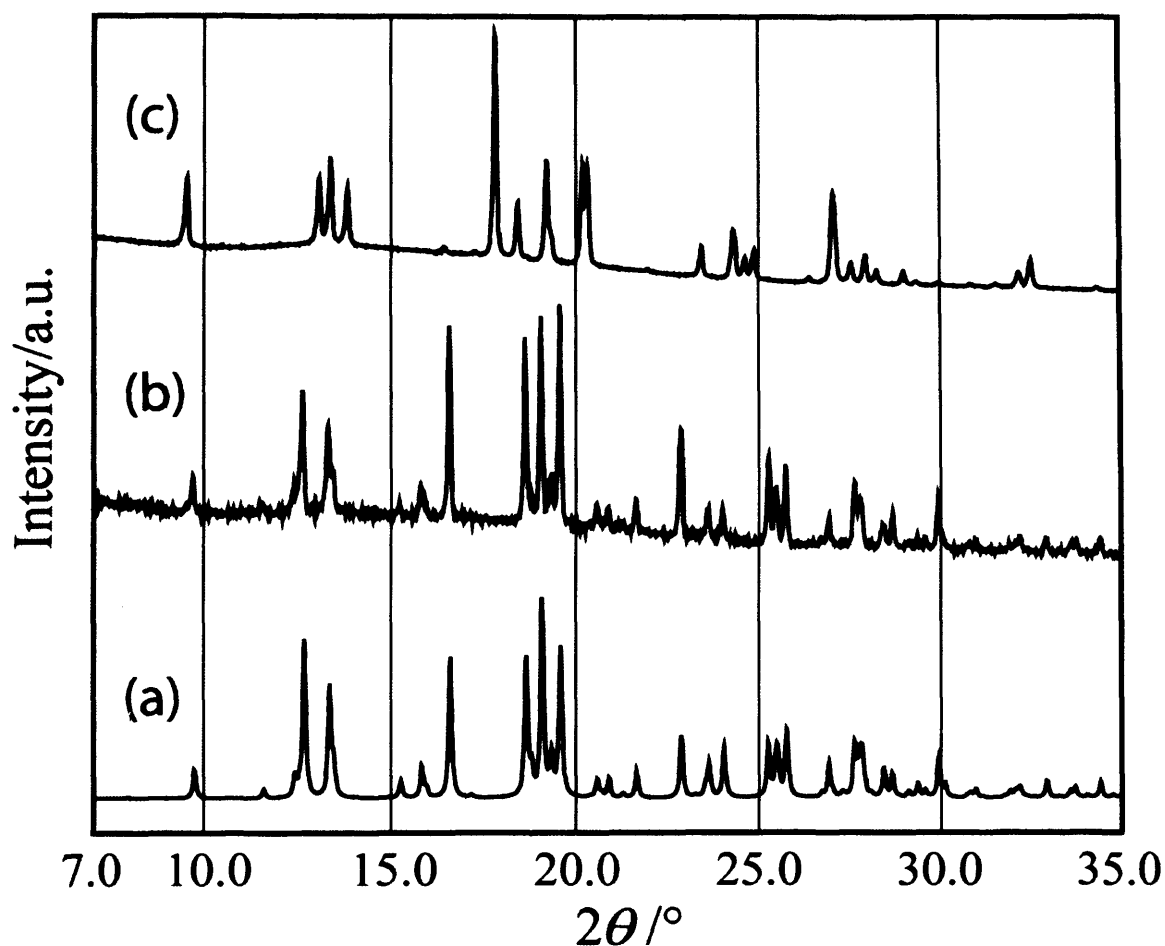


Figure 6.1 Comparison of powder X-ray diffraction patterns of (a) the hydrate phase (simulated from the crystal structure determined from single-crystal X-ray diffraction; see below), (b) hydrate phase (experimental), and (c) anhydrous phase (experimental; obtained by dehydration of the hydrate phase). Note that, due to the susceptibility of the hydrate phase to dehydration, the powder X-ray diffraction pattern for the hydrate phase in (b) was recorded over a relatively short time, and hence the signal/noise ratio is comparatively poor.

6.3 – Structure Determination

Crystal structure determination of the hydrate phase, which has not been reported previously, was carried out from single-crystal X-ray diffraction data collected on a Nonius Kappa CCD diffractometer at ambient temperature using monochromated MoK α radiation ($\lambda = 0.71073 \text{ \AA}$). Although an exposed sample of the hydrate phase undergoes dehydration over a period of an hour or so at ambient temperature, it was possible to collect single-crystal X-ray diffraction data sufficiently quickly for a crystal protected by a coating of inert oil such that the data were not significantly degraded. The crystal structure was solved and refined ($R1 = 0.0712$, $wR2 = 0.1570$ [$I > 2 \sigma(I)$]) using SHELX97 [48]. Refinement of non-hydrogen atoms was carried out with anisotropic displacement parameters. The positions of all hydrogen atoms in the hydrogen-bonding arrangement were revealed by difference Fourier analysis. The CH₃ and NH₃ groups were subsequently refined with idealized geometry, and the isotropic displacement parameter for each hydrogen atom was taken as 1.5 times the equivalent isotropic displacement parameter of the atom to which it is bonded. Water molecules were refined with O–H distances loosely restrained and the isotropic displacement parameter of each hydrogen atom was taken as 1.2 times the equivalent isotropic displacement parameter of the O atom to which it is bonded.

The crystal structure of the hydrate phase (*Figure 6.2*) is monoclinic with space group $P2_1/n$ [$a = 7.6306(15)$ Å, $b = 18.094(4)$ Å, $c = 14.236(3)$ Å, $\beta = 98.57(3)$; $V = 1943.65$ Å³; calculated density, 1.033 g cm⁻³] (See Appendix E for extended crystallographic data). The powder X-ray diffraction pattern simulated from this crystal structure is shown in *Figure 6.1a*. The good agreement between the simulated powder X-ray diffraction pattern for this structure (*Figure 6.1a*) and the experimental powder X-ray diffraction pattern for the bulk polycrystalline sample of the hydrate phase (*Figure 6.1b*) confirms that the structure of the hydrate phase determined from single-crystal X-ray diffraction data is fully representative of the bulk polycrystalline sample.

Structure determination of the anhydrous phase of *t*-butylammonium acetate was carried out directly from powder X-ray diffraction data. The material used for this structure determination was prepared by leaving several single crystals of the hydrate phase overnight in an oven at 25 °C (when the hydrate phase was left for a period of time at higher temperature (40 °C), sublimation was observed to occur). For structure determination of the anhydrous phase, high-quality powder X-ray diffraction data were recorded on a Bruker D8 diffractometer (See section 2.2.4 for more details on the instrument) at ambient temperature, with 2θ range 3.5° – 60°, step size 0.017°, and data collection time 12 hours.

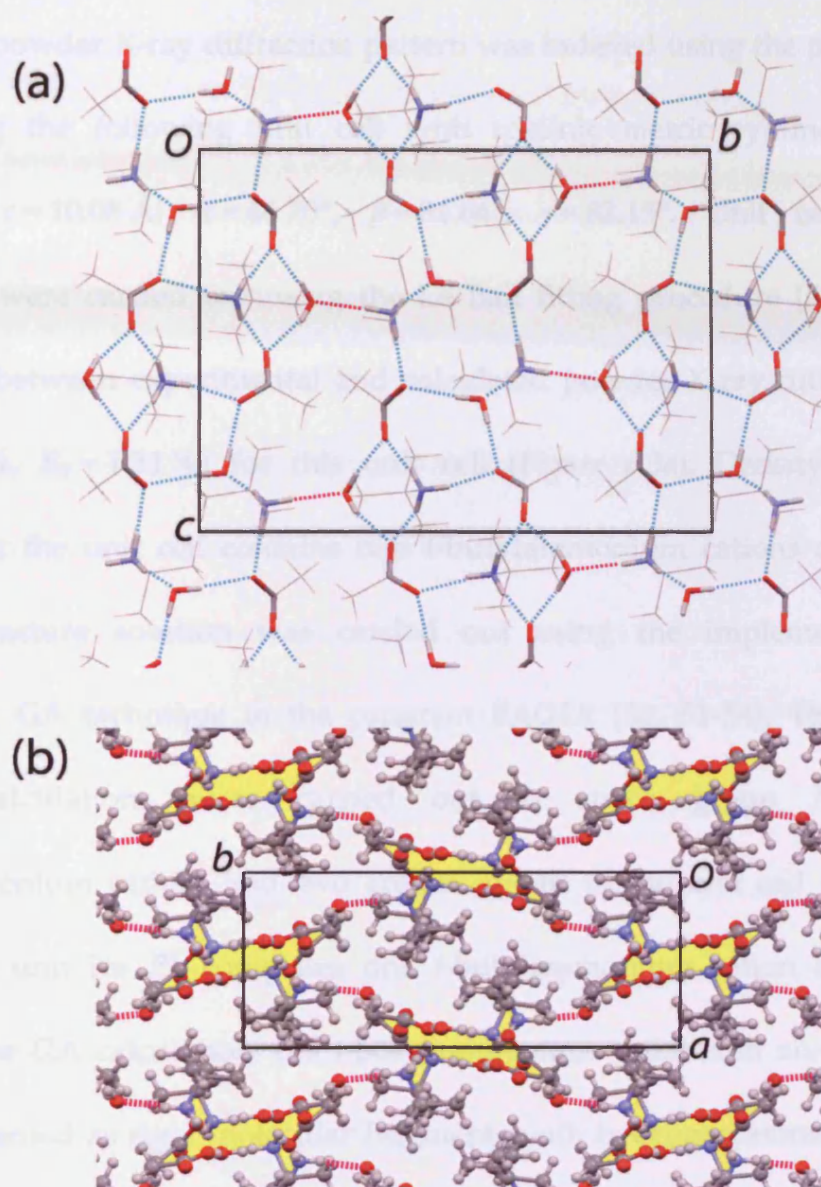


Figure 6.2 Crystal structure of the hydrate phase viewed (a) along the *a*-axis and (b) along the *c*-axis. Hydrogen bonds are indicated by dotted lines (blue dotted lines connect molecules within a given hydrogen-bonded ribbon, whereas red dotted lines connect adjacent ribbons). In (a), the groups engaged in hydrogen bonding are drawn with thicker bonds in order to highlight the hydrogen-bonding scheme. In (b), the ribbons are indicated by yellow shading, and red dotted lines represent hydrogen bonds between adjacent ribbons.

The powder X-ray diffraction pattern was indexed using the program TREOR [49], giving the following unit cell with triclinic metric symmetry: $a = 6.43 \text{ \AA}$, $b = 7.19 \text{ \AA}$, $c = 10.05 \text{ \AA}$, $\alpha = 66.70^\circ$, $\beta = 84.64^\circ$, $\gamma = 83.15^\circ$. Unit cell and profile refinement were carried out using the Le Bail fitting procedure [50], giving good agreement between experimental and calculated powder X-ray diffraction profiles ($R_{wp} = 1.80 \%$, $R_p = 1.31 \%$) for this unit cell (Figure 6.3a). Density considerations suggest that the unit cell contains two *t*-butylammonium cations and two acetate anions. Structure solution was carried out using the implementation of the direct-space GA technique in the program EAGER [32, 51-54]. The GA structure solution calculations were carried out in space group $P\bar{1}$. With two *t*-butylammonium cations and two acetate anions in the unit cell (see above), the asymmetric unit for $P\bar{1}$ comprises one *t*-butylammonium cation and one acetate anion. In the GA calculation, the *t*-butylammonium cation and acetate anion were each represented as rigid molecular fragments with hydrogen atoms omitted. Thus, the total number of structural variables involved in the direct-space search was 12, comprising three translational variables $\{x, y, z\}$ and three orientational variables $\{\theta, \phi, \psi\}$ for each fragment. The GA calculation was carried out for 50 generations, with a population size of 100 structures and with 25 mating operations and 10 mutation operations carried out in each generation. The best structure solution (i.e. the structure of lowest R_{wp} generated in the GA calculation) was used as the

starting structural model for Rietveld refinement [55-57], which was carried out using the GSAS program [58]. In the Rietveld refinement, standard geometric restraints were applied to bond lengths and bond angles (with the lengths of the two C–O bonds of the acetate anion restrained to be equal), and the restraints were relaxed gradually as the refinement progressed. The atomic positions were refined, together with a common isotropic displacement parameter for each molecular fragment. In the later stages of the refinement, hydrogen atoms were added to the structural model in positions corresponding to standard molecular geometries. For the NH_3^+ group of the *t*-butylammonium cation, the positions of the hydrogen atoms corresponded to geometrically reasonable N–H \cdots O hydrogen bonds, as discussed in more detail below. The isotropic displacement parameter for each hydrogen atom was taken as 1.5 times that of the atom to which it is bonded. The final Rietveld refinement (*Figure 6.3b*) gave good agreement between calculated and experimental powder X-ray diffraction patterns ($R_{\text{wp}} = 2.07\%$, $R_{\text{p}} = 1.47\%$), with the following refined parameters: $a = 6.42596(15) \text{ \AA}$, $b = 7.19411(17) \text{ \AA}$, $c = 10.04415(26) \text{ \AA}$, $\alpha = 66.6999(13)^\circ$, $\beta = 84.6295(15)^\circ$, $\gamma = 83.1542(10)^\circ$; $V = 422.873(23) \text{ \AA}^3$; calculated density, 1.046 g cm^{-3} (2θ range, $7.69\text{--}59.93^\circ$; 3129 profile points; 119 refined variables). The crystal structure is shown in *Figure 6.4*.

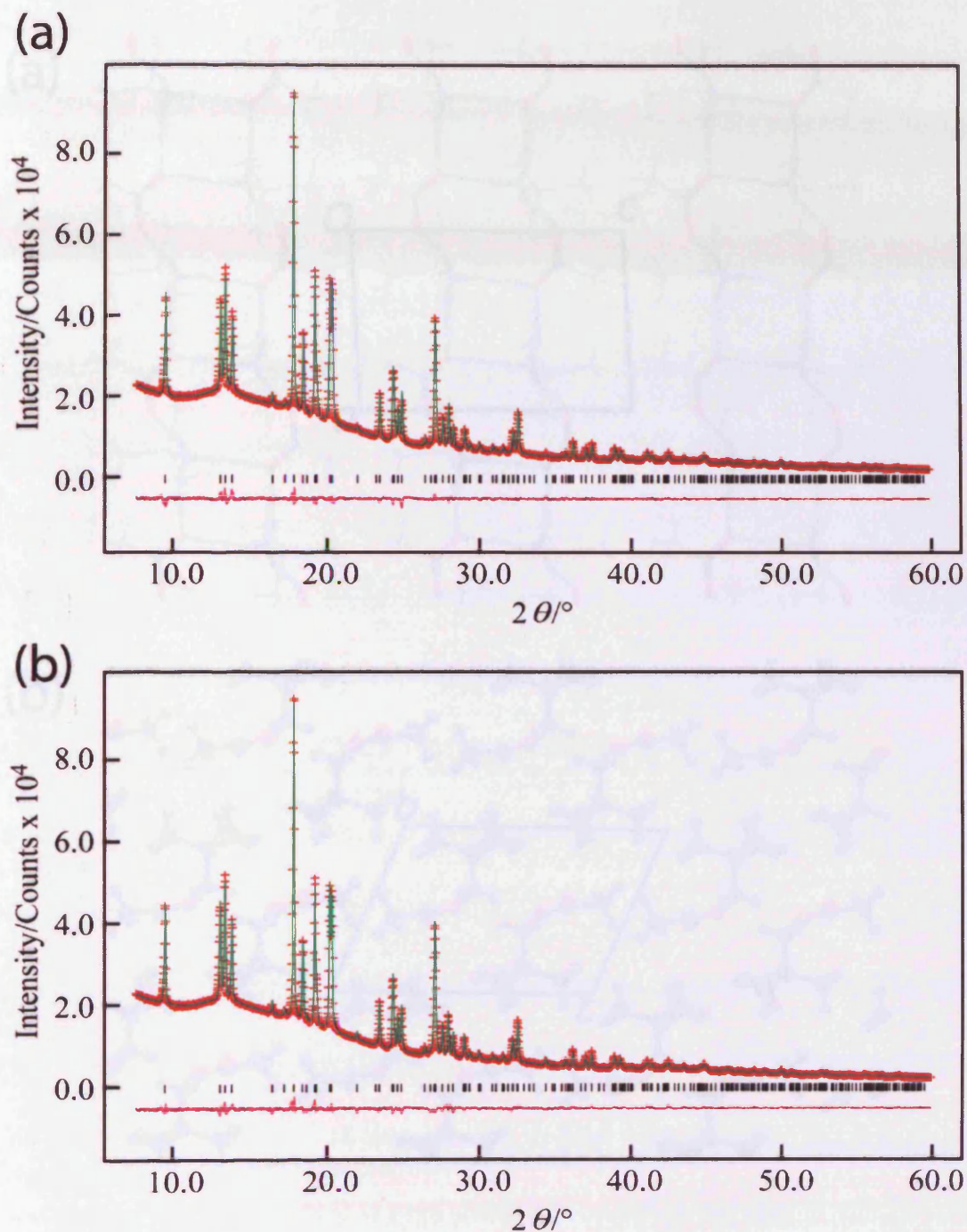


Figure 6.3 Results from (a) Le Bail fitting and (b) Rietveld refinement for the anhydrous phase. In each case, the plot shows the experimental (+), calculated (—) and difference (bottom) powder X-ray diffraction profiles. Reflection positions are marked.

6.4 – Results and Discussion

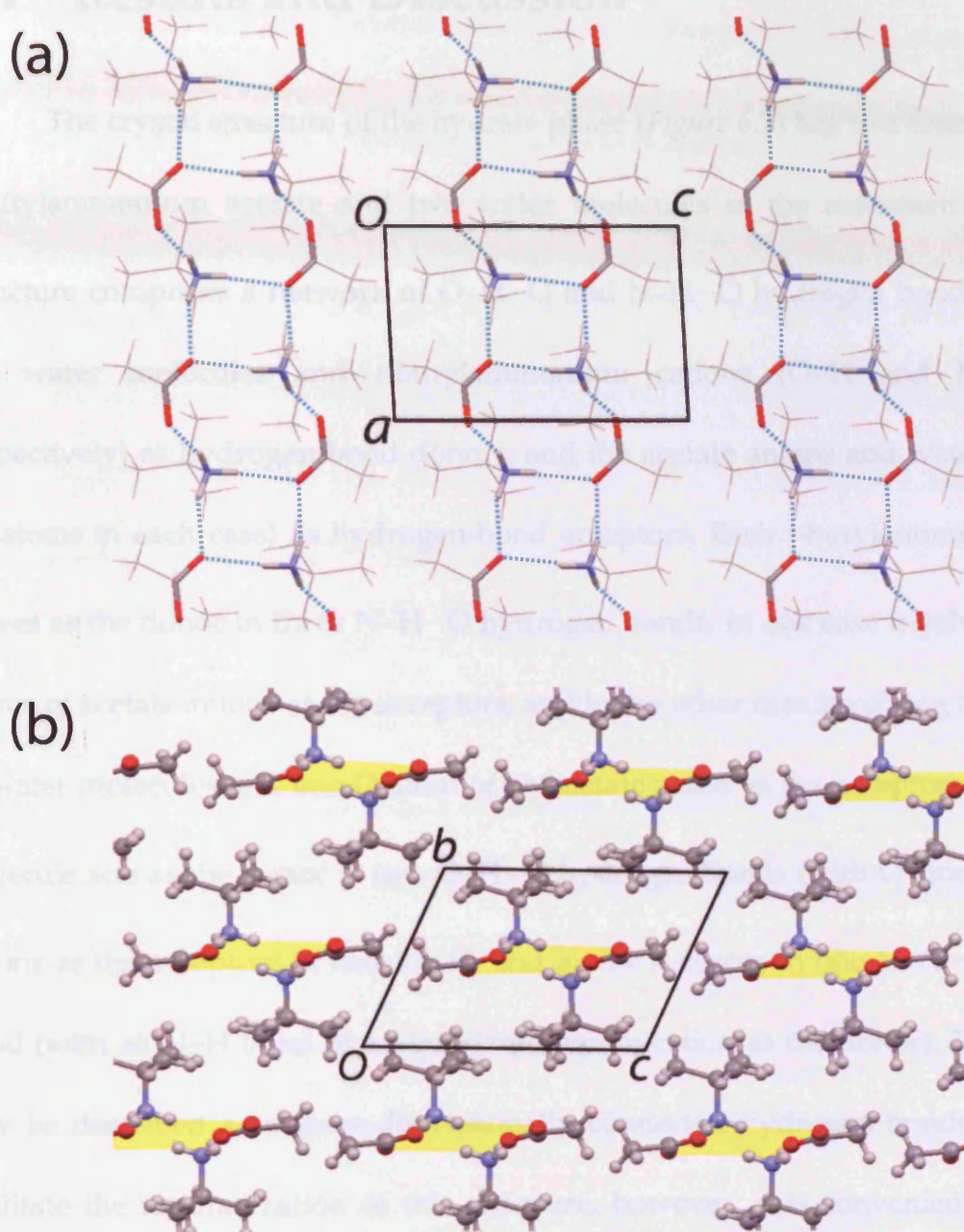


Figure 6.4 Crystal structure of the anhydrous phase viewed (a) along the *b*-axis and (b) along the *a*-axis. In (a), the groups engaged in hydrogen bonding are drawn with thicker bonds, and hydrogen bonds are indicated by blue dotted lines. In (b), the ribbons are indicated by yellow shading.

6.4 – Results and Discussion

The crystal structure of the hydrate phase (*Figure 6.2*) has two formula units of *t*-butylammonium acetate and two water molecules in the asymmetric unit. The structure comprises a network of O–H...O and N–H...O hydrogen bonds, involving the water molecules and *t*-butylammonium cations (O–H and N–H bonds respectively) as hydrogen-bond donors, and the acetate anions and water molecules (O atoms in each case) as hydrogen-bond acceptors. Each *t*-butylammonium cation serves as the donor in three N–H...O hydrogen bonds, in one case involving three O atoms of acetate anions as the acceptors, and in the other case involving two O atoms of water molecules and one O atom of an acetate anion as the acceptors. Each water molecule acts as the donor in two O–H...O hydrogen bonds (with O atoms of acetate anions as the acceptors in each case), and as the acceptor in one N–H...O hydrogen bond (with an N–H bond of a *t*-butylammonium cation as the donor). The structure may be described as a three-dimensionally connected hydrogen bonded array. To facilitate the rationalization of this structure, however, it is convenient to identify ribbon-like hydrogen-bonded arrays that run parallel to the *c*-axis (vertical in *Figure 6.2a*). As shown in *Figure 6.5a*, these ribbons are constructed from four different types of cyclic hydrogen-bonded array (each involving four hydrogen bonds), described in graph set notation [59-61] as follows: (i) $R_4^4(12)$

[a centrosymmetric array, labelled (i) in *Figure 6.5a*, involving two *t*-butylammonium cations and two acetate anions], (ii) $R_4^3(10)$ [labelled (ii) in *Figure 6.5a*, involving one *t*-butylammonium cation and one water molecule as donors (utilizing two N–H bonds and two O–H bonds respectively) and three O atoms of acetate anions as acceptors], (iii) $R_4^2(8)$ [labelled (iii) in *Figure 6.5a*, involving one *t*-butylammonium cation and one water molecule as donors (utilizing two N–H bonds and two O–H bonds respectively) and two O atoms of acetate anions as acceptors], and (iv) $R_6^4(12)$ [a centrosymmetric array, labelled (iv) in *Figure 6.5a*, involving two *t*-butylammonium cations and two water molecules as donors (each utilizing two N–H bonds and one O–H bonds respectively) and two O atoms of acetate anions and two O atoms of water molecules as acceptors]. We note that the $R_4^4(12)$ array (which is the only cyclic array that does not involve water molecules) is retained [we note that, in many other cases of dehydration processes in molecular crystals, the hydrogen bonding arrangement in the anhydrous product phase does not retain any common features with the hydrogen bonding arrangement in the parent hydrate phase] in the structure of the anhydrous phase discussed below. Each of these hydrogen-bonded ribbons is engaged in further hydrogen bonding (indicated by red dashed lines in *Figure 6.5a*) to adjacent ribbons lying in planes above and below, giving rise to a three-dimensionally connected hydrogen bonding network. When viewed along the *c*-axis (i.e. the direction of propagation of the ribbons; *Figure 6.2b*),

it is evident that this three-dimensional hydrogen-bonded network has a channel-like topology (the channels are parallel to the *c*-axis), with the *t*-butyl groups of the *t*-butylammonium cations accommodated within the channel-like region.

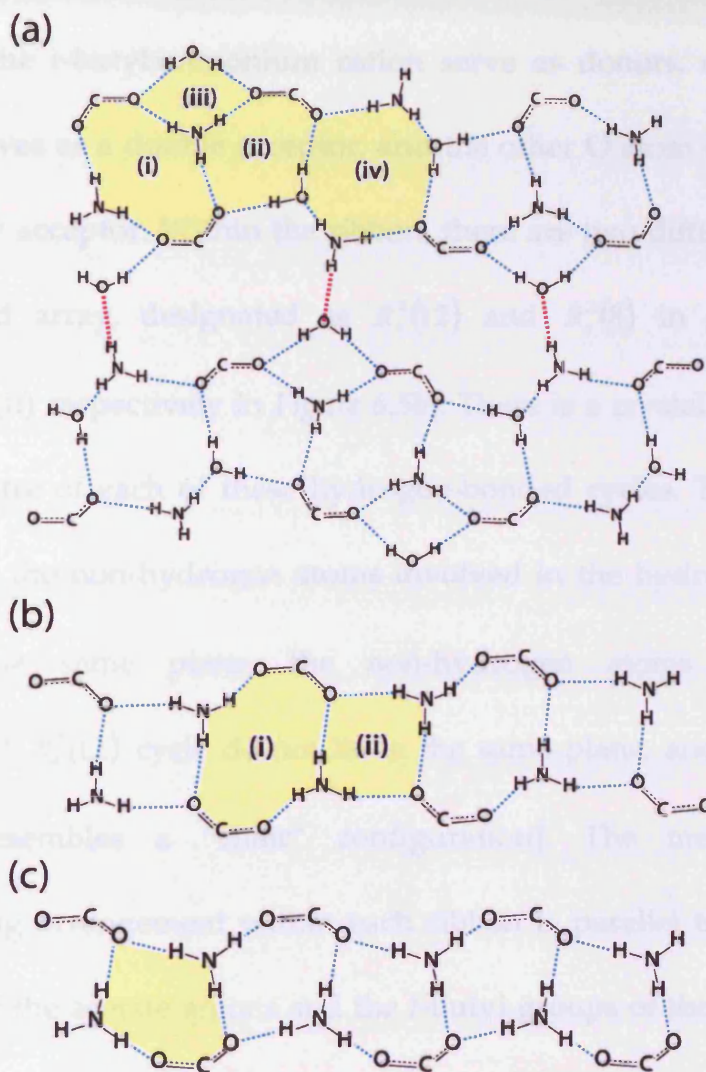


Figure 6.5 Schematic illustrations of (a) the hydrogen-bonding scheme in the hydrate phase, (b) the hydrogen-bonding scheme in the anhydrous phase, and (c) a hydrogen-bonding scheme commonly observed in other *t*-butylammonium carboxylate materials. The hydrogen-bonded cycles shaded in yellow are discussed in the text.

The crystal structure of the anhydrous phase (*Figure 6.4*) has one *t*-butylammonium cation and one acetate anion in the asymmetric unit. Hydrogen-bonded ribbons (*Figure 6.5b*) propagate along the *a*-axis, and are constructed from three independent types of N–H...O hydrogen bonds. All three N–H bonds of the *t*-butylammonium cation serve as donors, one O atom of the acetate anion serves as a double acceptor, and the other O atom of the acetate anion serves as a single acceptor. Within the ribbon, there are two different types of cyclic hydrogen-bonded array, designated as $R_4^4(12)$ and $R_4^2(8)$ in graph set notation [labelled (i) and (ii) respectively in *Figure 6.5b*]. There is a crystallographic inversion centre at the centre of each of these hydrogen-bonded cycles. The ribbons are not planar [although the non-hydrogen atoms involved in the hydrogen-bonded $R_4^2(8)$ cycle lie in the same plane, the non-hydrogen atoms involved in the hydrogen-bonded $R_4^4(12)$ cycle do not lie in the same plane, and are arranged in a manner that resembles a “chair” configuration]. The mean plane of the hydrogen-bonding arrangement within each ribbon is parallel to the *ac*-plane. The methyl groups of the acetate anions and the *t*-butyl groups of the *t*-butylammonium cations project from the periphery of the ribbons (the methyl groups of the acetate anions are located approximately in the same plane as the hydrogen-bonding arrangement, whereas the *t*-butyl groups project above and below this plane). As shown in *Figure 6.4b* (in which the structure is viewed parallel to the direction of

propagation of the ribbons), each ribbon is surrounded by six others. However, in contrast to the situation observed for the hydrate phase, there is no hydrogen bonding between adjacent ribbons in the structure of the anhydrous phase. Instead, adjacent ribbons in the anhydrous phase interact only via van der Waals interactions involving the methyl and *t*-butyl groups.

As noted above, the $R_4^4(12)$ hydrogen-bonded array in the structure of the anhydrous phase is also present in the structure of the hydrate phase, and it is conceivable that the integrity of this array is retained during the dehydration process. Nevertheless, the dehydration process is associated with significant changes to the overall hydrogen-bonding arrangement. In particular, as the water molecules are an integral part of the hydrogen-bonding arrangement in the hydrate phase, serving as both donors and acceptors, the loss of the water molecules in the dehydration process must inevitably disrupt the hydrogen-bonding, even though the hydrogen-bonding connectivity involving one of the two independent *t*-butylammonium cations and one of the two independent acetate anions might remain intact during the transformation.

It is relevant to compare the structures reported here with those of other *t*-butylammonium carboxylate materials (including hydrate and solvate phases). Of the structures within this class reported in the Cambridge Structural Database (CSD Version 5.31, November 2009), one structure (*t*-butylammonium sorbate [62]) has an

identical hydrogen-bonding arrangement to that reported here for the anhydrous phase of *t*-butylammonium acetate, comprising hydrogen-bonded ribbons with an alternation of $R_4^4(12)$ and $R_4^2(8)$ hydrogen-bonded cycles. No other structure within this class has a hydrogen-bonding scheme that approaches the complexity of that observed here for the hydrate phase of *t*-butylammonium acetate. However, the structure of one reported hydrate {tetrakis(*t*-butylammonium) benzene-1,2,4,5-tetracarboxylate octahydrate [63]} does contain a hydrogen-bonded $R_4^3(10)$ cycle analogous to that observed within the hydrogen-bonding scheme of *t*-butylammonium acetate hydrate (see above).

Among the structures of anhydrous *t*-butylammonium carboxylate materials, however, the most common type of hydrogen-bonded ribbon [64-66] is one constructed entirely from $R_4^3(10)$ hydrogen-bonded cycles, involving two *t*-butylammonium cations as donors (each utilizing two N–H bonds within the hydrogen-bonded cycle) and three O atoms of acetate anions as acceptors (with one O atom acting as the acceptor to two N–H...O hydrogen bonds)]. This hydrogen-bonded cycle is analogous to the $R_4^3(10)$ array observed in the hydrate phase of *t*-butylammonium acetate, but with the two O–H donors of the water molecule replaced by two N–H donors from a *t*-butylammonium cation (*Figure 6.5c*). In addition to the structures based on hydrogen-bonded ribbons, as discussed above, structures of *t*-butylammonium carboxylate materials comprising cage-like

hydrogen-bonding arrangements, which serve as the host in solid inclusion compounds, have also been reported [67, 68].

Clearly, a more detailed rationalization of the preferred modes of molecular aggregation of *t*-butylammonium carboxylate materials will rely on the application of appropriate computational techniques. Such computational studies would constitute an interesting subject for future research, particularly with a view to establishing a more quantitative understanding of the relative importance of optimizing the hydrogen-bonding arrangement vis-à-vis optimizing the steric effects due to the presence of the bulky *t*-butyl groups in this family of materials.

6.5 – References

- [1] J. M. Thomas, *Phil. Trans. Roy. Soc.*, **277**, 251-286 (1974)
- [2] J. D. Dunitz, *Acta Cryst. Sect. B*, **51**, 619-631 (1995)
- [3] J. Bernstein, "Polymorphism in Molecular Crystals", Oxford University Press, Oxford, (2002)
- [4] D. Braga and F. Grepioni, *Chem. Commun.*, 3635-3645 (2005)
- [5] F. H. Herbstein, *Acta Crystallogr., Sect. B*, **62**, 341-383 (2006)
- [6] H. Nakanishi, W. Jones and J. M. Thomas, *Chem. Phys. Lett.*, **71**, 44-48 (1980)
- [7] H. Nakanishi, W. Jones, J. M. Thomas, M. B. Hursthouse and M. Motevalli, *J. Phys. Chem.*, **85**, 3636-3642 (1981)
- [8] V. Enkelmann, G. Wegner, K. Novak and K. B. Wagener, *J. Am. Chem. Soc.*, **115**, 10390-10391 (1993)
- [9] S. Ohba and Y. Ito, *Acta Cryst. Sect. B*, **59**, 149-155 (2003)
- [10] Q. L. Chu, D. C. Swenson and L. R. MacGillivray, *Angew. Chem. Int. Ed.*, **44**, 3569-3572 (2005)
- [11] T. Friscic and L. R. MacGillivray, *Z. Kristallogr.*, **220**, 351-363 (2005)
- [12] H. Koshima, H. Kawanishi, M. Nagano, H. T. Yu, M. Shiro, T. Hosoya, H. Uekusa and Y. Ohashi, *J. Org. Chem.*, **70**, 4490-4497 (2005)
- [13] J. B. Benedict and P. Coppens, *J. Phys. Chem. A*, **113**, 3116-3120 (2009)
- [14] M. H. Mir, L. L. Koh, G. K. Tan and J. J. Vittal, *Angew. Chem. Int. Ed.*, **49**, 390-393 (2010)
- [15] W. I. F. David, K. Shankland, L. B. McCusker and C. Baerlocher, *Structure Determination from Powder Diffraction Data*, OUP/IUCr (2002)
- [16] K. D. M. Harris, *Cryst. Growth Des.*, **3**, 887-895 (2003)
- [17] K. D. M. Harris and E. Y. Cheung, *Chem. Soc. Rev.*, **33**, 526-538 (2004)

- [18] M. Tremayne, *Phil. Trans. Roy. Soc.*, **362**, 2691-2707 (2004)
- [19] R. Černý, *Croat. Chem. Acta*, **79**, 319-326 (2006)
- [20] K. D. M. Harris, M. Tremayne, P. Lightfoot and P. G. Bruce, *J. Am. Chem. Soc.*, **116**, 3543-3547 (1994)
- [21] V. V. Chernyshev, *Russ. Chem. Bull.*, **50**, 2273-2292 (2001)
- [22] P. Lightfoot, M. Tremayne, K. D. M. Harris and P. G. Bruce, *J. Chem. Soc., Chem. Commun.*, 1012-1016 (1992)
- [23] B. M. Kariuki, D. M. S. Zin, M. Tremayne and K. D. M. Harris, *Chem. Mater.*, **8**, 565-569 (1996)
- [24] W. I. F. David, K. Shankland and N. Shankland, *Chem. Comm.*, 931-932 (1998)
- [25] A. Huq and P. W. Stephens, *J. Pharm. Sci.*, **92**, 244-249 (2003)
- [26] M. Brunelli, J. P. Wright, G. R. M. Vaughan, A. J. Mora and A. N. Fitch, *Angew. Chem. Int. Ed.*, **42**, 2029-2032 (2003)
- [27] V. Favre-Nicolin and R. Černý, *Z. Kristallogr.*, **219**, 847-856 (2004)
- [28] V. Brodski, R. Peschar and H. Schenk, *J. Appl. Cryst.*, **38**, 688-693 (2005)
- [29] H. Tsue, M. Horiguchi, R. Tamura, K. Fujii and H. Uekusa, *J. Synth. Org. Chem. Jpn.*, **65**, 1203-1212 (2007)
- [30] W. I. F. David and K. Shankland, *Acta Cryst. Sect. A*, **64**, 52-64 (2008)
- [31] A. Altomare, R. Caliendo, C. Cuocci, C. Giacovazzo, A. G. G. Moliterni, R. Rizzi and C. Platteau, *J. Appl. Cryst.*, **41**, 56-61 (2008)
- [32] E. Y. Cheung, S. J. Kitchin, K. D. M. Harris, Y. Imai, N. Tajima and R. Kuroda, *J. Am. Chem. Soc.*, **125**, 14658-14659 (2003)
- [33] A. J. Mora, E. E. Avila, G. E. Delgado, A. N. Fitch and M. Brunelli, *Acta Cryst. Sect. B*, **61**, 96-102 (2005)
- [34] C. Platteau, J. Lefebvre, F. Affouard, J. F. Willart, P. Derollez and F. Mallet, *Acta Cryst. Sect. B*, **61**, 185-191 (2005)
- [35] F. Guo and K. D. M. Harris, *J. Am. Chem. Soc.*, **127**, 7314-7315 (2005)

- [36] S. Hirano, S. Toyota, F. Toda, K. Fujii and H. Uekusa, *Angew. Chem. Int. Ed.*, **45**, 6013-6016 (2005)
- [37] C. Guguta, H. Meekes and R. Gelder, *Cryst. Growth Des.*, **6**, 2686-2692 (2006)
- [38] D. Albesa-Jové, Z. Pan, K. D. M. Harris and H. Uekusa, *Cryst. Growth Des.*, **8**, 3641-3645 (2008)
- [39] F. Guo, J. Martí-Rujas, Z. Pan, C. E. Hughes and K. D. M. Harris, *J. Phys. Chem. C*, **112**, 19793-19796 (2008)
- [40] G. Hasegawa, T. Komasa, R. Bando, Y. Yoshihashi, E. Yonemochi, K. Fujii, H. Uekusa and K. Terada, *Int. J. Pharm.*, **369**, 12-18 (2009)
- [41] K. Fujii, Y. Ashida, H. Uekusa, S. Hirano, S. Toyota, F. Toda, Z. Pan and K. D. M. Harris, *Cryst. Growth Des.*, **9**, 1201-1207 (2009)
- [42] K. Fujii, H. Uekusa, N. Itoda, G. Hasegawa, E. Yonemochi, K. Terada, Z. Pan and K. D. M. Harris, *J. Phys. Chem. C*, **114**, 580-586 (2010)
- [43] B. M. Kariuki, H. Serrano-González, R. L. Johnston and K. D. M. Harris, *Chem. Phys. Lett.*, **280**, 189-195 (1997)
- [44] K. D. M. Harris, R. L. Johnston and B. M. Kariuki, *Acta Cryst. Sect. A*, **54**, 632-645 (1998)
- [45] G. W. Turner, E. Tedesco, K. D. M. Harris, R. L. Johnston and B. M. Kariuki, *Chem. Phys. Lett.*, **321**, 183-190 (2000)
- [46] S. Habershon, K. D. M. Harris and R. L. Johnston, *J. Comput. Chem.*, **24**, 1766-1774 (2003)
- [47] K. D. M. Harris, S. Habershon, E. Y. Cheung and R. L. Johnston, *Z. Kristallogr.*, **219**, 838-846 (2004)
- [48] G. M. Sheldrick, *Acta Cryst. Sect. A*, **64**, 112-122 (2008)
- [49] P. E. Werner, L. Eriksson and M. Westdahl, *J. Appl. Cryst.*, **18**, 367-370 (1985)
- [50] A. Le Bail, H. Duroy and J. L. Fourquet, *Mater. Res. Bull.*, **23**, 447-452 (1988)
- [51] E. Tedesco, G. W. Turner, K. D. M. Harris, R. L. Johnston and B. M. Kariuki, *Angew. Chem. Int. Ed.*, **39**, 4488-4491 (2000)

- [52] E. Tedesco, F. Della Sala, L. Favaretto, G. Barbarella, D. Albesa-Jové, D. Pisignano, G. Gigli, R. Cingolani and K. D. M. Harris, *J. Am. Chem. Soc.*, **125**, 12277-12283 (2003)
- [53] D. Albesa-Jové, B. M. Kariuki, S. J. Kitchin, L. Grice, E. Y. Cheung and K. D. M. Harris, *ChemPhysChem*, **5**, 414-148 (2004)
- [54] Z. Pan, M. Xu, E. Y. Cheung, K. D. M. Harris, E. C. Constable and C. E. Housecroft, *J. Phys. Chem. B*, **110**, 11620-11623 (2006)
- [55] H. M. Rietveld, *J. Appl. Cryst.*, **2**, 65-71 (1969)
- [56] R. A. Young, "The Rietveld Method", International Union of Crystallography, (1993)
- [57] L. B. McCusker, R. B. Von Dreele, D. E. Cox, D. Louër and P. Scardi, *J. Appl. Cryst.*, **32**, 36-50 (1999)
- [58] A. C. Larson and R. B. Von Dreele, GSAS, Los Alamos Laboratory Report No. LA-UR-86-748 (1987)
- [59] M. C. Etter, *Acc. Chem. Res.*, **23**, 120-126 (1990)
- [60] M. C. Etter, J. C. MacDonald and J. Bernstein, *Acta Cryst. Sect. B*, **46**, 256-262 (1990)
- [61] J. Bernstein, R. E. Davis, L. Shimoni and N. L. Chang, *Angew. Chem. Int. Ed.*, **34**, 1555-1573 (1995)
- [62] S. Nagahama, K. Inoue, K. Sada, M. Miyata and A. Matsumoto, *Cryst. Growth Des.*, **3**, 247-256 (2003)
- [63] K. Ejsmont and J. Zaleski, *Acta Cryst. Sect. E*, **63**, o4315-o4317 (2007)
- [64] K. Kinbara, A. Kai, Y. Maekawa, Y. Hashimoto, S. Naruse, M. Hasegawa and K. Saigo, *J. Chem. Soc., Perkin Trans. 2*, 247-263 (1996)
- [65] E. Y. Cheung, S. E. David, K. D. M. Harris, B. R. Conway and P. Timmins, *J. Solid State Chem.*, **180**, 1068-1075 (2007)
- [66] J. Li, Z. P. Liang, C. H. Lin and X. S. Tai, *Acta Cryst. Sect. E*, **64**, o2318-o2318 (2008)
- [67] T. Yuge, I. Hisaki, M. Miyata and N. Tohnai, *CrystEngComm*, **10**, 263-266 (2008)

- [68] K. Sada, T. Watanabe, J. Miyamoto, T. Fukuda, N. Tohnai, M. Miyata, T. Kitayama, K. Maehara and K. Ute, *Chem. Lett.*, **33**, 160-161 (2004)

Appendix A

Extended crystallographic data for 1,6-diaminohexane/ methanol/ urea inclusion compound (1,6-DAHx/MeOH/Urea).

Table A.1 Crystal data and structure refinement for 1,6-DAHx/MeOH/Urea

| | | |
|-----------------------------|---|------------------------------|
| Empirical formula | $\text{C}_{14}\text{H}_{48}\text{N}_{14}\text{O}_8$ | |
| Formula weight | 540.66 | |
| Temperature | 293(2) K | |
| Wavelength | 0.71073 Å | |
| Crystal system, space group | Monoclinic, $P2_1/c$ | |
| Unit cell dimensions | $a = 13.2901(4)$ Å | $\alpha = 90^\circ$ |
| | $b = 7.7411(3)$ Å | $\beta = 106.1080(10)^\circ$ |
| | $c = 15.0043(5)$ Å | $\gamma = 90^\circ$ |
| Volume | 1483.04(9) Å ³ | |
| Z | 2 | |
| Calculated density | 1.211 (10 ³ Kg/m ³) | |

Appendix A – Crystal data for 1,6-DAHX/MeOH/Urea

| | |
|---|--|
| Absorption coefficient | 0.098 mm ⁻¹ |
| <i>F</i> (000) | 588 |
| Crystal size | 0.50 × 0.50 × 0.40 mm |
| θ range for data collection | 3.61° to 27.5° |
| Limiting indices | -17 ≤ <i>h</i> ≤ 16, -9 ≤ <i>k</i> ≤ 10, -17 ≤ <i>l</i> ≤ 19 |
| Reflections collected / unique | 10622 / 3336 [<i>R</i> _{int} = 0.0661] |
| Completeness to θ = 27.54 | 97.8 % |
| Refinement method | Full-matrix least-squares on <i>F</i> ² |
| Data / restraints / parameters | 3336 / 0 / 227 |
| Goodness-of-fit on <i>F</i> ² | 1.040 |
| Final <i>R</i> indices [<i>I</i> > 2σ(<i>I</i>)] | <i>R</i> 1 = 0.0538, <i>wR</i> 2 = 0.1331 |
| <i>R</i> indices (all data) | <i>R</i> 1 = 0.0808, <i>wR</i> 2 = 0.1479 |
| Largest difference peak and hole | 0.193 e.Å ⁻³ and -0.175 e.Å ⁻³ |

Appendix A – Crystal data for 1,6-DAHX/MeOH/Urea

Table A.2 Atomic coordinates ($\times 10^4$) and equivalent isotropic displacement parameters ($\text{\AA}^2 \times 10^3$) for 1,6-DAHX/MeOH/Urea, $U(\text{eq})$ is defined as one third of the trace of the orthogonalized U_{ij} tensor.

| | <i>x</i> | <i>y</i> | <i>z</i> | <i>U</i> (eq) |
|------|----------|----------|----------|---------------|
| O(1) | 3541(1) | 10156(2) | -312(1) | 51(1) |
| O(2) | 780(1) | 53(1) | 8732(1) | 48(1) |
| O(3) | -1957(1) | 262(2) | 7634(1) | 49(1) |
| O(4) | 5252(1) | 4915(2) | 1833(1) | 62(1) |
| N(1) | 4494(1) | 8303(3) | -901(1) | 58(1) |
| N(2) | 2720(1) | 7991(3) | -1226(1) | 61(1) |
| N(3) | 1793(1) | 2187(3) | 8433(1) | 56(1) |
| N(4) | 44(1) | 2060(3) | 7666(1) | 55(1) |
| N(5) | -3039(1) | 145(2) | 8549(1) | 64(1) |
| N(6) | -1270(1) | 34(2) | 9179(1) | 57(1) |
| N(7) | 3222(1) | 4798(3) | 1809(1) | 90(1) |
| C(1) | 3591(1) | 8849(2) | -795(1) | 44(1) |
| C(2) | 872(1) | 1400(2) | 8293(1) | 42(1) |
| C(3) | -2087(1) | 151(2) | 8427(1) | 42(1) |
| C(4) | 564(1) | 5024(3) | -5(2) | 68(1) |
| C(5) | 1336(1) | 4910(3) | 921(1) | 64(1) |
| C(6) | 2472(2) | 4910(3) | 916(2) | 64(1) |
| C(7) | 5375(3) | 6379(5) | 1320(3) | 97(1) |

Appendix A – Crystal data for 1,6-DAHx/MeOH/Urea

Table A.3 Bond lengths [Å] and angles [°] for 1,6-DAHx/MeOH/Urea

| | |
|------------------|------------|
| O(1)-C(1) | 1.2565(19) |
| O(2)-C(2) | 1.2574(19) |
| O(3)-C(3) | 1.2519(19) |
| O(4)-C(7) | 1.404(3) |
| N(1)-C(1) | 1.324(2) |
| N(2)-C(1) | 1.336(2) |
| N(3)-C(2) | 1.330(2) |
| N(4)-C(2) | 1.335(2) |
| N(5)-C(3) | 1.328(2) |
| N(6)-C(3) | 1.335(2) |
| N(7)-C(6) | 1.434(3) |
| C(4)-C(5) | 1.483(3) |
| C(4)-C(4)#1 | 1.503(4) |
| C(5)-C(6) | 1.511(3) |
| O(1)-C(1)-N(1) | 121.43(16) |
| O(1)-C(1)-N(2) | 120.16(17) |
| N(1)-C(1)-N(2) | 118.40(18) |
| O(2)-C(2)-N(3) | 121.12(15) |
| O(2)-C(2)-N(4) | 120.28(16) |
| N(3)-C(2)-N(4) | 118.59(18) |
| O(3)-C(3)-N(5) | 121.33(15) |
| O(3)-C(3)-N(6) | 120.95(15) |
| N(5)-C(3)-N(6) | 117.72(16) |
| C(5)-C(4)-C(4)#1 | 115.0(2) |
| C(4)-C(5)-C(6) | 115.35(18) |
| N(7)-C(6)-C(5) | 115.59(18) |

Symmetry transformations used to generate equivalent atoms:

#1 $-x, -y+1, -z$

Appendix A – Crystal data for 1,6-DAHX/MeOH/Urea

Table A.4 Anisotropic displacement parameters ($\text{\AA}^2 \times 10^3$) for 1,6-DAHX/MeOH/Urea. The anisotropic displacement factor exponent takes the form: $-2 \pi^2 [h^2 a^{*2} U_{11} + \dots + 2 h k a^* b^* U_{12}]$

| | U_{11} | U_{22} | U_{33} | U_{23} | U_{13} | U_{12} |
|------|----------|----------|----------|----------|----------|----------|
| O(1) | 41(1) | 60(1) | 51(1) | -12(1) | 8(1) | -2(1) |
| O(2) | 39(1) | 52(1) | 50(1) | 8(1) | 9(1) | 1(1) |
| O(3) | 44(1) | 63(1) | 39(1) | 2(1) | 9(1) | 2(1) |
| O(4) | 43(1) | 70(1) | 67(1) | -1(1) | 7(1) | 3(1) |
| N(1) | 44(1) | 67(1) | 62(1) | -19(1) | 11(1) | 1(1) |
| N(2) | 43(1) | 62(1) | 73(1) | -21(1) | 6(1) | -4(1) |
| N(3) | 47(1) | 54(1) | 64(1) | 11(1) | 12(1) | -4(1) |
| N(4) | 50(1) | 56(1) | 56(1) | 14(1) | 13(1) | 5(1) |
| N(5) | 43(1) | 103(2) | 44(1) | -1(1) | 10(1) | -1(1) |
| N(6) | 44(1) | 85(1) | 39(1) | 6(1) | 7(1) | 1(1) |
| N(7) | 54(1) | 142(2) | 68(1) | 0(1) | 9(1) | 1(1) |
| C(1) | 40(1) | 53(1) | 38(1) | 2(1) | 7(1) | -1(1) |
| C(2) | 42(1) | 45(1) | 40(1) | -3(1) | 13(1) | 3(1) |
| C(3) | 41(1) | 41(1) | 43(1) | -2(1) | 9(1) | 0(1) |
| C(4) | 49(1) | 87(2) | 67(1) | -9(1) | 12(1) | 3(1) |
| C(5) | 51(1) | 74(1) | 66(1) | -6(1) | 16(1) | 0(1) |
| C(6) | 48(1) | 77(1) | 67(1) | -2(1) | 13(1) | 1(1) |
| C(7) | 87(2) | 89(2) | 107(2) | 27(2) | 13(2) | -7(2) |

Appendix A – Crystal data for 1,6-DAHX/MeOH/Urea

Table A.5 Hydrogen coordinates ($\times 10^4$) and isotropic displacement parameters ($\text{\AA}^2 \times 10^3$) for 1,6-DAHX/MeOH/Urea.

| | <i>x</i> | <i>y</i> | <i>z</i> | <i>U</i> (eq) |
|-------|-----------|----------|-----------|---------------|
| H(7B) | 3124 | 3820 | 2085 | 135 |
| H(7C) | 3142 | 5693 | 2155 | 135 |
| H(4C) | 687 | 4076 | -384 | 82 |
| H(4D) | 685 | 6090 | -299 | 82 |
| H(5C) | 1201 | 3860 | 1221 | 76 |
| H(5D) | 1224 | 5876 | 1293 | 76 |
| H(6C) | 2583 | 3945 | 542 | 77 |
| H(6D) | 2606 | 5961 | 615 | 77 |
| H(1A) | 5018(18) | 8790(30) | -591(15) | 67(6) |
| H(1B) | 4547(16) | 7430(30) | -1145(14) | 56(6) |
| H(5B) | -3108(16) | 100(20) | 9076(15) | 60(6) |
| H(6A) | -1396(16) | -10(30) | 9709(15) | 63(6) |
| H(2A) | 2144(17) | 8400(30) | -1160(13) | 57(5) |
| H(4A) | -549(19) | 1580(30) | 7606(15) | 68(6) |
| H(3B) | 1832(15) | 3010(30) | 8179(13) | 46(6) |
| H(3A) | 2300(16) | 1790(20) | 8834(14) | 53(5) |
| H(6B) | -670(20) | -10(30) | 9096(16) | 76(7) |
| H(4B) | 124(15) | 2880(30) | 7407(14) | 52(6) |
| H(2B) | 2762(17) | 7150(30) | -1495(16) | 68(7) |
| H(5A) | -3509(18) | 190(20) | 8088(16) | 55(6) |
| H(4) | 4580(20) | 4810(30) | 1854(16) | 77(7) |
| H(7A) | 4900(40) | 6430(50) | 760(40) | 187(18) |
| H(7C) | 5150(40) | 7380(60) | 1540(30) | 170(18) |
| H(7B) | 6110(40) | 6510(50) | 1190(30) | 171(15) |

Appendix B

Extended crystallographic data for 2-bromoadamantane/thiourea inclusion compound (2-BA/TIC).

Table B.1 Crystal data and structure refinement for 2-BA/TIC

| | | |
|-----------------------------|--|----------------------|
| Empirical formula | $\text{C}_{55}\text{H}_{120}\text{Br}_4\text{N}_{30}\text{S}_{15}$ | |
| Formula weight | 2002.35 | |
| Temperature | 110(2) K | |
| Wavelength | 0.71073 Å | |
| Crystal system, space group | Trigonal, $R\bar{3}c$ | |
| Unit cell dimensions | $a = 16.1180(2)$ Å | $\alpha = 90^\circ$ |
| | $b = 16.1180(2)$ Å | $\beta = 90^\circ$ |
| | $c = 61.6020(4)$ Å | $\gamma = 120^\circ$ |
| Volume | 13859.5(3) Å ³ | |
| Z | 6 | |
| Calculated density | 1.439 (10 ³ Kg/m ³) | |

Appendix B – Crystal data for 2-BA/TIC

| | |
|---|---|
| Absorption coefficient | 2.133 mm ⁻¹ |
| <i>F</i> (000) | 6240 |
| Crystal size | 0.50 × 0.40 × 0.40 mm |
| θ range for data collection | 1.97° to 27.69° |
| Limiting indices | -20 ≤ <i>h</i> ≤ 20, -21 ≤ <i>k</i> ≤ 20, -79 ≤ <i>l</i> ≤ 75 |
| Reflections collected / unique | 31291 / 3564 [<i>R</i> _{int} = 0.0647] |
| Completeness to θ = 27.69 | 98.5 % |
| Max. and min. transmission | 0.4824 and 0.4152 |
| Refinement method | Full-matrix least-squares on <i>F</i> ² |
| Data / restraints / parameters | 3564 / 269 / 248 |
| Goodness-of-fit on <i>F</i> ² | 1.052 |
| Final <i>R</i> indices [<i>I</i> > 2σ(<i>I</i>)] | <i>R</i> 1 = 0.1405, <i>wR</i> 2 = 0.3493 |
| <i>R</i> indices (all data) | <i>R</i> 1 = 0.1761, <i>wR</i> 2 = 0.3734 |
| Largest difference peak and hole | 1.492 e.Å ⁻³ and -1.207 e.Å ⁻³ |

Appendix B – Crystal data for 2-BA/TIC

Table B.2 Atomic coordinates ($\times 10^4$) and equivalent isotropic displacement parameters ($\text{\AA}^2 \times 10^3$) for 2-BA/TIC. $U(\text{eq})$ is defined as one third of the trace of the orthogonalized U_{ij} tensor.

| | <i>x</i> | <i>y</i> | <i>z</i> | <i>U</i> (eq) |
|-------|----------|----------|----------|---------------|
| C(1) | 5920(5) | -3(5) | 9501(1) | 21(1) |
| C(2) | 2606(5) | -827(4) | 9836(1) | 21(1) |
| C(3) | 3333 | 741(5) | 9167 | 16(2) |
| N(1) | 5553(4) | 94(5) | 9320(1) | 29(1) |
| N(2) | 5395(4) | -193(4) | 9681(1) | 24(1) |
| N(3) | 2244(5) | -1274(5) | 9648(1) | 36(2) |
| N(4) | 2155(4) | -1179(4) | 10022(1) | 23(1) |
| N(5) | 3353(5) | 1189(4) | 9349(1) | 27(1) |
| S(1) | 6978(1) | -16(1) | 9502(1) | 20(1) |
| S(2) | 3655(1) | 286(1) | 9830(1) | 17(1) |
| S(3) | 3333 | -305(1) | 9167 | 20(1) |
| C(4) | 6667 | 3333 | 9948(2) | 33(5) |
| C(5) | 6405(11) | 4069(9) | 9864(2) | 38(3) |
| C(6) | 6430(7) | 4070(7) | 9610(1) | 25(2) |
| C(7) | 5682(9) | 3105(7) | 9522(2) | 28(3) |
| Br(1) | 5639(3) | 3070(4) | 9225(1) | 37(1) |
| C(8) | 6667 | 3333 | 8676(4) | 92(8) |
| C(9) | 5703(9) | 2536(10) | 8586(2) | 79(7) |
| C(10) | 5760(15) | 2592(12) | 8333(2) | 36(4) |
| C(11) | 5808(11) | 3517(8) | 8264(2) | 39(4) |
| Br(2) | 5768(7) | 3658(7) | 7982(2) | 90(3) |
| C(12) | 6667 | 3333 | 10677(3) | 79(8) |
| C(13) | 7360(10) | 4302(9) | 10778(2) | 94(7) |
| C(14) | 7318(12) | 4226(13) | 11026(2) | 65(5) |
| C(15) | 7783(9) | 3640(9) | 11106(2) | 41(3) |
| Br(3) | 7696(6) | 3622(6) | 11408(1) | 78(2) |
| C(16) | 6667 | 3333 | 9714(3) | 60(5) |
| C(17) | 5662(8) | 3076(10) | 9628(2) | 41(4) |
| C(18) | 5701(13) | 3069(10) | 9377(2) | 67(5) |
| C(19) | 5887(11) | 2271(11) | 9307(2) | 63(5) |
| Br(4) | 5861(7) | 2109(5) | 9023(1) | 86(2) |

Appendix B – Crystal data for 2-BA/TIC

Table B.3 Bond lengths [Å] and angles [°] for 2-BA/TIC

| | |
|---------------|-----------|
| C(1)-N(1) | 1.302(9) |
| C(1)-N(2) | 1.340(8) |
| C(1)-S(1) | 1.715(7) |
| C(2)-N(4) | 1.323(8) |
| C(2)-N(3) | 1.334(9) |
| C(2)-S(2) | 1.746(7) |
| C(3)-N(5)#1 | 1.324(7) |
| C(3)-N(5) | 1.325(7) |
| C(3)-S(3) | 1.687(9) |
| C(4)-C(5)#2 | 1.533(9) |
| C(4)-C(5)#3 | 1.533(9) |
| C(4)-C(5) | 1.533(9) |
| C(5)-C(6) | 1.563(9) |
| C(6)-C(7) | 1.514(9) |
| C(6)-C(7)#2 | 1.541(9) |
| C(7)-C(6)#3 | 1.541(9) |
| Br(1)-Br(1)#2 | 2.580(8) |
| Br(1)-Br(1)#3 | 2.580(8) |
| C(8)-C(9)#3 | 1.541(10) |
| C(8)-C(9) | 1.541(10) |
| C(8)-C(9)#2 | 1.541(10) |
| C(9)-C(10) | 1.559(9) |
| C(10)-C(11) | 1.516(9) |
| C(10)-C(11)#3 | 1.530(9) |
| C(11)-C(10)#2 | 1.530(10) |
| C(12)-C(13)#2 | 1.528(10) |
| C(12)-C(13) | 1.528(10) |
| C(12)-C(13)#3 | 1.528(10) |
| C(12)-C(12)#4 | 1.93(4) |
| C(13)-C(14) | 1.532(9) |
| C(13)-C(12)#5 | 1.909(17) |
| C(14)-C(15) | 1.550(9) |
| C(14)-C(15)#3 | 1.559(10) |
| C(15)-C(14)#2 | 1.559(10) |
| Br(3)-Br(3)#2 | 2.568(14) |
| Br(3)-Br(3)#3 | 2.568(14) |
| C(16)-C(17)#3 | 1.550(9) |
| C(16)-C(17)#2 | 1.550(10) |

Appendix B – Crystal data for 2-BA/TIC

| | |
|-----------------------|-----------|
| C(16)-C(17) | 1.550(9) |
| C(17)-C(18) | 1.549(9) |
| C(18)-C(19) | 1.522(10) |
| C(18)-C(19)#2 | 1.540(10) |
| C(19)-C(18)#3 | 1.540(10) |
| N(1)-C(1)-N(2) | 117.5(6) |
| N(1)-C(1)-S(1) | 121.3(5) |
| N(2)-C(1)-S(1) | 120.8(5) |
| N(4)-C(2)-N(3) | 121.5(6) |
| N(4)-C(2)-S(2) | 120.2(5) |
| N(3)-C(2)-S(2) | 118.2(5) |
| N(5)#1-C(3)-N(5) | 115.6(8) |
| N(5)#1-C(3)-S(3) | 122.2(4) |
| N(5)-C(3)-S(3) | 122.2(4) |
| C(5)#2-C(4)-C(5)#3 | 109.2(6) |
| C(5)#2-C(4)-C(5) | 109.2(6) |
| C(5)#3-C(4)-C(5) | 109.2(6) |
| C(4)-C(5)-C(6) | 108.8(8) |
| C(7)-C(6)-C(7)#2 | 109.3(12) |
| C(7)-C(6)-C(5) | 110.5(7) |
| C(7)#2-C(6)-C(5) | 112.0(8) |
| C(6)-C(7)-C(6)#3 | 106.9(11) |
| Br(1)#2-Br(1)-Br(1)#3 | 60.000(3) |
| C(9)#3-C(8)-C(9) | 107.9(9) |
| C(9)#3-C(8)-C(9)#2 | 107.9(9) |
| C(9)-C(8)-C(9)#2 | 107.9(9) |
| C(8)-C(9)-C(10) | 107.7(9) |
| C(11)-C(10)-C(11)#3 | 124(2) |
| C(11)-C(10)-C(9) | 108.1(8) |
| C(11)#3-C(10)-C(9) | 107.0(7) |
| C(10)-C(11)-C(10)#2 | 100(2) |
| C(13)#2-C(12)-C(13) | 104.4(9) |
| C(13)#2-C(12)-C(13)#3 | 104.4(9) |
| C(13)-C(12)-C(13)#3 | 104.4(9) |
| C(13)#2-C(12)-C(12)#4 | 65.8(8) |
| C(13)-C(12)-C(12)#4 | 65.8(8) |
| C(13)#3-C(12)-C(12)#4 | 65.8(8) |
| C(12)-C(13)-C(14) | 110.2(9) |
| C(12)-C(13)-C(12)#5 | 67.2(13) |

Appendix B – Crystal data for 2-BA/TIC

| | |
|-----------------------|-----------|
| C(14)-C(13)-C(12)#5 | 43.0(11) |
| C(13)-C(14)-C(15) | 110.3(8) |
| C(13)-C(14)-C(15)#3 | 108.8(7) |
| C(15)-C(14)-C(15)#3 | 127.5(15) |
| C(14)-C(15)-C(14)#2 | 91.8(18) |
| Br(3)#2-Br(3)-Br(3)#3 | 60.000(7) |
| C(17)#3-C(16)-C(17)#2 | 109.0(7) |
| C(17)#3-C(16)-C(17) | 109.0(7) |
| C(17)#2-C(16)-C(17) | 109.0(7) |
| C(18)-C(17)-C(16) | 107.5(8) |
| C(19)-C(18)-C(19)#2 | 120.7(19) |
| C(19)-C(18)-C(17) | 108.3(8) |
| C(19)#2-C(18)-C(17) | 106.2(7) |
| C(18)-C(19)-C(18)#3 | 104.0(18) |

Symmetry transformations used to generate equivalent atoms:

#1 $-x+2/3, -x+y+1/3, -z+11/6$

#2 $-x+y+1, -x+1, z$

#3 $-y+1, x-y, z$

#4 $x-y+1/3, -y+2/3, -z+13/6$

#5 $-x+4/3, -x+y+2/3, -z+13/6$

Appendix B – Crystal data for 2-BA/TIC

Table B.4 Anisotropic displacement parameters ($\text{\AA}^2 \times 10^3$) for 2-BA/TIC. The anisotropic displacement factor exponent takes the form: $-2 \pi^2 [h^2 a^{*2} U_{11} + \dots + 2 h k a^* b^* U_{12}]$

| | U_{11} | U_{22} | U_{33} | U_{23} | U_{13} | U_{12} |
|-------|----------|----------|----------|----------|----------|----------|
| C(1) | 29(3) | 22(3) | 21(3) | 0(2) | 8(3) | 20(3) |
| C(2) | 27(3) | 12(3) | 22(3) | 4(2) | 9(2) | 8(3) |
| C(3) | 9(4) | 21(3) | 14(4) | 4(1) | 8(3) | 5(2) |
| N(1) | 21(3) | 40(4) | 27(3) | -3(3) | -3(2) | 16(3) |
| N(2) | 17(3) | 40(3) | 17(2) | 2(2) | 7(2) | 15(2) |
| N(3) | 29(3) | 35(4) | 28(3) | 2(3) | 7(3) | 5(3) |
| N(4) | 20(3) | 26(3) | 19(3) | 2(2) | 2(2) | 9(2) |
| N(5) | 53(4) | 25(3) | 12(3) | -6(2) | -4(2) | 26(3) |
| S(1) | 21(1) | 23(1) | 18(1) | 0(1) | 2(1) | 13(1) |
| S(2) | 18(1) | 16(1) | 13(1) | -1(1) | 3(1) | 5(1) |
| S(3) | 21(1) | 19(1) | 20(1) | 0(1) | 0(1) | 11(1) |
| C(4) | 31(5) | 31(5) | 37(8) | 0 | 0 | 16(3) |
| C(5) | 31(6) | 30(6) | 61(7) | -9(5) | -10(5) | 22(5) |
| C(6) | 20(4) | 20(4) | 43(5) | -1(3) | -7(3) | 16(3) |
| C(7) | 25(5) | 23(5) | 38(6) | -6(5) | -7(5) | 14(4) |
| Br(1) | 25(2) | 43(3) | 46(2) | -12(2) | -10(2) | 19(2) |
| C(8) | 90(8) | 90(8) | 95(12) | 0 | 0 | 45(4) |
| C(9) | 73(9) | 76(9) | 85(10) | 3(8) | -2(8) | 35(7) |
| C(10) | 29(7) | 35(7) | 47(8) | 6(6) | 6(6) | 18(6) |
| C(11) | 30(7) | 32(7) | 58(9) | -3(6) | -11(6) | 17(5) |
| Br(2) | 102(6) | 98(6) | 105(6) | 16(5) | 2(5) | 75(5) |
| C(12) | 82(8) | 82(8) | 73(11) | 0 | 0 | 41(4) |
| C(13) | 94(10) | 80(9) | 94(10) | 5(8) | -4(8) | 33(7) |
| C(14) | 71(8) | 57(8) | 74(8) | 2(7) | 8(7) | 37(6) |
| C(15) | 66(8) | 32(6) | 46(7) | 14(5) | 28(6) | 40(6) |
| Br(3) | 77(4) | 86(5) | 83(4) | -2(4) | -9(4) | 40(4) |
| C(16) | 60(6) | 60(6) | 60(9) | 0 | 0 | 30(3) |
| C(17) | 38(6) | 41(6) | 44(7) | 4(6) | 11(6) | 19(5) |
| C(18) | 58(7) | 66(7) | 64(7) | 3(7) | -2(7) | 21(6) |
| C(19) | 54(8) | 54(7) | 80(8) | -7(7) | -3(7) | 26(6) |
| Br(4) | 120(6) | 54(4) | 75(4) | 10(3) | 22(4) | 37(4) |

Appendix B – Crystal data for 2-BA/TIC

Table B.5 Hydrogen coordinates ($\times 10^4$) and isotropic displacement parameters ($\text{\AA}^2 \times 10^3$) for 2-BA/TIC

| | <i>x</i> | <i>y</i> | <i>z</i> | <i>U</i> (eq) |
|--------|----------|----------|----------|---------------|
| H(1A) | 4980 | 35 | 9321 | 35 |
| H(1B) | 5879 | 219 | 9199 | 35 |
| H(2A) | 4824 | -248 | 9676 | 29 |
| H(2B) | 5620 | -263 | 9806 | 29 |
| H(3A) | 1693 | -1815 | 9646 | 43 |
| H(3B) | 2555 | -1027 | 9526 | 43 |
| H(4A) | 1604 | -1720 | 10024 | 27 |
| H(4B) | 2406 | -873 | 10144 | 27 |
| H(5A) | 3352 | 1734 | 9343 | 33 |
| H(5B) | 3367 | 941 | 9475 | 33 |
| H(4) | 6667 | 3333 | 10110 | 40 |
| H(5C) | 6868 | 4714 | 9920 | 45 |
| H(5D) | 5757 | 3900 | 9915 | 45 |
| H(6) | 6278 | 4564 | 9557 | 30 |
| H(7A) | 5693 | 3110 | 9362 | 33 |
| H(7B) | 5035 | 2950 | 9571 | 33 |
| H(8) | 6667 | 3333 | 8838 | 110 |
| H(9A) | 5173 | 2627 | 8638 | 95 |
| H(9B) | 5584 | 1901 | 8636 | 95 |
| H(10) | 5124 | 2069 | 8281 | 43 |
| H(11A) | 5330 | 3622 | 8341 | 47 |
| H(11B) | 5719 | 3536 | 8105 | 47 |
| H(12) | 6667 | 3333 | 10514 | 95 |
| H(13A) | 7190 | 4786 | 10731 | 113 |
| H(13B) | 8020 | 4514 | 10728 | 113 |
| H(14) | 7801 | 4892 | 11072 | 78 |
| H(15A) | 7877 | 3666 | 11265 | 49 |
| H(15B) | 8385 | 3804 | 11029 | 49 |
| H(16) | 6667 | 3333 | 9876 | 72 |
| H(17A) | 5172 | 2439 | 9682 | 50 |
| H(17B) | 5492 | 3556 | 9678 | 50 |
| H(18) | 5049 | 2894 | 9323 | 80 |
| H(19A) | 5812 | 2170 | 9148 | 75 |
| H(19B) | 5444 | 1662 | 9381 | 75 |

Appendix C

Extended crystallographic data for bromocyclohexane/ thiourea inclusion compound (BCHX/TIC).

Table C.1 Crystal data and structure refinement for BCHX/TIC

| | | |
|-----------------------------|---|----------------------------|
| Empirical formula | $\text{C}_9\text{H}_{23}\text{BrN}_6\text{S}_3$ | |
| Formula weight | 391.42 | |
| Temperature | 110(2) K | |
| Wavelength | 0.71073 Å | |
| Crystal system, space group | Monoclinic, $P2_1/a$ | |
| Unit cell dimensions | $a = 9.6533(4)$ Å | $\alpha = 90^\circ$ |
| | $b = 15.9651(6)$ Å | $\beta = 111.835(2)^\circ$ |
| | $c = 12.2869(3)$ Å | $\gamma = 90^\circ$ |
| Volume | 1757.76(11) Å ³ | |
| Z | 4 | |
| Calculated density | 1.479 (10 ³ Kg/m ³) | |

Appendix C – Crystal data for BCHX/TIC

| | |
|--|--|
| Absorption coefficient | 2.692 mm ⁻¹ |
| <i>F</i> (000) | 808 |
| Crystal size | 0.30 × 0.20 × 0.20 mm |
| θ range for data collection | 2.19° to 27.54° |
| Limiting indices | $-12 \leq h \leq 12$, $-20 \leq k \leq 20$, $-15 \leq l \leq 15$ |
| Reflections collected / unique | 7218 / 4005 [$R_{\text{int}} = 0.0373$] |
| Completeness to $\theta = 27.54$ | 98.7 % |
| Refinement method | Full-matrix least-squares on F^2 |
| Data / restraints / parameters | 4005/ 247 / 237 |
| Goodness-of-fit on F^2 | 1.120 |
| Final R indices [$I > 2\sigma(I)$] | $R1 = 0.0644$, $wR2 = 0.1436$ |
| R indices (all data) | $R1 = 0.0837$, $wR2 = 0.1525$ |
| Largest difference peak and hole | 1.151 e.Å ⁻³ and -1.005 e.Å ⁻³ |

Appendix C – Crystal data for BCHX/TIC

Table C.2 Atomic coordinates ($\times 10^4$) and equivalent isotropic displacement parameters ($\text{\AA}^2 \times 10^3$) for BCHX/TIC, $U(\text{eq})$ is defined as one third of the trace of the orthogonalized U_{ij} tensor.

| | <i>x</i> | <i>y</i> | <i>z</i> | <i>U</i> (eq) |
|--------|----------|----------|----------|---------------|
| C(1) | 3626(5) | -2047(3) | 9201(3) | 21(1) |
| C(2) | 2582(5) | 932(3) | 7704(4) | 22(1) |
| C(3) | 3241(5) | 3016(3) | 4780(4) | 21(1) |
| S(1) | 4751(1) | -1443(1) | 8715(1) | 22(1) |
| S(2) | 2315(1) | 1991(1) | 7781(1) | 22(1) |
| S(3) | 4370(1) | 3592(1) | 4257(1) | 22(1) |
| N(1) | 4179(4) | -2459(2) | 10210(3) | 27(1) |
| N(2) | 2177(4) | -2124(2) | 8557(3) | 27(1) |
| N(3) | 2035(4) | 536(2) | 6675(3) | 27(1) |
| N(4) | 3342(4) | 498(2) | 8652(3) | 29(1) |
| N(5) | 1809(4) | 2924(2) | 4144(3) | 26(1) |
| N(6) | 3800(4) | 2666(2) | 5832(3) | 27(1) |
| C(4) | 3141(6) | 4326(4) | 7761(4) | 40(1) |
| C(5) | 1655(7) | 4347(3) | 6691(6) | 43(2) |
| C(6) | 828(5) | 5174(3) | 6637(5) | 36(1) |
| C(7) | 1803(6) | 5912(3) | 6576(6) | 40(2) |
| C(8) | 3287(5) | 5903(3) | 7619(5) | 36(1) |
| C(9) | 4097(6) | 5071(3) | 7656(6) | 37(1) |
| Br(1) | 2897(1) | 4265(1) | 9198(1) | 50(1) |
| C(4A) | 2976(18) | 5029(9) | 6766(14) | 44(3) |
| C(5A) | 2160(30) | 4218(10) | 6840(18) | 43(3) |
| C(6A) | 1280(20) | 4301(15) | 7644(18) | 44(4) |
| C(7A) | 2260(30) | 4600(17) | 8859(18) | 50(4) |
| C(8A) | 3200(30) | 5361(15) | 8840(19) | 51(4) |
| C(9A) | 4052(18) | 5244(15) | 8017(15) | 41(3) |
| Br(1A) | 1725(5) | 5922(3) | 6011(5) | 72(2) |

Appendix C – Crystal data for BCHX/TIC

Table C.3 Bond lengths [Å] and angles [°] for BCHX/TIC

| | |
|-----------------|-----------|
| C(1)-N(1) | 1.327(5) |
| C(1)-N(2) | 1.332(5) |
| C(1)-S(1) | 1.717(4) |
| C(2)-N(4) | 1.319(6) |
| C(2)-N(3) | 1.335(5) |
| C(2)-S(2) | 1.718(4) |
| C(3)-N(5) | 1.319(5) |
| C(3)-N(6) | 1.324(5) |
| C(3)-S(3) | 1.722(4) |
| C(4)-C(9) | 1.540(4) |
| C(4)-C(5) | 1.544(4) |
| C(4)-Br(1) | 1.869(4) |
| C(5)-C(6) | 1.531(4) |
| C(6)-C(7) | 1.527(4) |
| C(7)-C(8) | 1.526(4) |
| C(8)-C(9) | 1.532(4) |
| C(4A)-C(5A) | 1.538(10) |
| C(4A)-C(9A) | 1.539(10) |
| C(4A)-Br(1A) | 1.876(10) |
| C(5A)-C(6A) | 1.527(11) |
| C(6A)-C(7A) | 1.517(11) |
| C(7A)-C(8A) | 1.521(11) |
| C(8A)-C(9A) | 1.533(11) |
| N(1)-C(1)-N(2) | 118.5(4) |
| N(1)-C(1)-S(1) | 121.1(3) |
| N(2)-C(1)-S(1) | 120.4(3) |
| N(4)-C(2)-N(3) | 118.8(4) |
| N(4)-C(2)-S(2) | 121.0(3) |
| N(3)-C(2)-S(2) | 120.2(3) |
| N(5)-C(3)-N(6) | 119.2(4) |
| N(5)-C(3)-S(3) | 120.5(3) |
| N(6)-C(3)-S(3) | 120.3(3) |
| C(9)-C(4)-C(5) | 107.9(5) |
| C(9)-C(4)-Br(1) | 114.1(4) |
| C(5)-C(4)-Br(1) | 113.7(4) |
| C(6)-C(5)-C(4) | 111.1(4) |
| C(7)-C(6)-C(5) | 110.3(4) |

Appendix C – Crystal data for BCHX/TIC

| | |
|--------------------|-----------|
| C(8)-C(7)-C(6) | 110.7(4) |
| C(7)-C(8)-C(9) | 110.1(4) |
| C(8)-C(9)-C(4) | 110.9(4) |
| C(5A)-C(4A)-C(9A) | 107.5(11) |
| C(5A)-C(4A)-Br(1A) | 114.7(11) |
| C(9A)-C(4A)-Br(1A) | 113.3(11) |
| C(6A)-C(5A)-C(4A) | 112.7(11) |
| C(7A)-C(6A)-C(5A) | 111.7(12) |
| C(6A)-C(7A)-C(8A) | 113.2(13) |
| C(7A)-C(8A)-C(9A) | 112.5(13) |
| C(8A)-C(9A)-C(4A) | 110.9(11) |

Appendix C – Crystal data for BCHX/TIC

Table C.4 Anisotropic displacement parameters ($\text{\AA}^2 \times 10^3$) for BCHX/TIC. The anisotropic displacement factor exponent takes the form: $-2 \pi^2 [h^2 a^{*2} U_{11} + \dots + 2 h k a^* b^* U_{12}]$

| | U_{11} | U_{22} | U_{33} | U_{23} | U_{13} | U_{12} |
|--------|----------|----------|----------|----------|----------|----------|
| C(1) | 21(2) | 23(2) | 17(2) | -2(2) | 6(2) | 2(2) |
| C(2) | 19(2) | 22(2) | 22(2) | 0(2) | 4(2) | -1(2) |
| C(3) | 21(2) | 20(2) | 20(2) | -2(2) | 8(2) | -2(2) |
| S(1) | 20(1) | 23(1) | 20(1) | 2(1) | 6(1) | -1(1) |
| S(2) | 23(1) | 20(1) | 19(1) | 0(1) | 4(1) | 2(1) |
| S(3) | 20(1) | 25(1) | 19(1) | 2(1) | 4(1) | -2(1) |
| N(1) | 22(2) | 30(2) | 25(2) | 9(2) | 5(2) | 0(2) |
| N(2) | 22(2) | 34(2) | 23(2) | 4(2) | 7(2) | -4(2) |
| N(3) | 31(2) | 22(2) | 24(2) | -4(1) | 4(2) | 2(2) |
| N(4) | 30(2) | 22(2) | 27(2) | 0(2) | 0(2) | 3(2) |
| N(5) | 19(2) | 37(2) | 22(2) | 5(2) | 5(1) | -2(2) |
| N(6) | 25(2) | 33(2) | 21(2) | 5(2) | 5(2) | -4(2) |
| C(4) | 45(3) | 28(3) | 43(3) | -1(2) | 12(2) | 7(2) |
| C(5) | 47(3) | 34(3) | 40(3) | -5(2) | 7(3) | 4(3) |
| C(6) | 36(3) | 35(3) | 32(3) | -5(2) | 10(2) | 2(3) |
| C(7) | 42(4) | 33(3) | 46(4) | 2(3) | 19(3) | 9(3) |
| C(8) | 34(3) | 32(3) | 44(3) | 4(2) | 15(2) | -3(2) |
| C(9) | 33(3) | 41(3) | 40(3) | 2(3) | 17(2) | 5(2) |
| Br(1) | 69(1) | 45(1) | 36(1) | 7(1) | 21(1) | -9(1) |
| C(4A) | 44(4) | 39(4) | 46(4) | -1(4) | 11(4) | 1(4) |
| C(5A) | 48(5) | 36(5) | 44(5) | -2(5) | 16(4) | 6(5) |
| C(6A) | 47(6) | 41(5) | 45(5) | 0(5) | 18(5) | 4(5) |
| C(7A) | 48(6) | 51(6) | 53(6) | 7(6) | 23(5) | 6(6) |
| C(8A) | 49(6) | 50(7) | 51(6) | -1(6) | 17(5) | 0(6) |
| C(9A) | 40(4) | 39(5) | 44(5) | -2(4) | 15(4) | 0(4) |
| Br(1A) | 60(2) | 54(2) | 98(4) | 25(2) | 23(2) | 2(2) |

Appendix C – Crystal data for BCHX/TIC

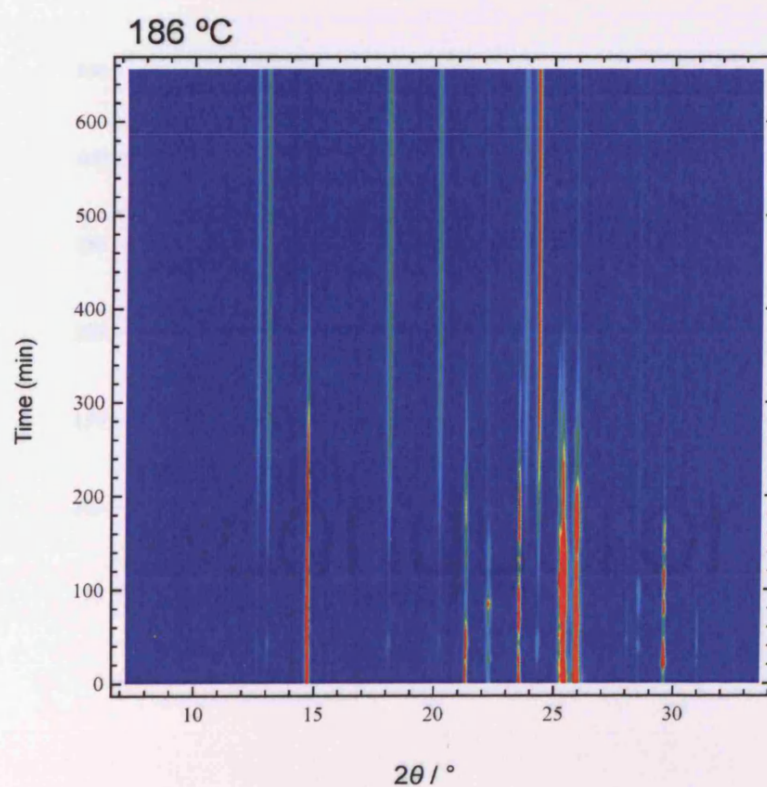
Table C.5 Hydrogen coordinates ($\times 10^4$) and isotropic displacement parameters ($\text{\AA}^2 \times 10^3$) for BCHX/TIC

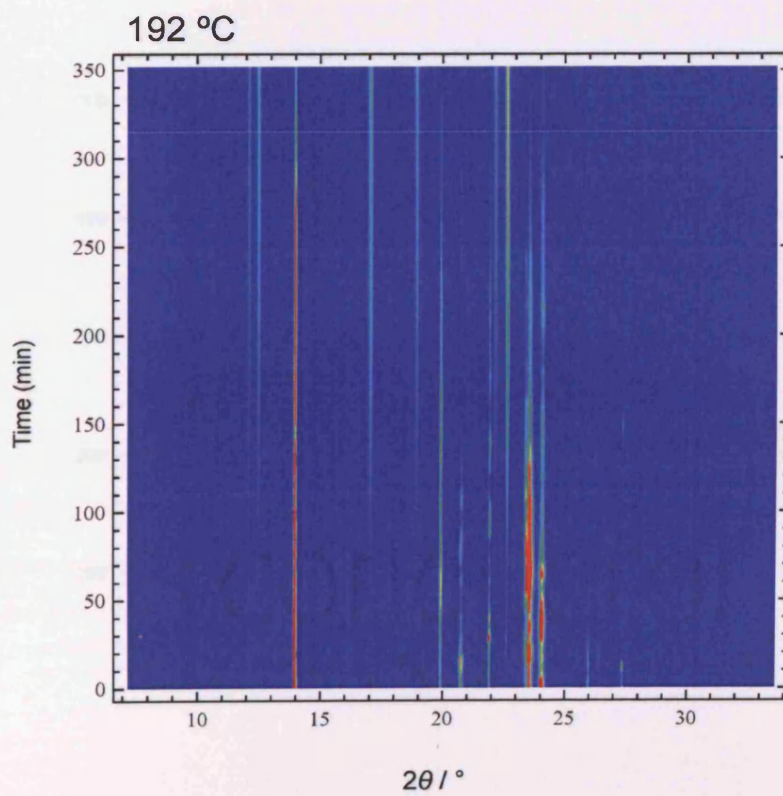
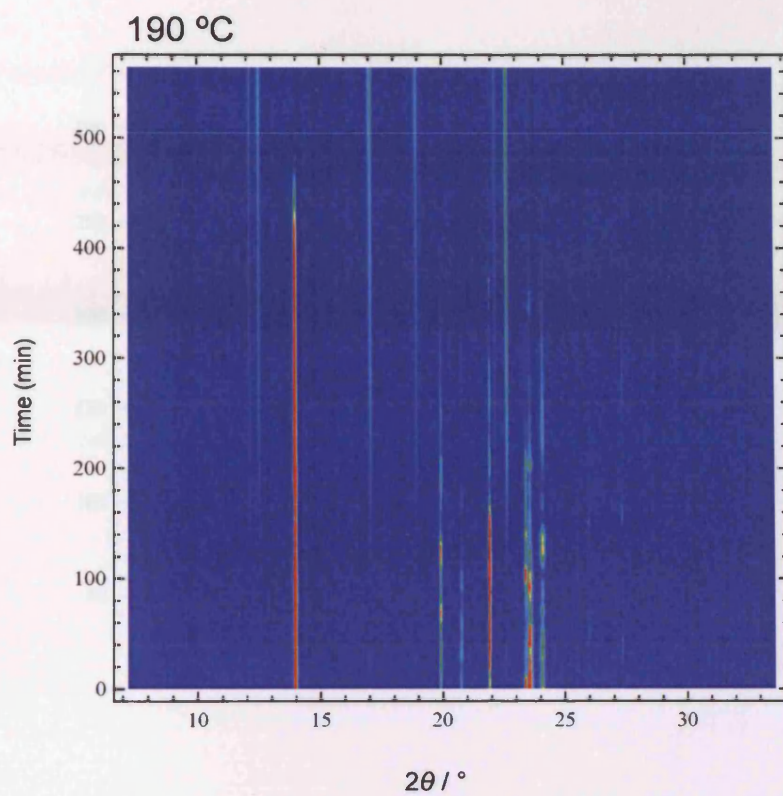
| | <i>x</i> | <i>y</i> | <i>z</i> | <i>U</i> (eq) |
|--------|----------|----------|----------|---------------|
| H(1A) | 3591 | -2773 | 10440 | 32 |
| H(1B) | 5133 | -2417 | 10648 | 32 |
| H(2A) | 1608 | -2442 | 8804 | 32 |
| H(2B) | 1788 | -1856 | 7885 | 32 |
| H(3A) | 2184 | -5 | 6637 | 33 |
| H(3B) | 1525 | 816 | 6033 | 33 |
| H(4A) | 3480 | -43 | 8598 | 35 |
| H(4B) | 3710 | 749 | 9337 | 35 |
| H(5A) | 1238 | 2632 | 4419 | 32 |
| H(5B) | 1426 | 3154 | 3444 | 32 |
| H(6A) | 3217 | 2376 | 6097 | 33 |
| H(6B) | 4753 | 2724 | 6264 | 33 |
| H(4) | 3676 | 3805 | 7690 | 48 |
| H(5C) | 1859 | 4278 | 5964 | 51 |
| H(5D) | 1017 | 3875 | 6742 | 51 |
| H(6C) | -110 | 5177 | 5937 | 43 |
| H(6D) | 569 | 5229 | 7341 | 43 |
| H(7A) | 1991 | 5882 | 5838 | 48 |
| H(7B) | 1272 | 6443 | 6573 | 48 |
| H(8A) | 3105 | 5976 | 8355 | 44 |
| H(8B) | 3918 | 6373 | 7551 | 44 |
| H(9A) | 5058 | 5072 | 8335 | 44 |
| H(9B) | 4314 | 5011 | 6934 | 44 |
| H(4A1) | 3603 | 4897 | 6299 | 53 |
| H(5A1) | 1461 | 4063 | 6043 | 52 |
| H(5A2) | 2893 | 3760 | 7132 | 52 |
| H(6A1) | 449 | 4703 | 7296 | 53 |
| H(6A2) | 840 | 3751 | 7707 | 53 |
| H(7A1) | 2930 | 4138 | 9277 | 60 |
| H(7A2) | 1621 | 4741 | 9303 | 60 |
| H(8A1) | 3924 | 5469 | 9644 | 61 |
| H(8A2) | 2543 | 5857 | 8586 | 61 |
| H(9A1) | 4792 | 4789 | 8317 | 50 |
| H(9A2) | 4598 | 5766 | 7999 | 50 |

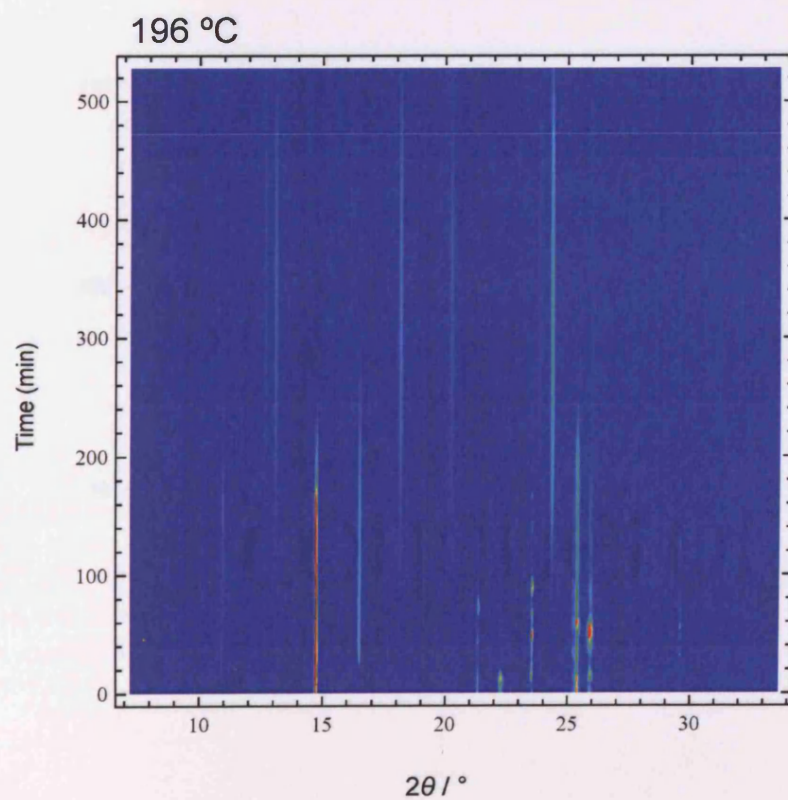
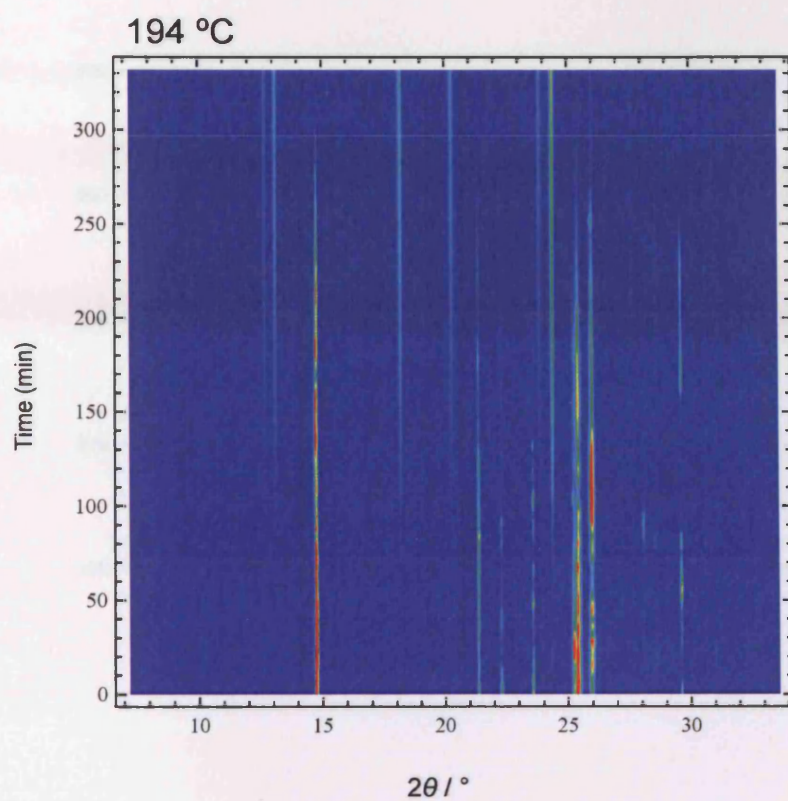
Appendix D

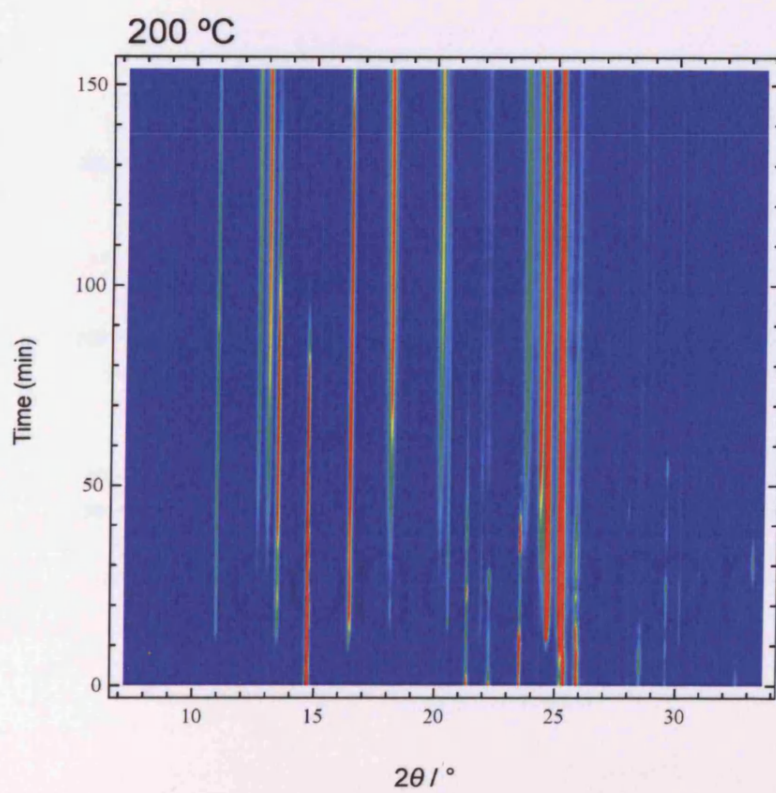
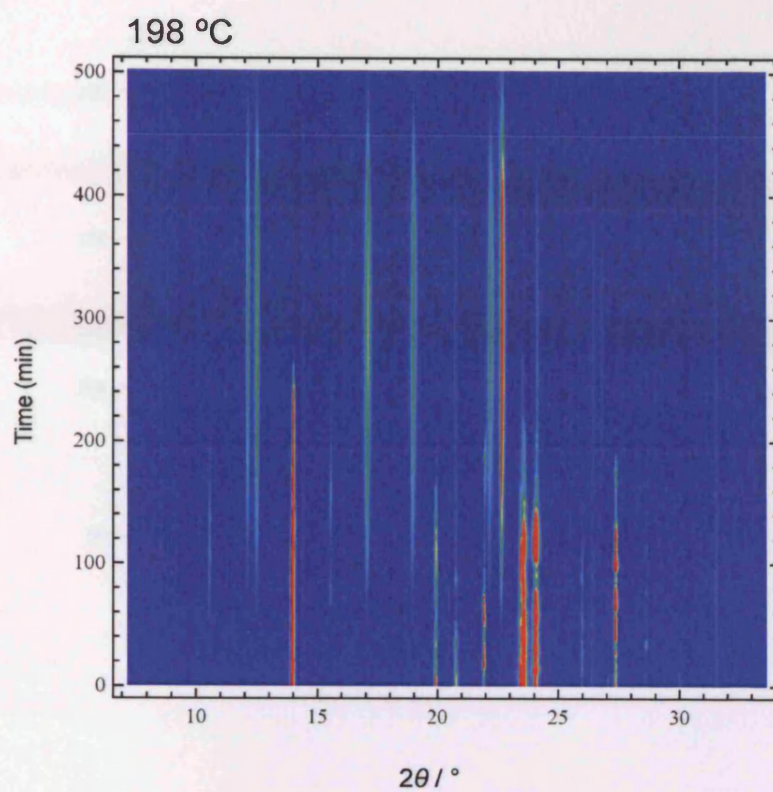
Graphs showing the evolution of the α polymorph of ODH, the γ polymorph of ODH and DOHH as a function of time at different temperatures, with intensity represented in different colours (dark blue the least intense and red the most intense)

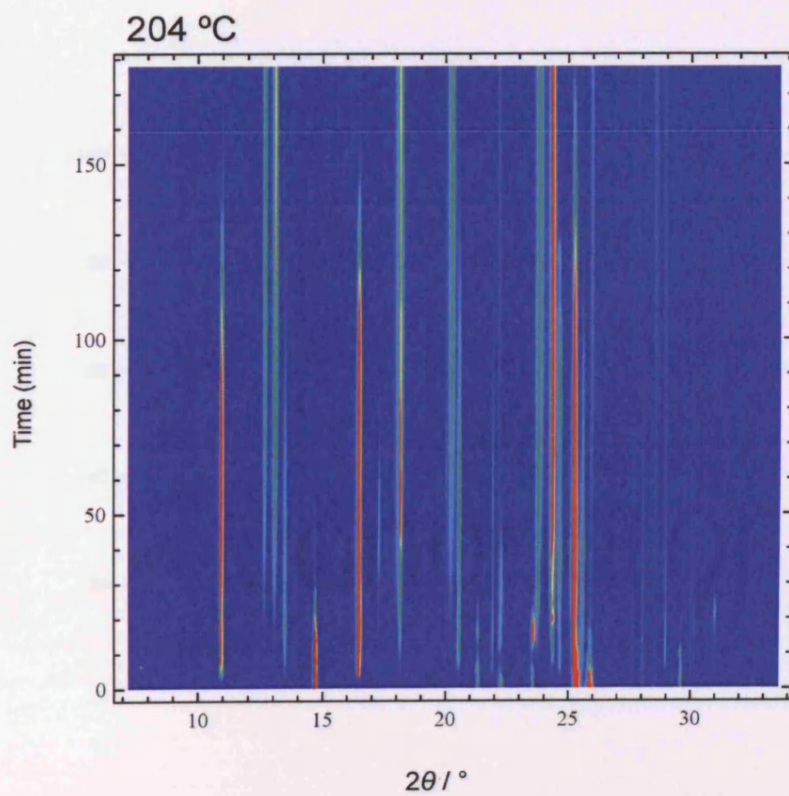
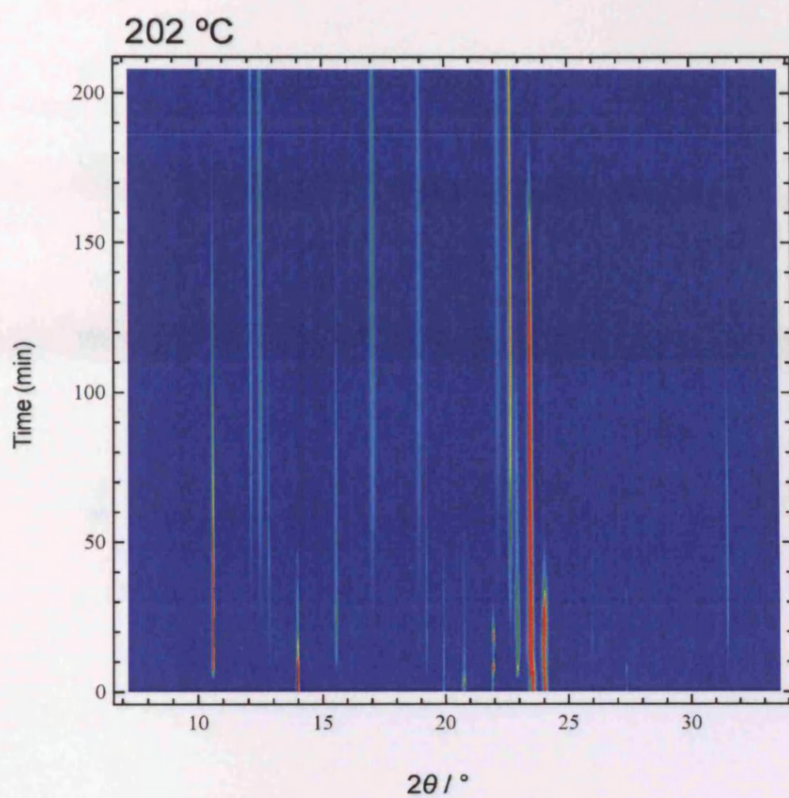
(Refer to Figure 5.8)

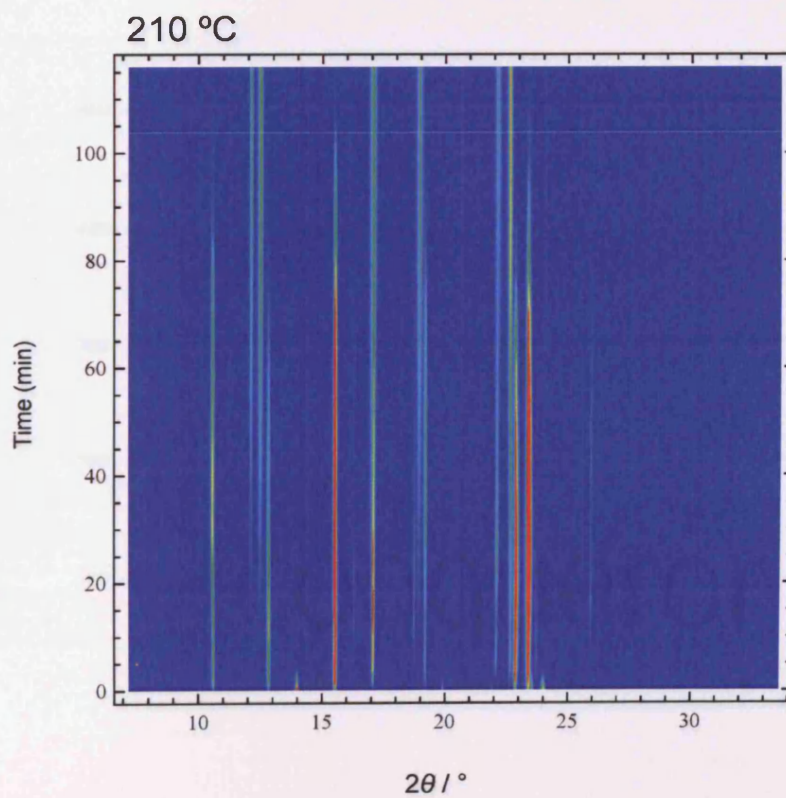
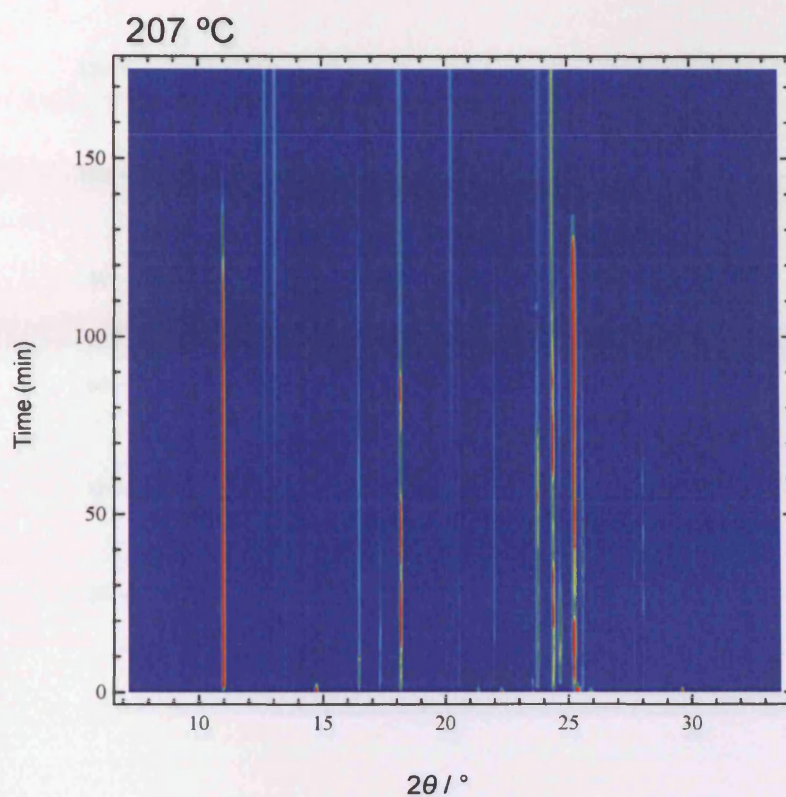


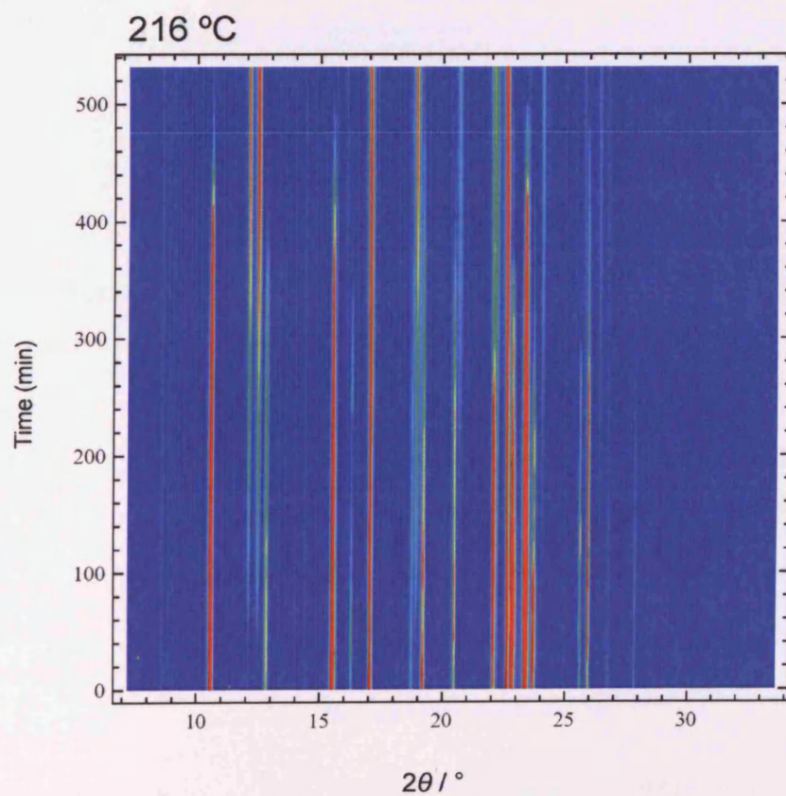
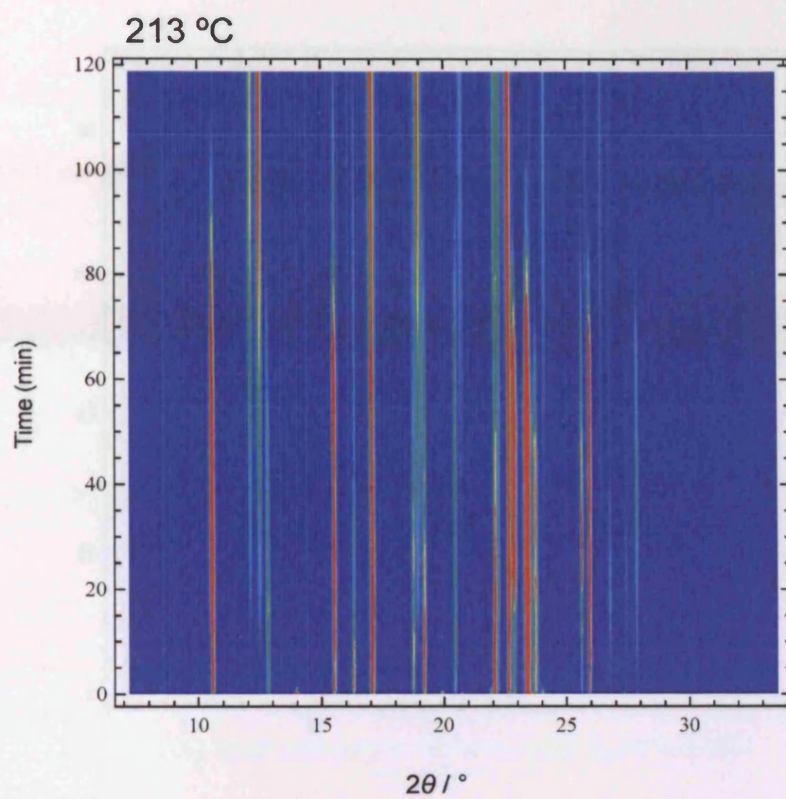


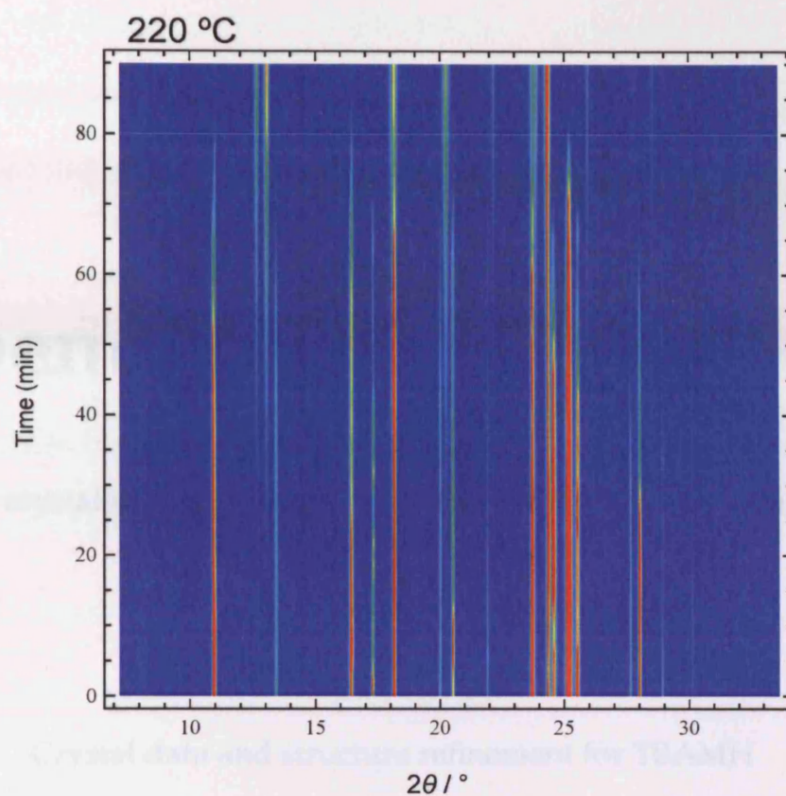












Appendix E

Extended crystallographic data for *t*-butylammonium acetate monohydrate (TBAMH).

Table E.1 Crystal data and structure refinement for TBAMH

| | | |
|-----------------------------|--|---------------------------|
| Empirical formula | $\text{C}_6\text{H}_{17}\text{NO}_3$ | |
| Formula weight | 151.21 | |
| Temperature | 293(2) K | |
| Wavelength | 0.71073 Å | |
| Crystal system, space group | Monoclinic, $P2_1/n$ | |
| Unit cell dimensions | $a = 7.6306(3)$ Å | $\alpha = 90^\circ$ |
| | $b = 18.0943(7)$ Å | $\beta = 98.572(2)^\circ$ |
| | $c = 14.2363(6)$ Å | $\gamma = 90^\circ$ |
| Volume | 1943.65(13) Å ³ | |
| Z | 8 | |
| Calculated density | 1.033 (10 ³ Kg/m ³) | |

Appendix E – Crystal data for TBAMH

| | |
|---|--|
| Absorption coefficient | 0.081 mm ⁻¹ |
| <i>F</i> (000) | 672 |
| Crystal size | 0.40 × 0.38 × 0.38 mm |
| θ range for data collection | 4.33° to 27.59° |
| Limiting indices | $-9 \leq h \leq 7$, $-21 \leq k \leq 23$, $-18 \leq l \leq 18$ |
| Reflections collected / unique | 11381 / 4417 [$R_{\text{int}} = 0.0842$] |
| Completeness to $\theta = 27.59$ | 98.2 % |
| Refinement method | Full-matrix least-squares on F^2 |
| Data / restraints / parameters | 4417/ 4 / 203 |
| Goodness-of-fit on F^2 | 1.027 |
| Final <i>R</i> indices [$I > 2\sigma(I)$] | $R1 = 0.0712$, $wR2 = 0.1570$ |
| <i>R</i> indices (all data) | $R1 = 0.1474$, $wR2 = 0.1872$ |
| Largest difference peak and hole | 0.161 e.Å ⁻³ and -0.137 e.Å ⁻³ |

Appendix E – Crystal data for TBAMH

Table E.2 Atomic coordinates ($\times 10^4$) and equivalent isotropic displacement parameters ($\text{\AA}^2 \times 10^3$) for TBAMH, $U(\text{eq})$ is defined as one third of the trace of the orthogonalized U_{ij} tensor.

| | <i>x</i> | <i>y</i> | <i>z</i> | <i>U</i> (eq) |
|-------|----------|----------|----------|---------------|
| C(1) | -2487(3) | -1024(1) | 6040(2) | 61(1) |
| C(2) | -1848(4) | -699(2) | 5173(2) | 92(1) |
| C(3) | -2722(4) | -1850(1) | 5941(2) | 78(1) |
| C(4) | -1283(4) | -834(2) | 6951(2) | 97(1) |
| C(5) | 1664(3) | 956(1) | 8913(2) | 61(1) |
| C(6) | 1750(4) | 133(2) | 9094(2) | 79(1) |
| C(7) | 1266(4) | 1131(2) | 7866(2) | 99(1) |
| C(8) | 375(4) | 1328(2) | 9475(3) | 92(1) |
| C(9) | 6562(3) | 1328(1) | 6165(2) | 63(1) |
| C(10) | 6853(5) | 2045(2) | 6693(2) | 98(1) |
| C(11) | 5575(3) | 1434(1) | 1676(2) | 59(1) |
| C(12) | 6629(5) | 1960(2) | 1163(2) | 94(1) |
| N(1) | -4273(2) | -695(1) | 6106(1) | 57(1) |
| N(2) | 3469(2) | 1271(1) | 9269(1) | 55(1) |
| O(1) | 6824(3) | 1294(1) | 5325(1) | 85(1) |
| O(2) | 6042(3) | 789(1) | 6590(1) | 89(1) |
| O(3) | 4403(2) | 1048(1) | 1205(1) | 67(1) |
| O(4) | 5959(2) | 1410(1) | 2558(1) | 83(1) |
| O(5) | 8079(2) | 2177(1) | 3992(1) | 71(1) |
| O(6) | 6062(3) | 482(1) | 8463(1) | 74(1) |

Appendix E – Crystal data for TBAMH

Table E.3 Bond lengths [Å] and angles [°] for TBAMH

| | |
|------------------|------------|
| C(1)-N(1) | 1.503(3) |
| C(1)-C(3) | 1.509(3) |
| C(1)-C(2) | 1.512(4) |
| C(1)-C(4) | 1.513(4) |
| C(5)-N(2) | 1.507(3) |
| C(5)-C(7) | 1.510(4) |
| C(5)-C(6) | 1.511(4) |
| C(5)-C(8) | 1.514(4) |
| C(9)-O(2) | 1.243(3) |
| C(9)-O(1) | 1.243(3) |
| C(9)-C(10) | 1.499(4) |
| C(11)-O(4) | 1.246(3) |
| C(11)-O(3) | 1.249(3) |
| C(11)-C(12) | 1.504(4) |
| N(1)-C(1)-C(3) | 107.58(19) |
| N(1)-C(1)-C(2) | 107.6(2) |
| C(3)-C(1)-C(2) | 110.9(2) |
| N(1)-C(1)-C(4) | 107.26(19) |
| C(3)-C(1)-C(4) | 110.7(2) |
| C(2)-C(1)-C(4) | 112.5(2) |
| N(2)-C(5)-C(7) | 107.00(19) |
| N(2)-C(5)-C(6) | 107.5(2) |
| C(7)-C(5)-C(6) | 111.8(2) |
| N(2)-C(5)-C(8) | 106.70(19) |
| C(7)-C(5)-C(8) | 112.2(2) |
| C(6)-C(5)-C(8) | 111.3(2) |
| O(2)-C(9)-O(1) | 122.6(2) |
| O(2)-C(9)-C(10) | 117.9(2) |
| O(1)-C(9)-C(10) | 119.5(2) |
| O(4)-C(11)-O(3) | 124.3(2) |
| O(4)-C(11)-C(12) | 116.7(2) |
| O(3)-C(11)-C(12) | 119.0(2) |

Appendix E – Crystal data for TBAMH

Table E.4 Anisotropic displacement parameters ($\text{\AA}^2 \times 10^3$) for TBAMH. The anisotropic displacement factor exponent takes the form: $-2 \pi^2 [h^2 a^{*2} U_{11} + \dots + 2 h k a^* b^* U_{12}]$

| | U_{11} | U_{22} | U_{33} | U_{23} | U_{13} | U_{12} |
|-------|----------|----------|----------|----------|----------|----------|
| C(1) | 59(1) | 58(1) | 67(1) | -5(1) | 13(1) | -3(1) |
| C(2) | 88(2) | 90(2) | 107(2) | 8(2) | 45(2) | -3(2) |
| C(3) | 83(2) | 60(2) | 94(2) | -5(1) | 15(2) | 4(1) |
| C(4) | 72(2) | 108(2) | 105(2) | -30(2) | -11(2) | 6(2) |
| C(5) | 59(1) | 54(1) | 67(1) | 4(1) | 0(1) | -5(1) |
| C(6) | 80(2) | 60(2) | 95(2) | 0(1) | 7(2) | -9(1) |
| C(7) | 108(2) | 97(2) | 79(2) | 14(2) | -29(2) | -24(2) |
| C(8) | 64(2) | 73(2) | 143(3) | 0(2) | 26(2) | 2(1) |
| C(9) | 75(2) | 53(1) | 58(1) | 1(1) | -4(1) | -5(1) |
| C(10) | 127(3) | 62(2) | 100(2) | -14(2) | -5(2) | -7(2) |
| C(11) | 68(2) | 59(1) | 53(1) | 1(1) | 17(1) | 3(1) |
| C(12) | 111(2) | 101(2) | 72(2) | 9(2) | 24(2) | -34(2) |
| N(1) | 63(1) | 51(1) | 57(1) | -1(1) | 10(1) | -5(1) |
| N(2) | 58(1) | 54(1) | 52(1) | 2(1) | 7(1) | -1(1) |
| O(1) | 107(1) | 89(1) | 57(1) | 5(1) | 4(1) | -26(1) |
| O(2) | 145(2) | 57(1) | 70(1) | 1(1) | 29(1) | -14(1) |
| O(3) | 80(1) | 65(1) | 54(1) | 2(1) | 7(1) | -10(1) |
| O(4) | 95(1) | 107(1) | 48(1) | 1(1) | 10(1) | -33(1) |
| O(5) | 79(1) | 61(1) | 73(1) | -4(1) | 11(1) | -10(1) |
| O(6) | 90(1) | 69(1) | 66(1) | -1(1) | 26(1) | -3(1) |

Appendix E – Crystal data for TBAMH

Table E.5 Hydrogen coordinates ($\times 10^4$) and isotropic displacement parameters ($\text{\AA}^2 \times 10^3$) for TBAMH.

| | <i>x</i> | <i>y</i> | <i>z</i> | <i>U</i> (eq) |
|--------|----------|----------|----------|---------------|
| H(2A) | -690 | -888 | 5123 | 137 |
| H(2B) | -1793 | -170 | 5230 | 137 |
| H(2C) | -2654 | -831 | 4615 | 137 |
| H(3A) | -3247 | -2036 | 6465 | 118 |
| H(3B) | -1588 | -2079 | 5937 | 118 |
| H(3C) | -3481 | -1959 | 5357 | 118 |
| H(4A) | -1775 | -1028 | 7482 | 146 |
| H(4B) | -1176 | -307 | 7009 | 146 |
| H(4C) | -133 | -1046 | 6939 | 146 |
| H(6A) | 2141 | 44 | 9757 | 118 |
| H(6B) | 2568 | -88 | 8726 | 118 |
| H(6C) | 595 | -79 | 8914 | 118 |
| H(7A) | 107 | 950 | 7616 | 149 |
| H(7B) | 2132 | 897 | 7540 | 149 |
| H(7C) | 1308 | 1656 | 7775 | 149 |
| H(8A) | -802 | 1150 | 9260 | 138 |
| H(8B) | 412 | 1853 | 9383 | 138 |
| H(8C) | 698 | 1216 | 10137 | 138 |
| H(10A) | 7504 | 1956 | 7313 | 148 |
| H(10B) | 5728 | 2263 | 6753 | 148 |
| H(10C) | 7512 | 2375 | 6350 | 148 |
| H(12A) | 5840 | 2301 | 796 | 141 |
| H(12B) | 7273 | 1687 | 748 | 141 |
| H(12C) | 7447 | 2228 | 1616 | 141 |
| H(1A) | -5013 | -795 | 5577 | 85 |
| H(1B) | -4168 | -207 | 6177 | 85 |
| H(1C) | -4695 | -887 | 6602 | 85 |
| H(2D) | 3466 | 1755 | 9157 | 82 |
| H(2E) | 4274 | 1054 | 8970 | 82 |
| H(2F) | 3734 | 1191 | 9891 | 82 |
| H(1) | 7480(30) | 1967(14) | 3502(12) | 85 |
| H(2) | 7690(30) | 1976(14) | 4469(13) | 85 |
| H(3) | 6080(40) | 587(15) | 7872(8) | 88 |
| H(4) | 5970(40) | 10(5) | 8511(19) | 88 |